



University  
of Glasgow

Wallace, Chloe May (2025) *Low molecular weight hydrogels for cell culture and bioprinting*. PhD thesis.

<https://theses.gla.ac.uk/84900/>

Copyright and moral rights for this work are retained by the author

A copy can be downloaded for personal non-commercial research or study,  
without prior permission or charge

This work cannot be reproduced or quoted extensively from without first  
obtaining permission in writing from the author

The content must not be changed in any way or sold commercially in any  
format or medium without the formal permission of the author

When referring to this work, full bibliographic details including the author,  
title, awarding institution and date of the thesis must be given

Enlighten: Theses

<https://theses.gla.ac.uk/>  
[research-enlighten@glasgow.ac.uk](mailto:research-enlighten@glasgow.ac.uk)



# University of Glasgow

## Low Molecular Weight Hydrogels for Cell Culture and Bioprinting

Chloe May Wallace

Submitted in fulfilment of the requirements for the Degree of  
Doctor of Philosophy

School of Chemistry

College of Science and Engineering

University of Glasgow

August 2024

## Abstract

Low molecular weight gelators (LMWG) are promising candidates for biomaterials due to their unique properties such as their reversibility and ability to hold large volumes of solvent. However, issues can arise when attempting to gel these materials under conditions acceptable for cell culture. In this thesis, the aim was to develop and comprehensively characterise a LMWG system at physiological pH. We employ a variety of techniques to investigate these materials across different length scales. By doing so, we have highlighted the significance of such characterisation when developing novel non-covalent biomaterials.

We outline how the dipeptide-based LMWG 2NapFF (diphenylalanine protected with a naphthalene group at the *N*-terminus) produces biocompatible hydrogels when crosslinked with ions present in cell culture media. We also explore the impact of heating and cooling the gelator solution prior to initiating gelation as well as the impact of adding PODS® (micron-scale proteins containing cargo molecules which are gradually released over prolonged periods) to the system for functionalisation purposes. Our findings reveal that a heating and cooling cycle can be used to adjust the properties of the resulting network without changing the gelator itself. Moreover, it was found that PODS® had minimal effect on the properties of the hydrogel, indicating that they can enhance the bioactivity of the systems without altering the network structure. PODS

Furthermore, we compare the 2NapFF hydrogels previously discussed to a Ureido-pyrimidinone (UPy) supramolecular hydrogel system, consisting of a monofunctional building block and bifunctional crosslinker species. We explored the effects of combining these two systems, both with and without the UPy crosslinker. Our results show that the assembly of the combined systems is primarily driven by the UPy component. Furthermore, the UPy crosslinker plays a vital role in the self-sorting of the UPy and 2NapFF components. It was also revealed that for cells to adhere effectively, the bifunctional UPy subunit was crucial to produce a supportive network.

In the final experimental chapter, we investigate the potential of the 2NapFF hydrogels crosslinked with cell culture media as bioinks for extrusion-based 3D printing. Through optimisation of the printing process, it was demonstrated that the type of media used to trigger gelation directly impacted the printability of the systems. As a result, the samples that consistently formed self-supporting structures were selected for printing macrophage cells, which remained viable within the gel after 24 hours. Bioprinting macrophages can be used in applications such as immune system and tumour microenvironment modeling.

# Table of Contents

1.1 Hydrogels	14
1.1.1 Natural hydrogels	14
1.1.2 Synthetic hydrogels	14
1.2 Low molecular weight gelators	15
1.3 Gelation triggers	17
1.3.1 pH	17
1.3.2 Solvent switch	18
1.3.3 Temperature	19
1.3.4 Light	20
1.3.5 Enzyme	20
1.3.6 Divalent metal salt	21
1.4 LMWGs gelators for cell culture	23
1.4.1 2D Cell Culture	24
1.4.2 3D Cell Culture	25
1.5 Multicomponent LMWGs for cell culture	27
1.6 Printing LMWG for cell culture	29

1.7 Functionalisation of hydrogels for cell culture	30
1.7.1 PODS®	32
1.8 Aims of thesis	33
1.9 References	34
2.1 Materials	45
2.2 2NapFF Synthesis	45
2.3 Sample Preparation	47
2.3.1 Chapter 3 Sample Preparation	47
2.3.2 Chapter 4 Sample Preparation	48
2.3.3 Chapter 4 Sample Preparation	48
2.4 Shear Rheology	49
2.5 Cavitation Rheology	50
2.6 Small-Angle Scattering	51
2.6.1 SAXS	51
2.6.2 SANS	52
2.6.3 Fitting Small-Angle Scattering Data with SASView	53
2.7 Cryo-TEM	54

2.8 Circular Dichroism	55
2.9 3D Printing	55
2.10 Cell Culture	55
2.10.1 Immunofluorescence	57
2.10.2 Live/Dead Assay	57
2.11 Confocal Microscopy	57
2.12 Bioprinting	58
2.13 References	
3.1 Introduction	62
3.2 Results and discussion	64
3.2.1 The effect of heating and cooling 2NapFF as a solution	65
3.2.2 Incorporating •PODS® Growth Factors	81
3.3 Conclusions	90
3.4 References	92
4.1 Introduction	96
4.2 Results and discussion	99
4.2.1 Small-Angle Scattering (SAXS and SANS)	100
4.2.2 Cryogenic transmission electron microscopy (cryo-TEM)	107

Chapter 1	
4.2.3 Rheology and circular dichroism	108
4.2.4 Cell culture studies	111
4.3 Conclusion	113
4.4 References	114
5.1 Introduction	118
5.2 Results and discussion	121
5.2.1 Optimisation of 3D printing parameters	113
5.2.2 Using SAXS to investigate the effect of 3D printing	128
5.2.3 Optimisation of parameters for bioprinting	132
5.2.4 Bioprinting macrophages with 2NapFF/RPMI	136
5.3 Conclusions	137
5.4 References	141
6. Conclusions and future work	142

# Acknowledgments

## *Go raibh míle maith agat*

First, I would like to say a huge thank you to my supervisor Prof Dave Adams. Thank you for giving me the opportunity to work in your group over the last four years and for all your support, guidance and general mentorship. I honestly could not have wished for a better supervisor and I am so grateful for your constant words of assurance and inspirational Drag Race quotes.

I would also like to thank Dr Rich Williams from Queen's University Belfast and Dr Hugues Miel from Almac Discovery. You both taught me so much about research, and I never would have believed I was capable of pursuing a PhD if I had not have worked with you.

A very special thank you to Rebecca Ginesi, it has been a pleasure to go through this PhD with you. You are genuinely the smartest, most selfless person I know and I am so lucky to have you as a best friend. Thank you for being by my side through all the ups and downs of this process, I truly could not have done it without you, and of course our beloved son Jinkx.

A massive thank you to all the members of the Adams group past and present. Courtenay Patterson, thank you for essentially adopting me when I started. Moving to a new city during a pandemic was daunting, but having my Irish big sister made me feel right at home. To Libby Mashall, thank you for your continual encouragement and for never failing to make me smile with your endless supply of cat photos. Thank you to my cohort buddies, Max Hill and Qingwen Guan for always checking in. To Simona and Emma, thank you for all your help and advice, especially with SAXS experiments. Our trip to ESRF is one of my favourite PhD memories, especially attempting to navigate Grenoble on electric scooters at night! To Alex and Dipankar thank you for your help and time. To Rui, Fin, Yanyao, Tejaswini, Olivia and Helen, best of luck on your PhD journey! I am consistently impressed by you all and can't wait to hear about all your achievements in the future.

I would also like to thank the Draper group members past and present. Bart, thank you for being so patient and helpful during my time in the lab, you have taught me so much. To Becky and Jakki, thank you for your friendship as well as your amazing flat parties! Thank you to Nick, my partner in crime, for always making me laugh and brightening my day. To Connor and Lineta, thank you for putting up with me invading your office for a chat and a cup of tea.

A massive thank you goes to Prof Patrica Dankers for hosting me for a 12-week placement during my PhD. Thank you also to the Dankers group for making me feel so welcome, my time in Eindhoven was genuinely a highlight of my PhD because of you all. Maritza, thank you for giving up your time to carry out cell experiments for me. Riccardo, thank you for teaching me about Cryo-TEM and carrying out many measurements. Martin, thank you for the rheology experiments in Chapter 3 – I could not have completed the chapter without all your help!

I would like to take this opportunity to thank my second supervisors Prof Matt Dalby and Prof Manuel Salmeron-Sanchez for their advice and guidance throughout the PhD. Thank you also to my industry supervisor Dr Jonathan Best from Cell Guidance Systems, for helping with all my PODS® queries. A big thank you to everyone at LifETIME CDT and the CeMi for all their help with the cell work discussed in chapters 2 and 4. In particular, I would like to express my gratitude to Sabah and Marta for their patience and help over the last four years. You have both taught me so much about biology and I'm going to miss our Taylor Swift catch ups at the ARC!

Thank you to everyone who has contributed to the scattering data presented in this thesis. To Sam Burholt from Diamond Light Source and Martin Rosenthal from ESRF for processing the SAXS data in Chapter 1. To Annela Seddon from the University of Bristol for collecting and processing the SAXS data presented in Chapter 3. To James Douch from ISIS Neutron Scattering for processing the SANS data from the same chapter, as well as Prof Dave Adams and Prof Emily Draper for collecting this data. To Andy Sutherland for processing the data presented in Chapter 4.

Thank you to my family, I truly could not have gone through this process without your unwavering support from across the water. To Jade and Bronagh for blindly supporting me - even though you're still not sure what I actually do! Thank you for always keeping your door open for a Boojum and a rant when things were tough, Joni is so lucky to have not one, but two amazing mums! On that note, thank you to my perfect niece Joni for bringing so much joy into our lives, I can't wait to see who you grow up to be! Thank you to my mum Maudeen, for supporting my decision to do this PhD and believing in me, even when I didn't believe in myself. Knowing you're just a phone call away has been such a comfort throughout all of this and I could not have done it without you. Finally, I'd like to thank my dad, Leo. Thank you for always encouraging my interest in science, even if it did involve watching countless episodes of Brian Cox's "Wonders of the Universe". I wish you were here to experience this with me and I hope I have made you proud.

## List of Abbreviations

$\beta$ -Gal:  $\beta$ -galactosidase

2D: Two-dimensional

3D: Three-dimensional

AFM: Atomic force microscopy

B: Bifunctional

BMP-2: Bone morphogenetic protein 2

BSA: Bovine serum albumin

CD: Circular dichroism

CRAB: Cavitation Rheology Analyser Box

cRGD: Cyclic arginyl-glycyl-aspartic acid

Cryo-TEM: Cryogenic transmission electron microscopy

d-2NapFF: Deuterated 2NapFF

DBS: Dibenzylidene-D-sorbitol

DLS: Dynamic Light Scattering

DMEM Dulbecco's Modified Eagle Medium

DMSO: Dimethyl sulfoxide

DNA: Deoxyribonucleic acid

ECM: Extracellular matrix

EDTA: Ethylenediaminetetraacetic acid

ESRF: European Synchrotron Radiation Facility

Et al.: Et alii

FBS: Fetal bovine serum

FGF: Fibroblast growth factor

Fmoc: Fluorenylmethyloxycarbonyl

FTIR: Fourier transform infrared

G': Storage modulus

G'': Loss modulus

GdL Glucono- $\delta$ -lactone  
GFP: Green fluorescent protein  
hBDNF Human brain-derived neurotrophic factor  
HCl: Hydrochloric acid  
HeLa: Henrietta Lacks  
hNDFs: Human neonatal dermal fibroblasts  
HPLM: Human plasma-like medium  
HT: High tension  
HVSCs Human ventricular scar cells  
I : Intensity  
IBCF: Isobutyl chloroformate  
IDIM: Iscove's Modified Dulbecco's Medium)  
Leu: Leucine  
LMWG: Low molecular weight gelator  
M: Monofunctional  
MDCK: Madin-Darby canine kidney  
MSC: Mesenchymal stem cell  
Nap: naphthalene  
NMM *N*-methylmorpholine  
PA: Peptide amphiphile  
PA: Polyamide  
PBS: Phosphate-buffered saline  
 $P_c$ : Critical pressure  
PEG: Poly(ethylene glycol)  
Phe: Phenylalanine  
PODS® (POlyhedrin Delivery Systems)  
PMA: Phorbol 12-myristate 13-acetate  
P/S: Penicillin-streptomycin  
PVA: Polyvinyl alcohol

Q: Scattering vector

RGD: Arginyl-glycyl-aspartic acid

RGDS: Arginine-glycine-aspartic-serine

r: Radius

RPMI: Roswell Park Memorial Institute

SAXS: Small-angle X-ray scattering

SANS: Small-angle neutron scattering

SEM: Scanning electron microscopy

SLDs: Scattering length densities

Sol-to-gel: Solution-to-gel

t: Time

TEM: Transmission electron microscopy

TFA: Trifluoroacetic acid

TGF: Transforming growth factor

THF: Tetrahydrofuran

THP-1: Tohoku hospital pediatrics-1

UPy Ureido-pyrimidinone:

USAXS: Ultra-small-angle X-ray scattering

UV: Ultraviolet

V: Volume

VEGF: Vascular endothelial growth factor

## **Declaration of authorship**

This Thesis has been written and compiled by the author, Chloe Wallace, who carried out the research at the University of Glasgow between 2020 and 2024 under the supervision of Professor Dave Adams. I declare that this Thesis is the result of my own work, and any contributions from others is explicitly referenced. This work has not been submitted for any other degree at the University of Glasgow or any other institution.

Chloe Wallace

# **Chapter 1: Introduction**

## 1.1 Hydrogels

Gels are viscoelastic materials which possess physical properties inbetween those of a liquid and a solid.<sup>1</sup> They can be classified as organogels, hydrogels, xerogels or aerogels depending on the solvent which is immobilised by their three-dimensional network.<sup>2</sup> Hydrogels are particularly of interest for biomedical applications due to their ability to retain significant amounts of water in their structure.<sup>3</sup> This combined with their flexible nature and fibrous structure, closely resembles the three-dimensional arrangement of the extracellular matrix (ECM).<sup>4</sup> Consequently, hydrogels have become the most common materials 3D cell culture.<sup>5</sup> These materials can be categorised as either natural or synthetic.

### 1.1.1 Natural Hydrogels

Natural hydrogels tend to possess inherent biocompatibility and biodegradability.<sup>6</sup> Protein-based hydrogels such as collagen and gelatin are widely used as ECM mimics due to their biodegradability and ability to form under physiological conditions. Moreover, these materials contain motifs that promote cell adhesion which is essential for cell survival.<sup>7</sup> Nevertheless, challenges arise from their batch-to-batch variability and undefined chemical composition.<sup>8</sup>

While polysaccharide hydrogels, such as chitosan and alginate may offer a more defined chemical composition, their weak mechanical properties can be problematic.<sup>9</sup> Furthermore, these systems lack the cell adhesion cues and degradability of protein-based hydrogels, thus functionalisation is usually required for cell culture applications.<sup>10</sup> To overcome the drawbacks associated with naturally derived products, these hydrogels have started to be replaced or hybridised with synthetic hydrogel systems.<sup>11</sup>

### 1.1.2 Synthetic hydrogels

Synthetic hydrogels are fabricated by crosslinking bioinert subunits via chemical reactions. This defined chemical composition results in hydrogels with higher controllability and reproducibility than their natural counterparts.<sup>12</sup> Synthetic hydrogels also tend to have superior mechanical properties when compared to natural hydrogels, such as improved mechanical strength, durability and reduced rate of degradation.<sup>13</sup> Commonly used examples include polyethylene glycol (PEG),<sup>14</sup> polyacrylamide (PA)<sup>15</sup> and polyvinyl alcohol (PVA).<sup>16</sup>

While these materials are generally considered bioinert and non-toxic, hybridisation with a natural hydrogel is often required to achieve a balance between biocompatibility and desired mechanical properties.<sup>17</sup> This method is also an effective way of adding bioactive signals to the system by incorporating cell adhesion cues and degradable peptides.<sup>17, 18</sup>

## 1.2 Low molecular weight gelators

Hydrogels can also be categorised as chemical or physical depending on the interactions driving their gelation (Figure 1). The network of chemical hydrogels is held together by irreversible covalent crosslinks, generating mechanically robust, polymeric materials. On the other hand, physical hydrogels are formed via weak, reversible, non-covalent bonds (Figure 1).

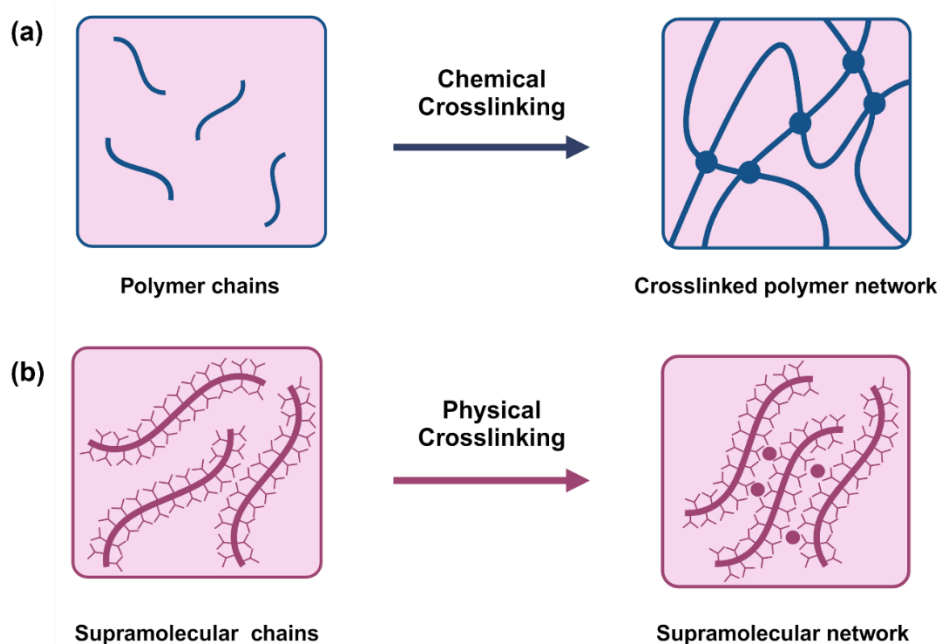


**Figure 1.** Schematic showing the mechanisms of both (a) chemical (where chemical crosslinks are represented as blue circles) and (b) physical gelation.

Low molecular weight gelators (LMWG) form a particularly interesting class of physical gels. These small molecule gelators offer a host of advantages that chemical hydrogels lack, namely their reversibility and tuneable properties.<sup>19</sup> Due to the low molecular weight of such compounds (typically below 1000 Da), they also tend to be relatively inexpensive and easy to synthesise, thus having the potential to be produced on a large scale.<sup>20, 21</sup> These LMWG initially assemble into long one-dimensional structures via physical interactions such as hydrogen bonding,  $\pi$ - $\pi$  stacking, and Van der Waals interactions (Figure 2a). The one-

dimensional structures produced then crosslink or entangle to produce a network in which the solvent is entrapped (Figure 2b).<sup>22</sup>

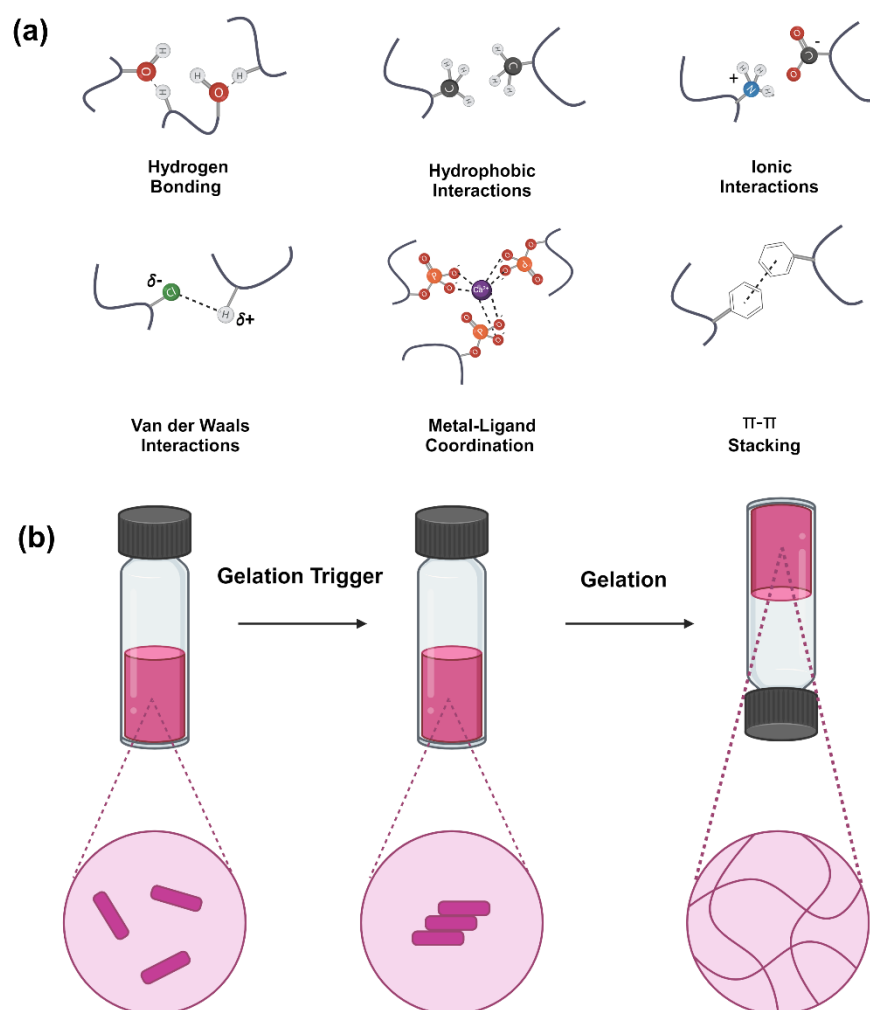


**Figure 2.** (a) Non-covalent interactions capable of driving the formation of LMWG. Figure adapted from *Chemistry- An Asian Journal*, 2020, **17**, e202200081.<sup>23</sup> (b) Scheme depicting the hierarchal self-assembly which is undergone by LMWG. Once a trigger is applied to the free gelator molecules suspended in solvent, they start to arrange themselves into ordered structures which eventually form a self-supporting gel network.

Peptide-based LWMG are appealing candidates for use as biocompatible scaffolds and encapsulation of bioactive moieties, as they tend to have high biocompatibility and potential to incorporate biological active sequences.<sup>24, 25</sup> Marchesan et al. have investigated the potential of ultrasmall uncapped peptides (i.e. peptides without a protecting groups at either terminus) as biomaterials and the effect of stereochemistry on their self-assembly.<sup>26, 27</sup> More commonly, these small peptides tend to include an aromatic capping group on the *N*-terminus such as an Fmoc group.<sup>28, 29</sup> The addition of this large hydrophobic group at the *N*-terminus

of the molecule, combined with a charged group at the C-terminus, means these gelators are amphiphilic in nature, i.e. they contain both hydrophobic and hydrophilic regions.<sup>30</sup>

The incorporation of the amino acid sequence arginyl-glycyl-aspartic acid (RGD) into cell scaffolds is of particular interest due its cell adhesive properties.<sup>31</sup> When a combination Fmoc-RGD and Fmoc-FFF was employed for the culture of mesenchymal stem cells (MSCs), they were found to promote cell proliferation and differentiation.<sup>32</sup> Additionally, the work of Alakpa and co-workers has shown that by varying concentrations of Fmoc-FF and Fmoc-S, hydrogels with a range of stiffnesses could be accessed.<sup>33</sup> These tunable properties allowed for targeted differentiation of MSCs. However, it is important to consider that Fmoc groups are not present in the extracellular matrix and thus may lead to toxicity issues.<sup>34</sup>

### 1.3 Gelation Triggers

As mentioned above, for gelation to occur a trigger is required. Initially, the LMWG is suspended in a solvent. Once the gelation trigger is applied, the solubility of the LMWG molecules reduces significantly. Consequentially, aggregation of the LMWG occurs, leading to the self-assembly of a gel network, entrapping the solvent.<sup>35, 36</sup> Commonly used gelation triggers for LMWG include pH,<sup>37</sup> solvent switching,<sup>38</sup> temperature,<sup>39</sup> light,<sup>40</sup> enzyme<sup>41</sup> and metal cation triggers.<sup>42</sup> The gelation trigger influences how the structures self-assemble and thus also impacts the mechanical properties of the resulting network.<sup>43</sup> Therefore, when deciding which trigger to apply to a system it is essential to evaluate how it impacts the resulting mechanical properties and whether it is appropriate for the intended application. This is particularly important when designing systems for biological applications such as cell culture, when a controlled and sterile environment is essential for cell survival.

#### 1.3.1 pH

Using a pH change to promote gelation is one of the most used triggers for LMWG. For a pH trigger to be successful, the gelator must contain a functional group that can be deprotonated and reprotonated when required. Often, this will be in the form of a carboxylic acid at the C-terminus of the gelator molecule. When solubilised in water, the terminal carboxylic acid group is deprotonated, producing a solution at a pH above the apparent  $pK_a$ . Upon the addition of an acid, the pH of the system drops causing the carboxylate to be

reprotonated.<sup>44</sup> This reduces the solubility of the LMWG causing it to self-assemble into a gel network (Figure 3).

Regarding biomedical applications, the restricted pH range at which gelation can occur produces challenges, especially as dipeptide-conjugate LMWG tend to gel at a pH lower than physiological pH (pH 7.4).<sup>45</sup>

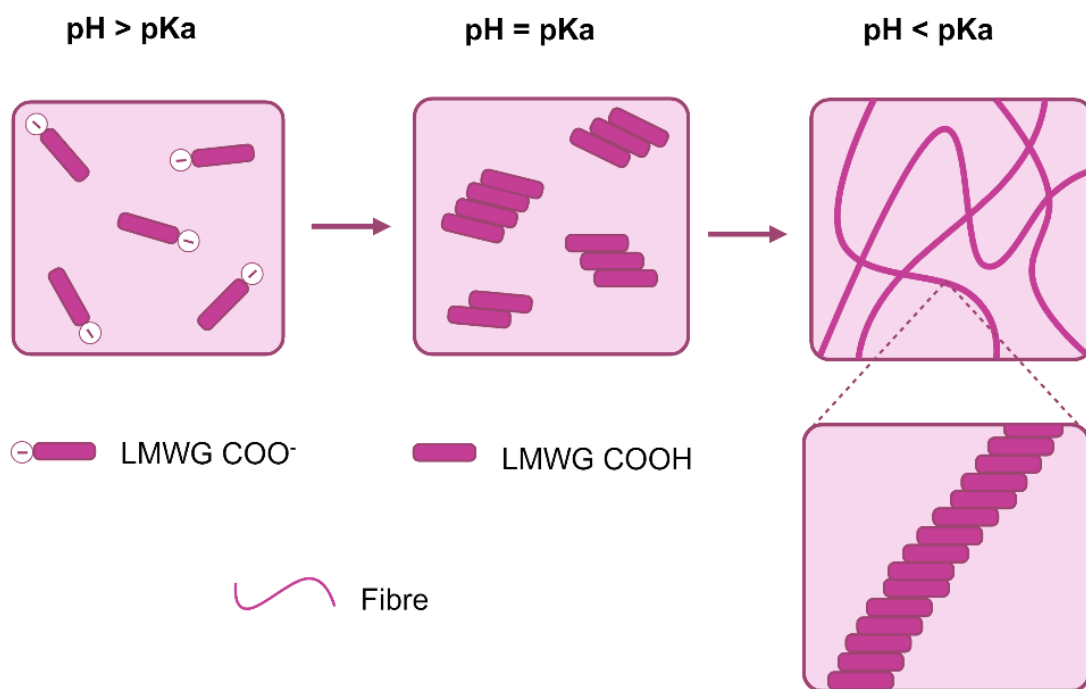


**Figure 3.** Schematic depicting the self-assembly of a LMWG with a free C-terminus, using pH as a gelation trigger. When dissolved in water, the terminal carboxylic acid group is deprotonated, resulting in a solution with a pH above the apparent  $\text{pK}_a$ . When the pH of the solution is lowered, the carboxylate is reprotonated. This reduces the solubility of the LMWG causing it to self-assemble into a gel network.

### 1.3.2 Solvent Switch

A second method of triggering the gelation of a LMWG is via a solvent trigger. This technique requires the gelator to be suspended in an organic solvent, such as acetone or DMSO. Water is then added to the solution, the solubility of the gelator molecules decreases, which induces self-assembly.<sup>46</sup> A solvent switch gelation trigger can be advantageous as it produces homogenous gels quickly,<sup>47</sup> An example of using this method for cell culture comes from Liu et al. who developed a library of LMWG with a C2-symmetric 1,4-diamide cyclohexane or benzene core.<sup>48</sup> Multiple cell lines were encapsulated into the hydrogel scaffolds by mixing the cells in DMEM (Dulbecco's Modified Eagle Medium) with the concentrated gelator in DMSO. The final solution had a DMSO concentration of between

2.5 and 3.3% which is considered acceptable by the authors as it is much lower than the concentration typically used for cell freezing medium (10%). Despite this, the need for an organic solvent means that a solvent trigger is not commonly used for biological applications, especially as it can be argued that concentrations of DMSO above 0.1% can affect cell viability.<sup>49</sup>

### 1.3.3 Temperature

Another method of altering the solubility of a LMWG to trigger gelation is to use a heat-cool cycle. This process involves heating the solution of LMWG suspended in water, increasing its solubility, before cooling to room temperature. As the solution is cooled, the solubility of the gelator decreases again, instigating self-assembly.<sup>50</sup> Work from Hansda et al. reports the successful hydrogelation of an *N*-Boc protected peptide-based amphiphile by suspending in PBS at physiological pH and heating until a clear solution was obtained.<sup>51</sup> Once cooled upon standing, a self-supporting hydrogel network was formed. A cytotoxicity study was carried out using human embryonic kidney cells and fibroblast cells. After a 24-hour incubation time, it was found that the gelator did not lead to cytotoxic effects in either cell line. The hydrogel was also found to exhibit strong antibacterial effects as well as the ability to release drugs including naproxen, in a sustained and controlled manner. These results highlight the vast potential of this biomaterial for applications from drug delivery to wound healing where antibacterial properties are essential.

However, a potential limiting factor of this trigger is that controlling the cooling rate is crucial to obtain reproducible results, as it dictates the rate of self-assembly and therefore the properties of the resulting hydrogel.<sup>52</sup> A temperature trigger has previously been used to develop nucleoside derived LMWG for 3D cell culture. This entailed heating mixtures of the LMWG to 80 °C for 10 minutes, before allowing to cool to room temperature. While the materials produced were found to support cell adhesion and proliferation, it was also noted that the high temperature is likely to have denatured many of the proteins present in the FBS. Moreover, heating to temperatures above 37°C eliminates the option of adding the cells at this point and thus may limit the system's potential for 3D culture applications.

### 1.3.4 Light

While light-triggered hydrogelation is traditionally associated with polymer crosslinking,<sup>53</sup> it can also be exploited to trigger LMWG gelation. This is often a response to the irradiation of photoresponsive LMWG switching between the cis- and trans- isomers when irradiated with light of a particular wavelength.<sup>54</sup>

One advantage of this technique is that it allows for spatial and temporal control over the gelation as the radiation can be focused on a particular area rather than the bulk.<sup>55</sup> This is particularly favourable for cell culture applications as spatially resolved irradiation allows for fine control over the mechanical properties of certain areas within the gel<sup>56</sup> and gel strength has been found to correlate with cell growth and differentiation.<sup>57</sup> Moreover, light-triggered gelation is a non-invasive process.<sup>54</sup> The work of Das and co-workers details the design and synthesis of a low molecular weight gelator peptide-drug conjugate for the photo-controlled delivery of chemotherapeutic agent 5-Fluorouracil (Figure 4).<sup>58</sup> The irradiation of the gelator under UV light at 365 nm induced 26% liberation of the drug after 40 minutes. Further biocompatibility studies using a HeLa cell line confirmed cell viability up to 80  $\mu$ M. However, it is worth noting that certain wavelengths of light are unsuitable for such applications due to their capability of causing cell damage, particularly when a longer exposure time is necessary.<sup>59, 60</sup>

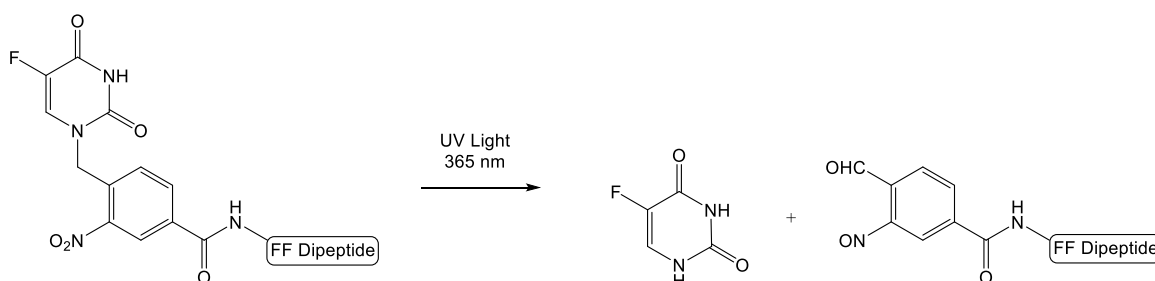


**Figure 4.** The mechanism of photocleavage reaction for the release of the chemotherapeutic agent 5-Fluorouracil and o-nitroso benzaldehyde. Figure adapted from *ChemistrySelect*, 2019, 4, 6667-6843 with permission from John Wiley and Sons, license number 5854710139454<sup>58</sup>

### 1.3.5 Enzymes

Another method for inducing gel assembly or disassembly is utilising enzyme-catalysed reactions to transform a non-gelator into a gelator, often in a reversible manner.<sup>61</sup> This occurs when specific enzymes catalyse chemical changes to the LMWG structure via the activation of a pro-gelator molecule.

Alternatively, the reverse reaction may take place, leading to a gel-to-sol transition.<sup>62</sup> Enzyme-triggered gelation is of particular interest for biomedical applications such as tissue engineering,<sup>63, 64</sup> bioimaging<sup>65, 66</sup> and drug delivery,<sup>67, 68</sup> due to its high specificity towards substrates and catalytic efficiency.<sup>69</sup> One notable example comes from the work of Zhao et al. who reported using the enzyme  $\beta$ -galactosidase ( $\beta$ -Gal) to catalyse the hydrolysis of Nap-FFK(galactose), releasing galactose and generating the gelator Nap-FFK. The Nap-FFK molecules then self-assemble into nanofibers which underpin the hydrogel structure.<sup>70</sup>

While the previous example used bond cleavage to trigger self-assembly, work from Toldano and co-workers describes using bond formation convert precursors (Fmoc-F and F<sub>2</sub>) to a LMWG. (Fmoc-FFF) (Figure 5).<sup>71</sup> It was noted that both thermolysin or lipase enzymes could be used to carry out this coupling and the resulting hydrogel could be used to culture microglial cells with a high viability.<sup>72</sup>

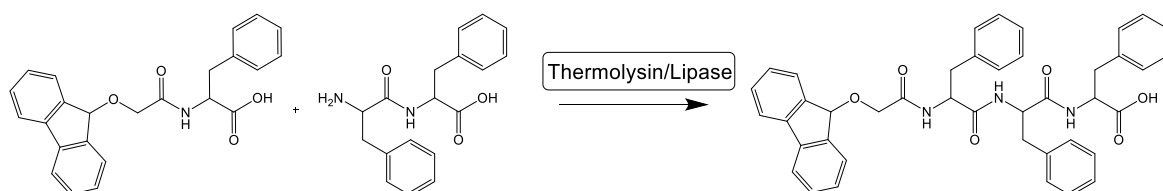


**Figure 5.** Mechanism of enzyme-mediated formation of Fmoc-FFF. Adapted from *J. Am. Chem. Soc.*, 2006, **128**, 1070.<sup>71</sup>

While the presence of enzymes within the ECM can be beneficial in terms of biocompatibility, managing the distribution and levels of expression of the specific enzyme required for gelation *in vivo* can pose difficulties.<sup>70</sup> Similarly, potential off-target effects must be thoroughly considered. Particularly because if gelation is activated in a non-target tissue, an immune response will be provoked due to the presence of the foreign material or enzyme.<sup>73</sup> Therefore the specificity of the enzyme used is crucial for success.<sup>74, 75</sup>

### 1.3.6 Divalent Metal Salt

As noted above, the restricted pH range at which many LMWG self-assemble can be problematic for biomaterial applications. Crosslinking these gelators using divalent cations at high pH may offer a solution. When *N*-protected dipeptide gelators with a free carboxylic acid group at the C-terminus are dissolved at high pH, the molecules can aggregate into structures such as spherical or worm-like micelles.<sup>76</sup>

If worm-like micelles are present in the solution, the addition of divalent cations (such as Ca<sup>2+</sup>) prompts the crosslinking of neighbouring carboxylate groups (Figure 6).<sup>77</sup> This

reduces the solubility of the LMWG in water, eventually leading to the formation of a metal-coordinated hydrogel.

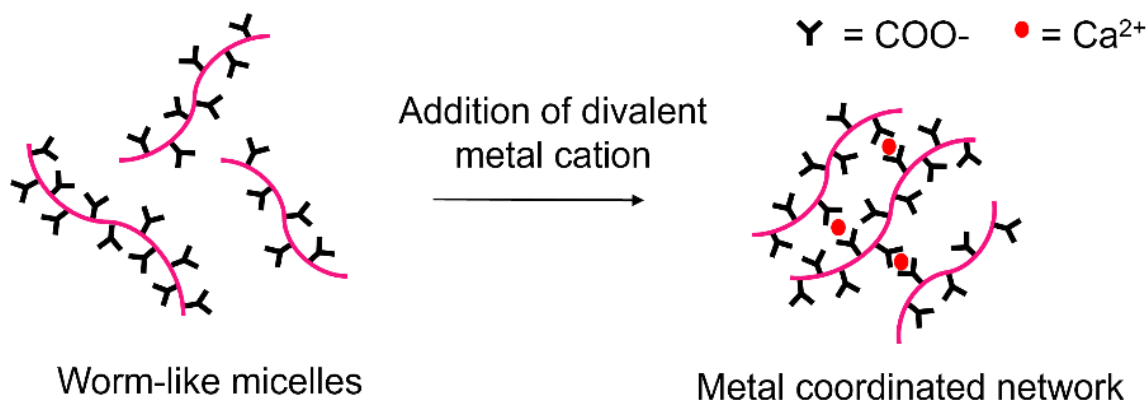


**Figure 6.** Cartoon illustrating the ionic crosslinking of carboxylate groups on the worm-like micelles when divalent calcium ions are added. Adapted from *Chem*, 2017, **3**, 390-410.<sup>78</sup>

The use of divalent metal cations to trigger gelation is an attractive option for biological applications as many buffers already contain metal ions. One example of this comes from the work from Krajl et al., which describes the development of a potential biomaterial when investigating the impact of chirality and halogenation on phenylalanine dipeptides (Figure 7).<sup>79</sup> Various analogues of diphenylalanine were synthesised and gelled using PBS to provide ions which formed salt bridges between the dipeptide zwitterions at pH 7.3. When fibroblasts were cultured on the resulting hydrogels a live/dead assay revealed that compounds 3-5 were unstable and resulted in low cell numbers and the presence of dead cells (Figure 7). Compound 6 was the most stable hydrogel but lacked cytocompatibility. The most promising result came from compound 2 (d-Phe-l-Leu) on which the fibroblast cells proliferated in high numbers.

When considering a divalent metal salt trigger for gelation potential issues may arise due to ion concentration and specificity. Especially as an excess of divalent cations can lead to uncontrolled gelation, and thus inconsistent material properties.<sup>80</sup> As well as this, the presence of divalent cations may interfere with other biochemical processes or components within the biomaterial, potentially affecting its functionality and performance.<sup>81</sup>

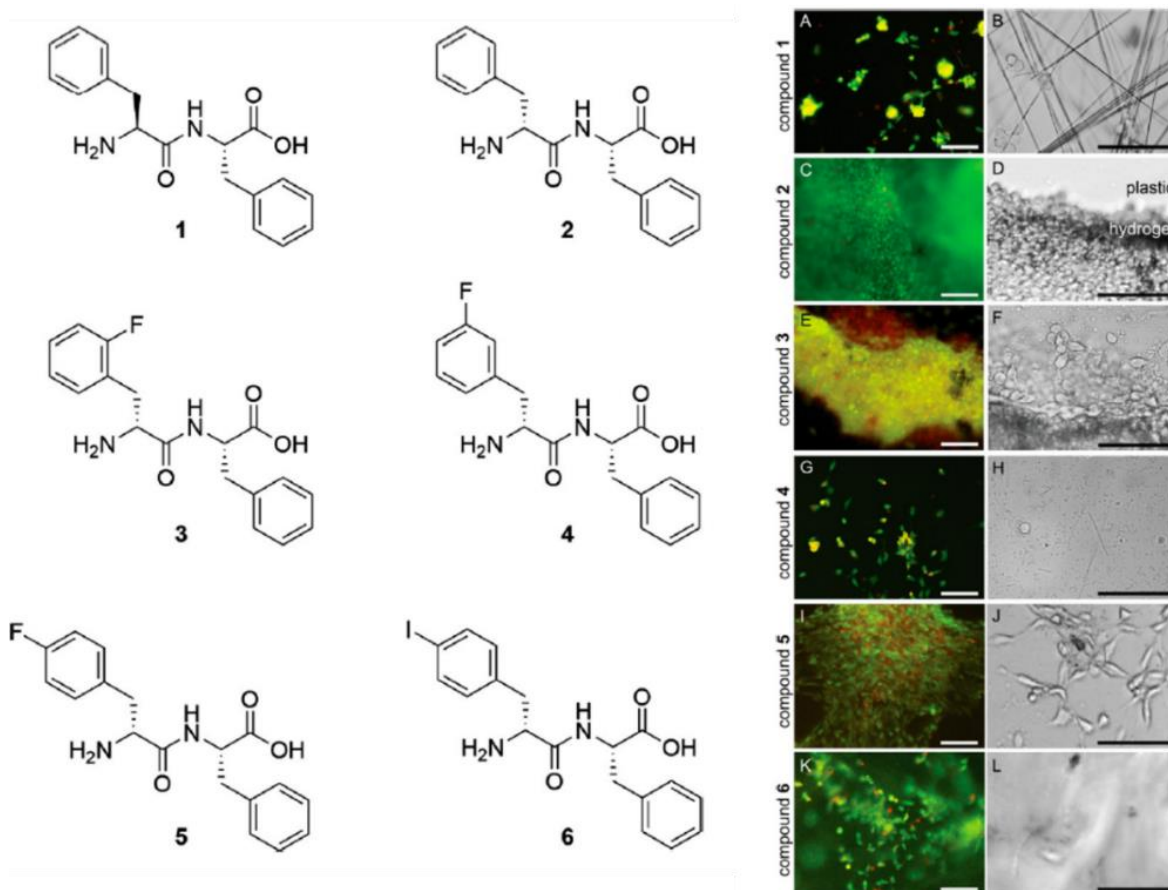


**Figure 7.** (Left) Chemical structure of dipeptides investigated. (Right A–L) Live (green)/dead (red) fluorescence (left,) and bright-field (right) microscopy images of fibroblasts cultured on hydrogels 1–6. Scale bars = 100  $\mu\text{m}$ . Figure adapted from *ACS Nano*, 2020, **14**, 16951-16961.<sup>79</sup>

#### 1.4 Low molecular weight gelators for cell culture

Low molecular weight gelators have several properties which make them appealing for cell culture applications. Firstly, the hierarchical nature of their self-assembly mimics that of the natural ECM, enhancing their biocompatibility.<sup>83</sup> Moreover, they tend to have highly tuneable mechanical properties, allowing the materials produced to closely match the native tissue. This is favourable considering the influence of mechanical properties of cell differentiation and proliferation.<sup>84</sup> Such LMWG can also be designed to include bioactive motifs to promote specific cellular responses.<sup>85</sup> Additionally, the synthesis of LMWG tends to be relatively simple and scalable, therefore they have the potential to be used for cell culture on a large scale. For these reasons, LMWG have been employed for both 2D and 3D cell culture applications in the past.

### 1.4.1 2D Cell Culture

Cells cultured in 2D grow as a monolayer, attaching themselves to the surface of the material they are grown on. (Figure 8a)<sup>86</sup> There are several benefits associated with 2D culture, including its simple and inexpensive nature.<sup>87, 88</sup> By culturing cells in 2D a controlled environment for the cells is created with a uniform substrate surface and even exposure to nutrients and oxygen.<sup>86</sup> As well as this, 2D cultures form quickly and produce high-quality, reproducible long term cultures which are easy to interpret due to their simplicity.<sup>89</sup> Scaling up 2D cultures is also very straightforward allowing the production of high cell numbers when required.<sup>90</sup> Moreover, as cell 2D cell culture has been used for many years, we have access to extensive literature and protocols, providing a solid foundation for experimental design and comparison with previous studies.<sup>87</sup>

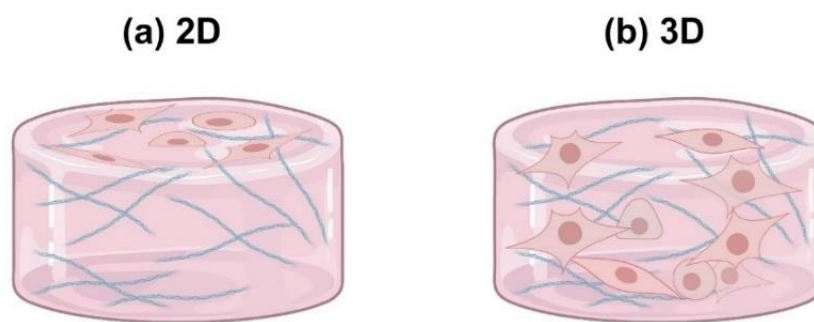


**Figure 8.** Cartoon depicting (a) 2D cell culture where cells are cultured as a monolayer on top of a hydrogel and (b) 3D culture where the cells are cultured within the hydrogel, interacting with each other and their environment.

Drawbacks to using 2D cell culture stem from the monolayer morphology not being representative of the 3D structure of the ECM.<sup>91</sup> This is because cells within the natural ECM interact with neighbouring cells as well as their environment, whereas cells in 2D culture are deprived of such interactions, thus lacking an *in vivo* like microenvironment.<sup>87, 91, 92</sup> Despite these limitations many supramolecular gelators have been implemented as surfaces for 2D culture of cells.<sup>93-96</sup>

With regards to LMWG, there are few literature examples of them for 2D cell culture applications. In fact, 2D culture is often used as a preliminary viability test before 3D culture is attempted. For example, the work of Diba and co-workers describes the formulation of multicomponent dynamic scaffolds.<sup>97</sup> Initially, the hydrogels were used for the 2D culture of human ventricular scar cells (HVSCs) cells before successfully using the materials for 3D culture and spheroid encapsulation.

Likewise, work from Alakpa et al. reports using 2D culture of stem cells on the surface of the hydrogels to examine the effect of stiffness on cell behaviour, before moving towards 3D culture by injecting the pre-gel solution loaded with cells into a collagen matrix.<sup>33</sup> A possible explanation for this shortage of LMWG used for 2D culture is that due to the soft mechanical properties of these materials, cells cultured on the surface may migrate through the gel.<sup>98</sup> Alternatively, it may be due to 3D culture being a more appealing option for researchers.

### 1.4.2 3D Cell Culture

In contrast to 2D cell culture, 3D culture allows cells to grow and interact with other cells and their surrounding material in all three dimensions (Figure 8b).<sup>87</sup> This allows them to be designed in such a way that closely resembles the ECM by creating environmental niches.<sup>99, 100</sup> While the distribution of oxygen and nutrients is less uniform in 3D culture, this can be viewed as an advantage as it is more representative of conditions *in vivo*.<sup>86</sup> Furthermore, the molecular mechanisms and biochemistry of the cells are closer to those of cells within the ECM when 3D culture is used, whereas in 2D culture processes such as gene expression can vary.<sup>101, 102, 103</sup> However, despite the growing popularity of 3D cell culture, a few issues still need to be considered. Firstly, a 3D culture can take a longer duration of time to form in some cases compared to a 2D culture.<sup>87, 104</sup> Once formed, 3D cultures tend to be of worse quality than their 2D counterparts, producing in difficult to interpret, non-reproducible results.<sup>89</sup> Finally, 3D cultures are often significantly more expensive to set up and run compared to 2D cultures and are rarely available for commercial sources.<sup>87, 105, 106</sup>

LMWG have been successfully utilised for 3D cell culture applications. In 2008 Panda et al. reported that the uncapped dipeptide (Phe- $\Delta$ Phe) formed a dense fibril hydrogel network at physiological pH.<sup>96</sup> Including the unsaturated phenylalanine analogue also made the scaffold resistant to proteolysis. The group then went on to demonstrate the potential of this material for 3D culture applications, by showing that cells seeded on the top of the gel were capable of migrating into three (X, Y, Z) planes.<sup>107</sup>

A further example comes from Marchesan and co-workers who manipulated the co-assembly of the antibiotic (ciprofloxacin) with the LMWG <sup>D</sup>Leu-Phe-Phe for the 3D culture of fibroblast cells.<sup>108</sup> A pH trigger was used to form the hydrogels at pH 7.4, before culture of the cells on top of the gels. Infiltration of the network by the fibroblasts was confirmed using a live/dead assay.

Work from Liebmann et al. discussed the potential of Fmoc-FF hydrogels as a platform for 3D cell culture applications.<sup>109</sup> They found that the hydrogel provided an effective scaffold for cell growth in 3D, with cells remaining viable for long-term culture. It was also unveiled that this gelator could be used to create layers, which presents the opportunity to study cell behaviour at an interface (Figure 9a). When astrocytes were cultured in 2D on top of this hydrogel, it was found that the cells exhibited an elongated morphology and large size of around 50  $\mu\text{m}$ . Conversely, when cultured in 3D the cells tended to be smaller in size (10–20  $\mu\text{m}$ ) and presenting a more spherical phenotype closer to that observed in vivo (Figure 9c). This result emphasises the importance of 3D culture to develop physiologically relevant models. However, a solvent switch method was used to trigger the formation of these gels, requiring the dipeptide gelator to be dissolved in DMSO before the dispersion media (PBS) was added. As previously mentioned, the use of organic solvents is not ideal for cell culture application due to their potential to lead to cell death.<sup>49</sup>

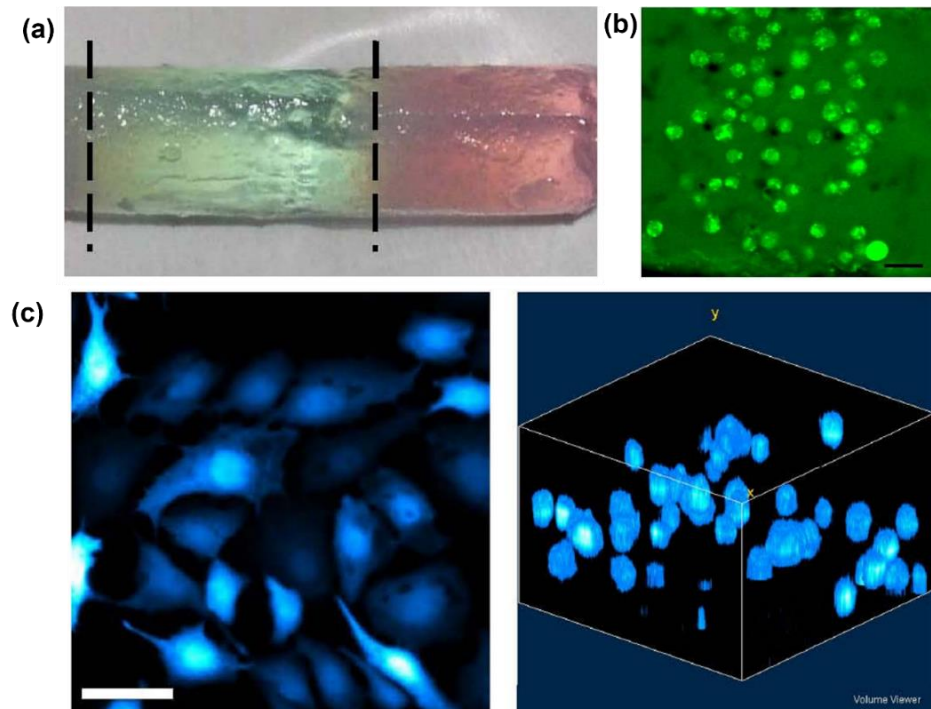


**Figure 9.** (a) Photograph showing layering of the Fmoc-FF hydrogel using different coloured dyes to distinguish between layers. (b) COS-7 astrocyte cells immobilized in a 3D hydrogel within a microchamber composed of silicon microstructures. The scale bar is representative of 30  $\mu\text{m}$ . (c) (left) 2D culture of MDCK astrocytes on a glass substrate. Scale bar is 50  $\mu\text{m}$ . (Right). Growth of same cell line in 3D culture within the hydrogel. Confocal z-stacks were collected at scans of 10  $\mu\text{m}$  increments over total thickness of 160  $\mu\text{m}$ . Figure adapted from *BMC Biotechnology*, 2007, 7, 88.<sup>109</sup>

Another notable example comes from the work of Webber et al, which employs a peptide amphiphile containing the bioactive motif Arg-Gly-Asp-Ser (RGDS) and photocleavable nitrobenzyl group.<sup>110</sup> The study describes using light to trigger the gelation of the peptide for 3D culture by culturing fibroblast cells with the gelator in DMEM. When gelation was triggered, a sol-to-gel transition led to the encapsulation of the cells within the hydrogel. Moreover, once the nitrobenzyl group was cleaved by irradiation, the cell-anchoring RGD group was released. This results in increased biocompatibility of the system due to the higher volume of RGD now present in the system.

## 1.5 Multicomponent LMWG for cell culture

Multicomponent supramolecular self-assembly is a common phenomenon in nature, occurring in biological species including the ECM, cell walls and DNA.<sup>111-113</sup> For this reason, these non-covalent assemblies are of particular interest within the fields of tissue engineering and drug delivery.<sup>113, 114</sup> Moreover, multicomponent supramolecular systems allow access to novel properties compared to the single species they are composed of. Multicomponent systems can be classified as self-sorted or co-assembled.<sup>22, 115</sup> Self-sorted systems display a strong preference for self-combination, resulting in each assembled structure containing only one of the species present (Figure 10a).<sup>116</sup> Conversely, co-assembled structures are composed of a mixture of each component.<sup>117</sup> Co-assembly can occur randomly or specifically. Random co-assembly refers to when the components assemble in an unorganized fashion (Figure 10b). Alternatively, specific co-assembly refers to when the components have a slight affinity towards themselves which causes the components to arrange in an ordered fashion (Figure 10c).<sup>118</sup>

Zhou and co-workers have previously shown that Fmoc-FF and Fmoc-RGD can form multicomponent hydrogel structures suitable for 3D cell culture.<sup>119</sup> Spectroscopic and imaging techniques including CD, FTIR, TEM, AFM and fluorescence revealed that the individual molecules co-assembled via the  $\pi$ - $\pi$  stacking of the Fmoc groups, forming  $\beta$ -sheets.<sup>120</sup> By incorporating Fmoc-RGD into the system, bioactivity was significantly enhanced.<sup>119</sup>

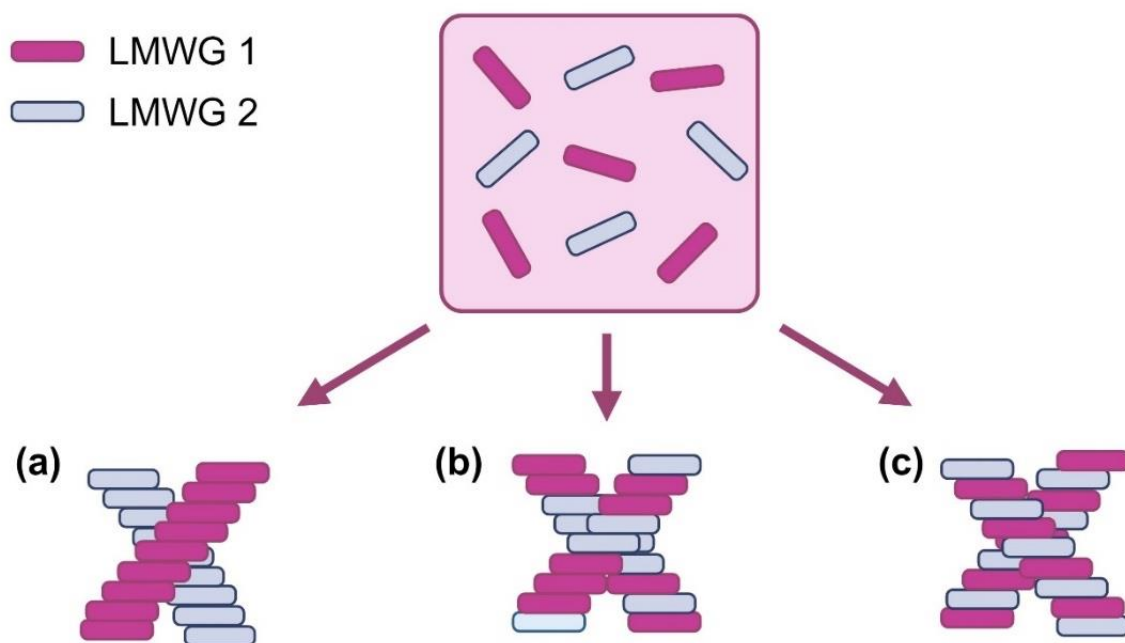


**Figure 10.** Cartoon showing the self-assembly pathways of multicomponent LMWG systems. The LMWG can (a) self-sort (b) randomly co-assemble or (c) co-assemble specifically.

A second example comes from the work of Okesola and co-workers who developed a two-component hydrogel scaffold suitable for the culture of human-adipose-derived stem cells, demonstrating enhanced self-healing and enzyme degradation stability.<sup>121</sup> The components studied were the peptide amphiphiles (PA-E3) and 1,3:2,4-dibenzylidene-D-sorbitol (DBS-COOH). It was reported that the PA-E3 was self-sorting within the network, while DBS-COOH acted as an additive modifier to the fibres. It was also noted that the multicomponent hydrogel exhibits significantly improved biocompatibility in comparison to the signal component systems. Both examples highlight the vast potential of supramolecular multicomponent systems for biological applications in the future. However, further research is necessary as such systems remain challenging to design and to predict if gelation will occur, as even a small change to one component can impact the assembly.<sup>113, 122, 123</sup>

## 1.6 Printing LMWG for cell culture

Another possible route to mimicking the complex nature of the ECM is using 3D printing or bioprinting.<sup>124</sup> There are three main 3D printing techniques used for bioprinting; extrusion-based, inkjet-based and laser-assisted bioprinting. The ease of use and low application cost of extrusion-based bioprinting have made it the most widely employed variation.<sup>125</sup> Firstly, the bioink is loaded into a syringe or cartridge, before being mechanically extruded onto a platform (Figure 11).<sup>126</sup> Despite the popularity of extrusion-based printing, applications may be limited by its low printing resolution and high rate of cell death due to the shear stress experienced by the cells when extruded through the nozzle or needle.<sup>127</sup>

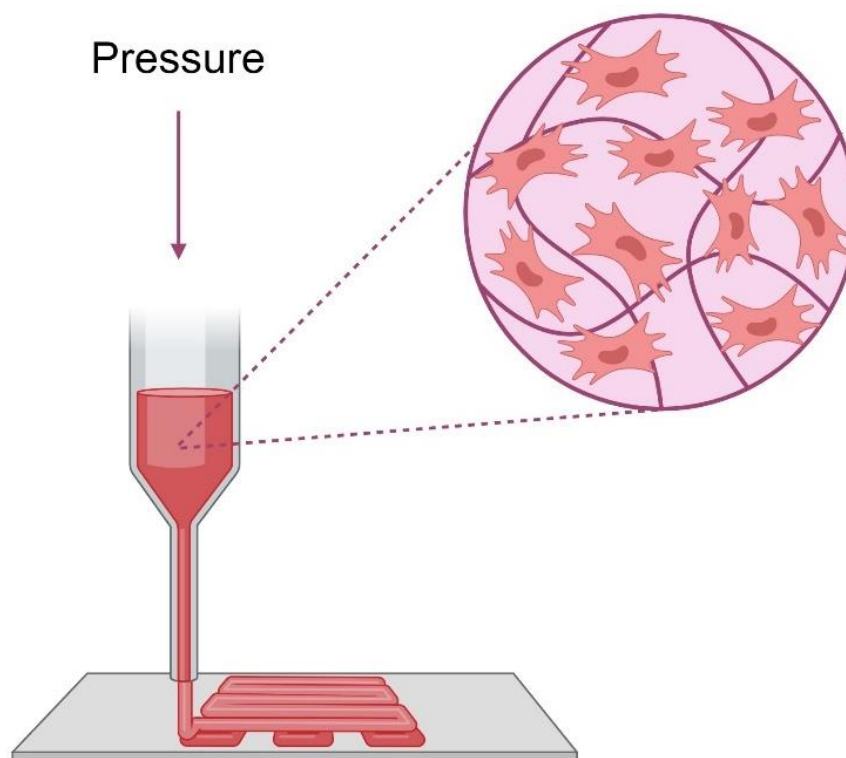


**Figure 11.** Simplified diagram showing the process of extrusion-based bioprinting.

As well as the printing method, the bioink used for 3D printing must also be considered carefully due to the essential criteria for success. The scaffolds formed must exhibit suitable mechanical strength and shape fidelity and be capable of undergoing tuneable gelation. Furthermore, the resulting gel must be biocompatible and ideally suitable for large-scale synthesis with minimal batch-to-batch variation. For these reasons, LMWG are gaining increasing interest within the field of 3D bioprinting. Such gelators have already been used as bioinks for drug delivery matrices and implantable scaffolds.<sup>128, 129</sup>

A study carried out by Susapato et al. demonstrates the use of tetrapeptides (IIFK and IIZK) for use as tuneable bioinks with the ability to produce materials with stiffnesses up to 300 kPa.<sup>130</sup> An advanced automatic printing process was used to print structures using a low concentration of 1 mg/mL of each LMWG in 1X PBS. This low minimum gelation concentration at physiological pH is unusual for such gelators and suggests that the peptides could be promising candidates for large-scale printing experiments. Both gelators underwent co-extrusion with mesenchymal stem cells, resulting in robust scaffolds that were stable over several weeks. In addition to this, the networks produced were used to induce chondrogenic differentiation in the cells.

A further example of peptide-based gelators as bioinks comes from the Domingos group.<sup>131</sup> This work entailed using the peptide gelators Alpha1 and AlphaProB which form soft and stiff hydrogels respectively. Both gelators were printed containing encapsulated epithelial cells which remained viable 7 days post-extrusion according to a live/dead assay. These results were particularly promising as the variation in stiffness of the gelators can be used to promote different cellular responses.

## **1.7 Functionalisation of hydrogels for cell culture**

To elevate the bioactivity of LMWG for cell culture applications and mimic the complex environment of the ECM, biological motifs or additives are often required.<sup>132</sup> The type of functionalisation used is dependent on the cellular aim, which is usually to enhance the adhesion of cells or influence cell signalling. With regards to promoting cell adhesion, the most effective and commonly used motif is the RGD sequence which targets specific integrin-binding proteins on the cell membrane and can be derived from laminin (Figure 12).<sup>133, 134 135</sup> It has been previously discovered that cyclic RGD peptides such as cyclo(RGDfV) (where f represents D-phenylalanine) resulted in superior activity and selectivity in comparison to linear RGD.<sup>136-138</sup> In Chapter 3 of this thesis, we utilise a cyclic variation of this sequence (Upy-cRGD) due to its higher conformation resemblance to fibronectin.<sup>134, 138</sup> Other examples of synthetic integrin targeting motifs include GFOGER and IKVAV, which are derived from collagen and laminin respectively.<sup>140, 141</sup>

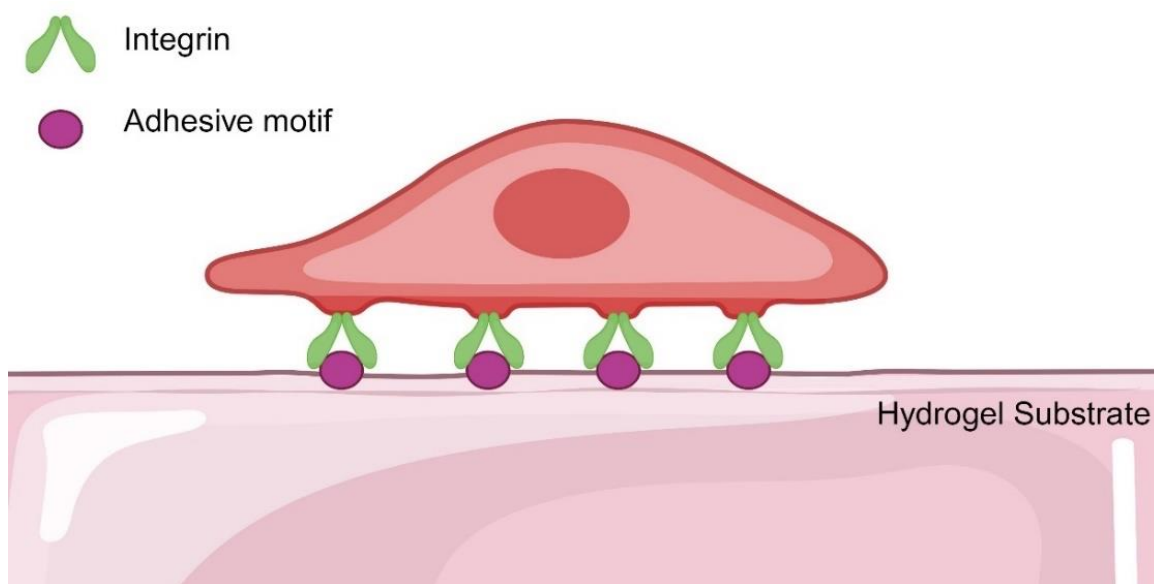


**Figure 12.** Cartoon displaying a simplified interpretation of the integrin binding mechanism between integrin on the cell surface and adhesive motifs added to a hydrogel substrate.

Incorporating proteins such as growth factors into supramolecular systems is a popular way of influencing cell signalling to encourage processes such as cell proliferation, migration and differentiation.<sup>142</sup> Administering such proteins directly into the body would lead to harmful off-target effects due to the poorly controlled release.<sup>143</sup> Moreover, these proteins tend to have short half-lives in vivo and thus would require frequent repeated dosages.<sup>144</sup> For these reasons, supramolecular hydrogels are considered promising candidates for delivering growth factors in a controlled manner.<sup>145</sup> Examples of growth factors that have been incorporated into supramolecular systems for controlled delivery include VEGF to promote angiogenesis,<sup>146, 147</sup> BMP-2 for bone regeneration,<sup>148-150</sup> TGF- $\beta$ 1 for cartilage regeneration<sup>151, 152</sup> and FGF for skin healing.<sup>153</sup>

Unfortunately, there are still limitations when using supramolecular materials to deliver growth factors in vivo or for cell culture applications.<sup>144</sup> One of which is that the mechanical properties of the protein-loaded biomaterial may not have the desired mechanical properties. Alternatively, growth factor activity may decrease upon loading or release from the gel. Lastly, fine control over protein release may not be fully achieved, leading to a burst release effect.<sup>154, 155</sup>

### 1.7.1 PODS®

PODS® (POLYhedrin Delivery Systems) technology from Cell Guidance Systems may offer solutions to the growth factor delivery issues mentioned above. These micron-scale proteins are capable of encapsulating cargo molecules for prolonged periods, before gradually releasing over days or weeks, thus avoiding burst release.<sup>156-157</sup>

Polyhedrin is produced within viruses including baculoviruses and cypoviruses which utilise it to create complex crystal structures (Figure 13).<sup>159</sup> These protein crystals act as armour to protect viruses against environmental conditions such as dehydration, freezing, low pH and UV radiation over many years.<sup>160-164</sup> The PODS® are generated via the self-assembly of polyhedrin into cuboid structures within insect cells infected with baculoviruses or cypoviruses. By manipulating this process, bioengineers have been able to successfully modify the infected insect cells so they express an abundance of polyhedrin. This allows the self-assembling PODS® structures to encapsulate cargo proteins. Degradation of the PODS® takes place via protease-mediated mechanisms which enables the sustained release of the bioactive cargo.<sup>156</sup>

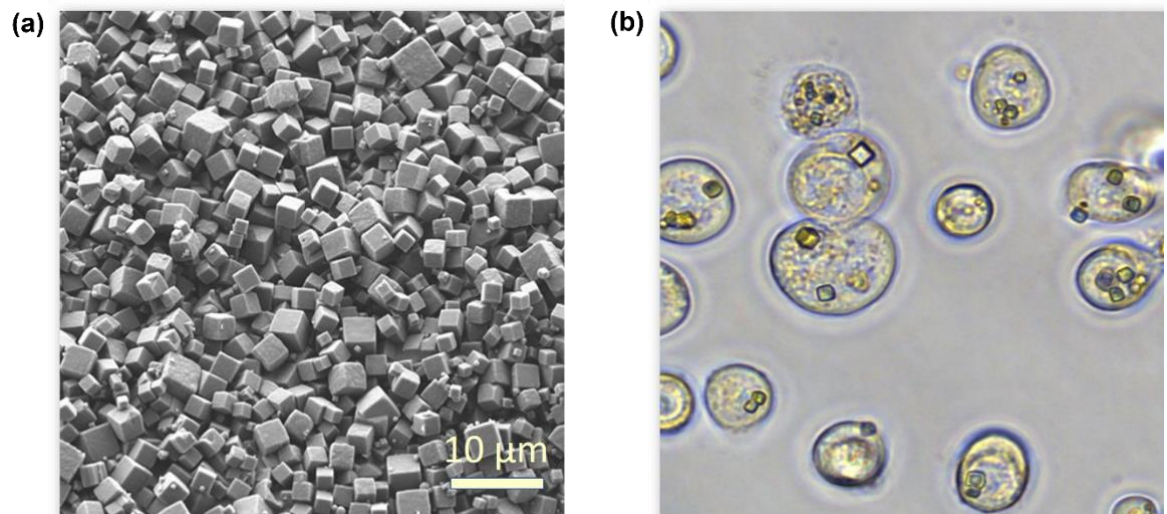


**Figure 13.** (a) SEM image of PODS® (b) Light microscope image of PODS® generating within insect cells. Figure adapted from Cell Guidance Systems, PODS® Technology, <https://www.cellgs.com/pods-technology.htm>, accessed 20<sup>th</sup> August 2024.

Chang and co-workers have previously utilised these PODS® containing brain-derived neurotrophic factor (hBDNF) within a cellulose hydrogel to mimic a stem cell niche within the inner ear.<sup>156</sup> The study revealed that the PODS® provided a gradual and continuous growth factor supply which enhanced the proliferation and differentiation of the cells. Immunohistochemistry was used to confirm this observation.

## 1.8 Aims of this Thesis

Through this thesis, I aim to develop and thoroughly characterise LMWG at physiological pH for cell culture applications. I do this by using a range of techniques to study the materials across different length scales. By doing so, I convey the importance of such characterisation which will aid our understanding of how these systems self-assemble and thus help develop finely controllable novel biomaterials in the future.

In Chapter 2, I describe the development of 2NapFF hydrogels crosslinked with DMEM to produce hydrogel networks at physiological pH. I also investigate the effect of heating and cooling the gelator before gelation is triggered. These systems were characterised across multiple length scales via shear rheology, cavitation rheology, confocal microscopy and small-angle x-ray scattering (SAXS). Furthermore, I examine the effect of incorporating PODS® within the systems and study their effect on fibroblasts when cultured on top of the hydrogels.

I discovered that the PODS® had little impact on the rheological or scattering data, and thus can be used to improve the bioactivity of the systems, without altering the network. A live/dead assay also suggests enhanced mesenchymal stem cell proliferation after 7 days when PODS® were included.

In Chapter 3, I compared the 2NapFF hydrogels crosslinked with DMEM to a Ureido-pyrimidinone (UPy) supramolecular hydrogel system. This UPy system comprises of a monofunctional building block and bifunctional crosslinker species. I examine the effect of combining both systems with and without the UPy crosslinker. By employing SAXS I highlight that the assembly of the combined systems is driven by the UPy component. A combination of rheology and circular dichroism (CD) data showed that when the UPy crosslinker I included in the combined samples, self-sorting of the 2NapFF and UPy components occurred. Cell culture studies also reveal that the crosslinking species was crucial to forming a network to which cells can adhere.

In Chapter 4, I demonstrate that the rheological properties and printability of the 2NapFF hydrogels are heavily influenced by the media used to trigger gelation. The printing conditions for the samples gelled with various types of cell culture media were optimised. Consequently, the samples displaying reproducible, self-supporting structures were used to print macrophage cells which remained within the gel after 24 hours. These findings suggest that these systems could be considered as potential bioink candidates in the future.

**1.9 References**

1. M. Bustamante-Torres, D. Romero-Fierro, B. Arcentales-Vera, K. Palomino, H. Magaña and E. Bucio, *Gels*, 2021, **7**, 182.
2. Y. E. Shapiro, *Prog. Polym. Sci.*, 2011, **36**, 1184-1253.
3. E. M. Ahmed, *J. Adv. Res*, 2015, **6**, 105-121.
4. H. Geckil, F. Xu, X. Zhang, S. Moon and U. Demirci, *Nanomedicine*, 2010, **5**, 469-484.
5. S. Mantha, S. Pillai, P. Khayambashi, A. Upadhyay, Y. Zhang, O. Tao, H. M. Pham and S. D. Tran, *Materials*, 2019, **12**, 3323.
6. N. Angaria, S. Saini, M. S. Hussain, S. Sharma, G. Singh, N. Khurana and R. Kumar, *Int. J. Polym. Mater.*, 2024, **73**, 1174.
7. K. Z. Lee, J. Jeon, B. Jiang, S. V. Subramani, J. Li and F. Zhang, *Molecules*, 2023, **28**, 4988.
8. C. Huerta-López and J. Alegre-Cebollada, *Nanomaterials*, 2021, **11**, 1656.
9. A. Islam, T. Yasin, I. Bano and M. Riaz, *J. Appl. Polym. Sci.*, 2012, **124**, 4184-4192.
10. S. Salave, D. Rana, A. Sharma, K. Bharathi, R. Gupta, S. Khode, D. Benival and N. Kommineni, *Polysaccharides*, 2022, **3**, 625-654.
11. D. A. Gyles, L. D. Castro, J. O. C. Silva and R. M. Ribeiro-Costa, *Eur. Polym. J.*, 2017, **88**, 373-392.
12. X. Guan, M. Avci-Adali, E. Alarçin, H. Cheng, S. S. Kashaf, Y. Li, A. Chawla, H. L. Jang and A. Khademhosseini, *Biotechnol. J.*, 2017, **12**, 1600394.
13. I. M. Garnica-Palafox and F. M. Sánchez-Arévalo, *Carbohydr. Polym.*, 2016, **151**, 1073-1081.
14. R. Cruz-Acuña, M. Quirós, A. E. Farkas, P. H. Dedhia, S. Huang, D. Siuda, V. García-Hernández, A. J. Miller, J. R. Spence, A. Nusrat and A. J. García, *Nat. Cell. Biol.*, 2017, **19**, 1326-1335.
15. J. R. Tse and A. J. Engler, *Curr. Protoc. Cell Biol.*, 2010, **47**, 10.16.11-10.16.16.
16. T. Gao, M. Jiang, X. Liu, G. You, W. Wang, Z. Sun, A. Ma and J. Chen, *Polymers*, 2019, **11**, 171.
17. G. Gao, A. F. Schilling, K. Hubbell, T. Yonezawa, D. Truong, Y. Hong, G. Dai and X. Cui, *Biotechnol. Lett.*, 2015, **37**, 2349-2355.
18. M. P. Lutolf and J. A. Hubbell, *Nat. Biotechnol.*, 2005, **23**, 47-55.
19. S. Manchineella and T. Govindaraju, *ChemPlusChem*, 2017, **82**, 88-106.

20. L. Thomson and D. J. Adams, in *Chemoresponsive Materials: Smart Materials for Chemical and Biological Stimulation*, ed. H.-J. Schneider, The Royal Society of Chemistry, 2022, 96-128.
21. M. Ni and S. Zhuo, *RSC Adv.*, 2019, **9**, 844-852.
22. E. R. Draper and D. J. Adams, *Chem. Soc. Rev.*, 2018, **47**, 3395-3405.
23. J. Omar, D. Ponsford, C. A. Dreiss, T.-C. Lee and X. J. Loh, *Chem. Asian J.*, 2022, **17**, e202200081.
24. R. Dong, Y. Pang, Y. Su and X. Zhu, *Biomater. Sci.*, 2015, **3**, 937-954.
25. Z. Yang, H. Xu and X. Zhao, *Adv. Sci.*, 2020, **7**, 1903718.
26. S. Marchesan, C. D. Easton, F. Kushkaki, L. Waddington and P. G. Hartley, *Chem. Comm.*, 2012, **48**, 2195-2197.
27. S. Marchesan, C. Easton, K. Styan, L. Waddington, F. Kushkaki, L. Goodall, K. McLean, J. Forsythe and P. Hartley, *Nanoscale*, 2014, **6**, 5172-5180.
28. S. Yang, M. Wang, T. Wang, M. Sun, H. Huang, X. Shi, S. Duan, Y. Wu, J. Zhu and F. Liu, *Mater. Today Bio.*, 2023, **20**, 100644.
29. A. P. McCloskey, E. R. Draper, B. F. Gilmore and G. Laverty, *J. Pept. Sci.*, 2017, **23**, 131-140.
30. L. Li, L. Xie, R. Zheng and R. Sun, *Front. Chemi.*, 2021, **9**, 2296-2646.
31. V. B. Kumar, O. S. Tiwari, G. Finkelstein-Zuta, S. Rencus-Lazar and E. Gazit, *Pharm.*, 2023, **15**, 345.
32. Y.-L. Wang, S.-P. Lin, S. R. Nelli, F.-K. Zhan, H. Cheng, T.-S. Lai, M.-Y. Yeh, H.-C. Lin and S.-C. Hung, *Macromol. Biosci.*, 2017, **17**, 1600192.
33. E. V. Alakpa, V. Jayawarna, A. Lampel, K. V. Burgess, C. C. West, C. J. Bakker, S. Roy, N. Javid, S. Fleming, D. A. Lamprou, J. Yang, A. Miller, A. J. Urquhart, P. W. J. M. Frederix, N. T. Hunt, B. Péault, R. V. Ulijn and M. J. Dalby, *Chem*, 2016, **1**, 298-319.
34. W. T. Truong, Y. Su, D. Gloria, F. Braet and P. Thordarson, *Biomater. Sci.*, 2015, **3**, 298-307.
35. B. Ding, Y. Li, M. Qin, Y. Ding, Y. Cao and W. Wang, *Soft Matter*, 2013, **9**, 4672-4680.
36. Y. Qiao, Y. Lin, Z. Yang, H. Chen, S. Zhang, Y. Yan and J. Huang, *J. Phys. Chem. B*, 2010, **114**, 11725-11730.
37. V. Jayawarna, M. Ali, T. A. Jowitt, A. F. Miller, A. Saiani, J. E. Gough and R. V. Ulijn, *Adv. Mater.*, 2006, **18**, 611-614.

38. A. Mahler, M. Reches, M. Rechter, S. Cohen and E. Gazit, *Adv. Mater.*, 2006, **18**.
39. R. Vegners, I. Shestakova, I. Kalvinsh, R. M. Ezzell and P. A. Janmey, *J. Pept. Sci.*, 1995, **1**, 371-378.
40. Q. Liu, H. Wang, G. Li, M. Liu, J. Ding, X. Huang, W. Gao and W. Huayue, *Chinese Chem. Lett.*, 2019, **30**, 485-488.
41. C. Muller, A. Ontani, A. Bigo-Simon, P. Schaaf and L. Jierry, *Adv. Colloid Interface Sci.*, 2022, **304**, 102660.
42. A. Fortunato and M. Mba, *Gels*, 2021, **7**, 85.
43. F. Tantakitti, J. Boekhoven, X. Wang, R. V. Kazantsev, T. Yu, J. Li, E. Zhuang, R. Zandi, J. H. Ortony, C. J. Newcomb, L. C. Palmer, G. S. Shekhawat, M. O. de la Cruz, G. C. Schatz and S. I. Stupp, *Nat Mater*, 2016, **15**, 469-476.
44. L. Chen, K. Morris, A. Laybourn, D. Elias, M. R. Hicks, A. Rodger, L. Serpell and D. J. Adams, *Langmuir*, 2010, **26**, 5232-5242.
45. L. Chen, S. Revel, K. Morris, L. C. Serpell and D. J. Adams, *Langmuir*, 2010, **26**, 13466-13471.
46. L. Chen, J. Raeburn, S. Sutton, D. G. Spiller, J. Williams, J. S. Sharp, P. C. Griffiths, R. K. Heenan, S. M. King, A. Paul, S. Furzeland, D. Atkins and D. J. Adams, *Soft Matter*, 2011, **7**, 9721-9727.
47. F. M. Menger and K. L. Caran, *J. Am. Chem. Soc.*, 2000, **122**, 11679-11691.
48. G. F. Liu, D. Zhang and C. L. Feng, *Angew Chem. Int. Ed. Engl.*, 2014, **53**, 7789-7793.
49. X. Chen and S. Thibeault, *Annu Int. Conf. IEEE Eng. Med. Biol. Soc.*, 2013, 6228-6231.
50. J. Cui, A. Liu, Y. Guan, J. Zheng, Z. Shen and X. Wan, *Langmuir*, 2010, **26**, 3615-3622.
51. B. Hansda, J. Majumder, B. Mondal, A. Chatterjee, S. Das, S. Kumar, R. Gachhui, V. Castelletto, I. W. Hamley, P. Sen and A. Banerjee, *Langmuir*, 2023, **39**, 7307-7316.
52. E. R. Draper and D. J. Adams, *Langmuir*, 2019, **35**, 6506-6521.
53. I. A. Duceac, L. Verestiuc, C. D. Dimitriu, V. Maier and S. Coseri, *Polymers*, 2020, **12**, 1473.
54. E. R. Draper and D. J. Adams, *Chem. Commun.*, 2016, **52**, 8196-8206.
55. K. Tamaki, T. Utaka, H. Takase, Y. Eriyama and T. Ukachi, *J. Photopolym. Sci. Technol.*, 2003, **16**, 9-11.

56. E. R. Draper, E. G. Eden, T. O. McDonald and D. J. Adams, *Nat. Chem.*, 2015, **7**, 848-852.
57. T. D. Sargeant, C. Aparicio, J. E. Goldberger, H. Cui and S. I. Stupp, *Acta. Biomater.*, 2012, **8**, 2456-2465.
58. S. Das, H. Horo, U. Goswami and L. M. Kundu, *ChemistrySelect*, 2019, **4**, 6778-6783.
59. R. Masuma, S. Kashima, M. Kurasaki and T. Okuno, *J. Photochem. and Photobiol.*, 2013, **125**, 202-208.
60. T. M. Runger, *J. Invest. Dermatol.*, 2007, **127**, 2103-2105.
61. D. K. Smith, *Soft Matter*, 2024, **20**, 10-70.
62. M. D. Segarra-Maset, V. J. Nebot, J. F. Miravet and B. Escuder, *Chem. Soc. Rev.*, 2013, **42**, 7086-7098.
63. J. Qi, Y. Yan, B. Cheng, L. Deng, Z. Shao, Z. Sun and X. Li, *ACS Appl. Mater. Interfaces*, 2018, **10**, 6180-6189.
64. A. S. Carlini, R. Gaetani, R. L. Braden, C. Luo, K. L. Christman and N. C. Gianneschi, *Nat. Commun.*, 2019, **10**, 1735.
65. Y. Zhong, J. Zhan, G. Xu, Y. Chen, Q. Qin, X. Liao, S. Ma, Z. Yang and Y. Cai, *Angew. Chem. Int. Ed.*, 2021, **60**, 8121-8129.
66. T. Xu, Y. Cai, X. Zhong, L. Zhang, D. Zheng, Z. Gao, X. Pan, F. Wang, M. Chen and Z. Yang, *Chem. Commun.*, 2019, **55**, 7175-7178.
67. T. Jiang, Y. Ma, X. Xu, Q. Ji, M. Feng, C. Cheng, Y. Feng, B. He and R. Mo, *Acta Pharm. Sin. B*, 2021, **11**, 2070-2079.
68. Y. Tian, H. Wang, Y. Liu, L. Mao, W. Chen, Z. Zhu, W. Liu, W. Zheng, Y. Zhao, D. Kong, Z. Yang, W. Zhang, Y. Shao and X. Jiang, *Nano Letters*, 2014, **14**, 1439-1445.
69. J. E. P. Brouns and P. Y. W. Dankers, *Biomacromolecules*, 2021, **22**, 4-23.
70. F. Zhao, C. S. Weitzel, Y. Gao, H. M. Browdy, J. Shi, H.-C. Lin, S. T. Lovett and B. Xu, *Nanoscale*, 2011, **3**, 2859-2861.
71. S. Toledano, R. J. Williams, V. Jayawarna and R. V. Ulijn, *J. Am. Chem. Soc.*, 2006, **128**, 1070-1071.
72. L. Chronopoulou, A. R. Togna, G. Guarguaglini, G. Masci, F. Giammaruco, G. I. Togna and C. Palocci, *Soft Matter*, 2012, **8**, 5784-5790.
73. W. Liwinska, E. Waleka-Bagiel, Z. Stojek, M. Karbarz and E. Zabost, *Drug Deliv.*, 2022, **29**, 2561-2578.

74. Y. Li, J. S. Lee, A. R. Kirtane, M. Li, C. W. Coffey, 3rd, K. Hess, A. Lopes, J. Collins, S. Tamang, K. Ishida, A. Hayward, J. Wainer, A. J. Wentworth and G. Traverso, *Adv. Healthc. Mater.*, 2023, **12**, e2301033.
75. V. Nele, C. E. Schutt, J. P. Wojciechowski, W. Kit-Anan, J. J. Douth, J. P. K. Armstrong and M. M. Stevens, *Adv. Mater.*, 2020, **32**, 1905914.
76. L. Chen, G. Pont, K. Morris, G. Lotze, A. Squires, L. C. Serpell and D. J. Adams, *Chem. Commun.*, 2011, **47**, 12071-12073.
77. L. Chen, T. O. McDonald and D. J. Adams, *RSC Adv.*, 2013, **3**, 8714-8720.
78. E. R. Draper and D. J. Adams, *Chem*, 2017, **3**, 390-410.
79. S. Kralj, O. Bellotto, E. Parisi, A. M. Garcia, D. Iglesias, S. Semeraro, C. Deganutti, P. D'Andrea, A. V. Vargiu, S. Geremia, R. De Zorzi and S. Marchesan, *ACS Nano*, 2020, **14**, 16951-16961.
80. J. Zhang, J. Ke, Y. Zhu, J. Song, J. Yang, C. Wen and L. Zhang, *Biomed. Mater.*, 2020, **15**, 015003.
81. V. Chimirso, S. Conti, P. Kong, C. Fodor and W. P. Meier, *Soft Matter*, 2021, **17**, 715-723.
82. S. Marchesan, C. D. Easton, K. E. Styan, L. J. Waddington, F. Kushkaki, L. Goodall, K. M. McLean, J. S. Forsythe and P. G. Hartley, *Nanoscale*, 2014, **6**, 5172-5180.
83. O. El Hamoui, T. Saydé, I. Svahn, A. Gudin, E. Gontier, P. Le Coustumer, J. Verget, P. Barthélémy, K. Gaudin, S. Battu, G. Lespes and B. Alies, *ACS Biomater. Sci. Eng.*, 2022, **8**, 3387-3398.
84. S.-B. Han, J.-K. Kim, G. Lee and D.-H. Kim, *Adv. Biosyst.*, 2020, **4**, 2000247.
85. J. Y. C. Lim, Q. Lin, K. Xue and X. J. Loh, *Materials Today Adv.*, 2019, **3**, 100021.
86. S. Breslin and L. O'Driscoll, *Drug Discov. Today*, 2013, **18**, 240-249.
87. M. Kapalczyńska, T. Kolenda, W. Przybyła, M. Zajączkowska, A. Teresiak, V. Filas, M. Ibbs, R. Bliźniak, Ł. Łuczewski and K. Lamperska, *Arch. Med. Sci.*, 2018, **14**, 910-919.
88. B. B. Aggarwal, D. Danda, S. Gupta and P. Gehlot, *Biochem. Pharmacol.*, 2009, **78**, 1083-1094.
89. J. A. Hickman, R. Graeser, R. de Hoogt, S. Vidic, C. Brito, M. Gutekunst and H. van der Kuip, *Biotechnol. J.*, 2014, **9**, 1115-1128.
90. S. Tohyama, J. Fujita, C. Fujita, M. Yamaguchi, S. Kanaami, R. Ohno, K. Sakamoto, M. Kodama, J. Kurokawa, H. Kanazawa, T. Seki, Y. Kishino, M. Okada, K.

- Nakajima, S. Tanosaki, S. Someya, A. Hirano, S. Kawaguchi, E. Kobayashi and K. Fukuda, *Stem Cell Rep.*, 2017, **9**, 1406-1414.
91. P. M. Gilbert, K. L. Havenstrite, K. E. Magnusson, A. Sacco, N. A. Leonardi, P. Kraft, N. K. Nguyen, S. Thrun, M. P. Lutolf and H. M. Blau, *Science*, 2010, **329**, 1078-1081.
92. M. J. Bissell, A. Rizki and I. S. Mian, *Curr. Opin. Cell Biol.*, 2003, **15**, 753-762.
93. Y. Yuan, Y. Shi, J. Banerjee, A. Sadeghpour and H. S. Azevedo, *Mater. Today Bio.*, 2023, **19**, 100598.
94. A. M. Garcia, D. Iglesias, E. Parisi, K. E. Styan, L. J. Waddington, C. Deganutti, R. De Zorzi, M. Grassi, M. Melchionna, A. V. Vargiu and S. Marchesan, *Chem*, 2018, **4**, 1862-1876.
95. E. V. Alakpa, V. Jayawarna, K. E. V. Burgess, C. C. West, B. Péault, R. V. Ulijn and M. J. Dalby, *Sci. Rep.*, 2017, **7**, 6895.
96. J. J. Panda, A. Mishra, A. Basu and V. S. Chauhan, *Biomacromolecules*, 2008, **9**, 2244-2250.
97. M. Diba, S. Spaans, S. I. S. Hendrikse, M. M. C. Bastings, M. J. G. Schotman, J. F. van Sprang, D. J. Wu, F. J. M. Hoeben, H. M. Janssen and P. Y. W. Dankers, *Adv. Mater.*, 2021, **33**, e2008111.
98. A. A. Solbu, D. Caballero, S. Damigos, S. C. Kundu, R. L. Reis, Ø. Halaas, A. S. Chahal and B. L. Strand, *Mater. Today Bio.*, 2023, **18**, 100537.
99. J. Lee, M. J. Cuddihy and N. A. Kotov, *Tissue Eng. Part B Rev.*, 2008, **14**, 61-86.
100. J. Ham, L. Lever, M. Fox and M. R. Reagan, *JBMR Plus*, 2019, **3**, e10228.
101. S. Ghosh, G. C. Spagnoli, I. Martin, S. Ploegert, P. Demougin, M. Heberer and A. Reschner, *J. Cell. Physiol.*, 2005, **204**, 522-531.
102. M. J. Gómez-Lechón, R. Jover, T. Donato, X. Ponsoda, C. Rodriguez, K. G. Stenzel, R. Klocke, D. Paul, I. Guillén and R. Bort, *J. Cell. Physiol.*, 1998, **177**, 553-562.
103. M. J. Powers, D. M. Janigian, K. E. Wack, C. S. Baker, D. B. Stolz and L. G. Griffith, *Tissue Eng.*, 2002, **8**, 499-513.
104. S.-F. Chen, Y.-C. Chang, S. Nieh, C.-L. Liu, C.-Y. Yang and Y.-S. Lin, *PloS one*, 2012, **7**, e31864.
105. T. R. Sodunke, K. K. Turner, S. A. Caldwell, K. W. McBride and M. J. Reginato, *Biomaterials*, 2007, **28**, 4006-4016.
106. L.-B. Weiswald, D. Bellet and V. Danglès-Marie, *Neoplasia*, 2015, **17**, 1-15.

107. J. J. Panda, R. Dua, A. Mishra, B. Mitra and V. S. Chauhan, *ACS Appl. Mater. Interfaces*, 2010, **2**, 2839-2848.
108. S. Marchesan, Y. Qu, L. J. Waddington, C. D. Easton, V. Glattauer, T. J. Lithgow, K. M. McLean, J. S. Forsythe and P. G. Hartley, *Biomaterials*, 2013, **34**, 3678-3687.
109. T. Liebmann, S. Rydholm, V. Akpe and H. Brismar, *BMC Biotechnol.*, 2007, **7**, 88.
110. M. J. Webber, E. J. Berns and S. I. Stupp, *Isr. J. Chem.*, 2013, **53**, 530-554.
111. D. Wu, H. Lei, X. Xie, L. Zhou, P. Zheng, Y. Cao and Y. Zhang, *Nano Research*, 2022, **15**, 4294-4301.
112. P. Xing, H. P. Tham, P. Li, H. Chen, H. Xiang and Y. Zhao, *Adv. Sci.*, 2018, **5**, 1700552.
113. L. Li, R. Zheng and R. Sun, *J. Adv. Res.*, 2024, **54**, 45-54.
114. X. Jia and K. L. Kiick, *Macromol. Biosci.*, 2009, **9**, 140-156.
115. L. Li, R. Sun and R. Zheng, *Mater. Des.*, 2021, **197**, 109209.
116. B. Adelizzi, N. J. Van Zee, L. N. J. de Windt, A. R. A. Palmans and E. W. Meijer, *J. Am. Chem. Soc.*, 2019, **141**, 6110-6121.
117. P. Makam and E. Gazit, *Chem. Soc. Rev.*, 2018, **47**, 3406-3420.
118. L. J. Marshall, S. Bianco, R. E. Ginesi, J. Douth, E. R. Draper and D. J. Adams, *Soft Matter*, 2023, **19**, 4972-4981.
119. M. Zhou, A. M. Smith, A. K. Das, N. W. Hodson, R. F. Collins, R. V. Ulijn and J. E. Gough, *Biomaterials*, 2009, **30**, 2523-2530.
120. A. M. Smith, R. J. Williams, C. Tang, P. Coppo, R. F. Collins, M. L. Turner, A. Saiani and R. V. Ulijn, *Adv. Mater.*, 2008, **20**, 37-41.
121. B. O. Okesola, Y. Wu, B. Derkus, S. Gani, D. Wu, D. Knani, D. K. Smith, D. J. Adams and A. Mata, *Chem. Mater.*, 2019, **31**, 7883-7897.
122. X. Cao, A. Gao, J.-t. Hou and T. Yi, *Coord. Chem. Rev.*, 2021, **434**, 213792.
123. A. R. Hirst, I. A. Coates, T. R. Boucheteau, J. F. Miravet, B. Escuder, V. Castelletto, I. W. Hamley and D. K. Smith, *J. Am. Chem. Soc.*, 2008, **130**, 9113-9121.
124. K. Wang, Z. Wang, H. Hu and C. Gao, *Supramol. Mater.*, 2022, **1**, 100006.
125. L. M. C. Jesús M. Rodríguez Rego, Antonio Macías García, Alfonso C. Marcos Romero, *Int. J. Bioprinting*, 2023, 437-449.
126. X. B. Chen, A. Fazel Anvari-Yazdi, X. Duan, A. Zimmerling, R. Gharraei, N. K. Sharma, S. Sweilem and L. Ning, *Bioact. Mater.*, 2023, **28**, 511-536.
127. J. Gong, C. C. L. Schuurmans, A. M. v. Genderen, X. Cao, W. Li, F. Cheng, J. J. He, A. López, V. Huerta, J. Manríquez, R. Li, H. Li, C. Delavaux, S. Sebastian, P. E.

- Capendale, H. Wang, J. Xie, M. Yu, R. Masereeuw, T. Vermonden and Y. S. Zhang, *Nat. Commun.*, 2020, **11**, 1267.
128. Y. Loo, A. Lakshmanan, M. Ni, L. L. Toh, S. Wang and C. A. E. Hauser, *Nano Letters*, 2015, **15**, 6919-6925.
129. Y. Loo, S. Zhang and C. A. Hauser, *Biotechnol. Adv.*, 2012, **30**, 593-603.
130. H. H. Susapto, D. Alhattab, S. Abdelrahman, Z. Khan, S. Alshehri, K. Kahin, R. Ge, M. Moretti, A.-H. Emwas and C. A. E. Hauser, *Nano Letters*, 2021, **21**, 2719-2729.
131. B. Raphael, T. Khalil, V. Workman, A. Smith, C. Brown, C. Streulli, A. Saiani and M. Domingos, *Materials Letters*, 2016, **190**, 103-106.
132. L. Rijns, M. B. Baker and P. Y. W. Dankers, *J. Am. Chem. Soc.*, 2024, **146**, 17539-17558.
133. J. Gailit, C. Clarke, D. Newman, M. G. Tonnesen, M. W. Mosesson and R. A. Clark, *Exp. Cell. Res.*, 1997, **232**, 118-126.
134. X. Dai, Z. Su and J. O. Liu, *Tetrahedron Lett.*, 2000, **41**, 6295-6298.
135. T. G. Kapp, F. Rechenmacher, S. Neubauer, O. V. Maltsev, E. A. Cavalcanti-Adam, R. Zarka, U. Reuning, J. Notni, H. J. Wester, C. Mas-Moruno, J. Spatz, B. Geiger and H. Kessler, *Sci Rep*, 2017, **7**, 39805.
136. I. W. Hamley, *Chem. Rev.*, 2017, **117**, 14015-14041.
137. M. Aumailley, M. Gurrath, G. Müller, J. Calvete, R. Timpl and H. Kessler, *FEBS Lett.*, 1991, **291**, 50-54.
138. D. Heckmann and H. Kessler, *Methods Enzymol.*, 2007, **426**, 463-503.
139. B. S. Ludwig, H. Kessler, S. Kossatz and U. Reuning, *Cancers*, 2021, **13**.
140. C. G. Knight, L. F. Morton, A. R. Peachey, D. S. Tuckwell, R. W. Farndale and M. J. Barnes, *J. Biol. Chem.*, 2000, **275**, 35-40.
141. K. Tashiro, G. C. Sephel, B. Weeks, M. Sasaki, G. R. Martin, H. K. Kleinman and Y. Yamada, *J. Biol. Chem.*, 1989, **264**, 16174-16182.
142. G. Janarthanan, S. K. Uthaman, K. Murugesu and S. Vijayavenkataraman, *Int. J. Bioprinting*, 2024, **10**, 1-37.
143. T. N. Vo, F. K. Kasper and A. G. Mikos, *Adv. Drug Deliv. Rev.*, 2012, **64**, 1292-1309.
144. Y. Lyu and H. S. Azevedo, *Molecules*, 2021, **26**, 873.
145. A. J. Feliciano, C. van Blitterswijk, L. Moroni and M. B. Baker, *Acta Biomater.*, 2021, **124**, 1-14.
146. T. Fernández-Muiños, L. Recha-Sancho, P. López-Chicón, C. Castells-Sala, A. Mata and C. E. Semino, *Acta Biomater.*, 2015, **16**, 35-48.

147. B. Cheng, Y. Yan, J. Qi, L. Deng, Z.-W. Shao, K.-Q. Zhang, B. Li, Z. Sun and X. Li, *ACS Appl. Mater. Interfaces*, 2018, **10**, 12474-12484.
148. H. H. Lu, S. D. Subramony, M. K. Boushell and X. Zhang, *Ann. Biomed. Eng.*, 2010, **38**, 2142-2154.
149. S. Hou, X. Wang, S. Park, X. Jin and P. X. Ma, *Adv. Healthc. Mater.*, 2015, **4**, 1491-1495.
150. S. S. Lee, E. L. Hsu, M. Mendoza, J. Ghodasra, M. S. Nickoli, A. Ashtekar, M. Polavarapu, J. Babu, R. M. Riaz, J. D. Nicolas, D. Nelson, S. Z. Hashmi, S. R. Kaltz, J. S. Earhart, B. R. Merk, J. S. McKee, S. F. Bairstow, R. N. Shah, W. K. Hsu and S. I. Stupp, *Adv. Healthc. Mater.*, 2015, **4**, 131-141.
151. R. N. Shah, N. A. Shah, M. M. Del Rosario Lim, C. Hsieh, G. Nuber and S. I. Stupp, *Proc. Natl. Acad. Sci.*, 2010, **107**, 3293-3298.
152. K. Wei, M. Zhu, Y. Sun, J. Xu, Q. Feng, S. Lin, T. Wu, J. Xu, F. Tian, G. Li and L. Bian, *Macromolecules*, 2016, **49**, 866-875.
153. X. Xuan, Y. Zhou, A. Chen, S. Zheng, Y. An, H. He, W. Huang, Y. Chen, Y. Yang, S. Li, T. Xuan, J. Xiao, X. Li and J. Wu, *J. Mater. Chem. B*, 2020, **8**, 1359-1370.
154. B. H. Shan and F. G. Wu, *Adv. Mater.*, 2024, **36**, e2210707.
155. S. Meissner, S. Rees, L. Nguyen, B. Connor, D. Barker, B. Harland, B. Raos and D. Svirskis, *Biomater. Adv.*, 2024, **159**, 213837.
156. H.-T. Chang, R. A. Heuer, A. M. Oleksijew, K. S. Coots, C. B. Roque, K. T. Nella, T. L. McGuire and A. J. Matsuoka, *Acta Biomater.*, 2020, **108**, 111-127.
157. X. Ji, G. Sutton, G. Evans, D. Axford, R. Owen and D. I. Stuart, *EMBO J.*, 2010, **29**, 505-514.
158. Y. Matsuzaki, R. Maruta, K. Takaki, E. Kotani, Y. Kato, R. Yoshimura, Y. Endo, C. Whitty, C. Pernstich, R. Gandhi, M. Jones and H. Mori, *Biomolecules*, 2019, **9**.
159. H. Mori, R. Ito, H. Nakazawa, M. Sumida, F. Matsubara and Y. Minobe, *J. Gen. Virol.*, 1993, **74**, 99-102.
160. F. Coulibaly, E. Chiu, S. Gutmann, C. Rajendran, P. W. Haebel, K. Ikeda, H. Mori, V. K. Ward, C. Schulze-Briese and P. Metcalf, *Proc. Natl. Acad. Sci. U S A*, 2009, **106**, 22205-22210.
161. G. Rohrmann, *J. Gene. Virol.*, 1986, **67**, 1499-1513.
162. S. Abe, B. Maity and T. Ueno, *Chem. Commun.*, 2016, **52**, 6496-6512.
163. K. A. K. Parwana, P. Kaur Gill, R. Njanike, H. H. P. Yiu, C. F. Adams, D. M. Chari and S. I. Jenkins, *Materials*, 2024, **17**, 2330.

Chapter 1

164. A. M. Healy, Z. A. Worku, D. Kumar and A. M. Madi, *Adv. Drug Deliv. Rev.*, 2017, **117**, 25-46.

## **Chapter 2: Materials and Methods**

## Chapter 2

### 2.1 Materials

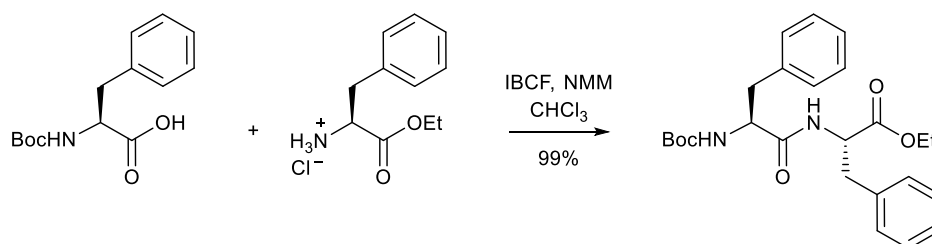
Experiments carried out in Chapter 3 used media purchased from ThermoFisher Scientific include; DMEM (Thermo, cat.no. 1196602). DMEM + glucose samples refer to Dulbecco's Modified Eagle's Medium (DMEM), with 4500 mg/L glucose and sodium pyruvate (Sigma, D5671-500ML) which was purchased from Sigma Aldrich. The gerlator 2NapFF used throughout this thesis was synthesised as described below.

Chapter 4 uses d-2NapFF which was synthesised as previously described by B. Dietrich<sup>1</sup> and used as received. BF-PEG-UPy, UPy-G and UPy-cRGD, were synthesised by SyMO-Chem and used without further purification. All solvents were of AR quality and purchased from Biosolve. Water was purified on an EMD Millipore Milli-Q Integral Water Purification System.

The work carried out in Chapter 5 utilised media purchased from ThermoFisher Scientific include; DMEM (Thermo, cat.no. 1196602) or RPMI 1640 (Thermo, cat.no. 11875093), DMEM F12 (Thermo, cat.no. 11320033), IDIM (Thermo, cat.no. 12440053), HPLM (Thermo, cat.no. A4899101) and Medium 199 (Thermo, cat.no. 11150059). DMEM + glucose samples refer to Dulbecco's Modified Eagle's Medium (DMEM), with 4500 mg/L glucose and sodium pyruvate (Sigma, D5671-500ML) which was purchased from Sigma Aldrich.

### 2.2 2NapFF synthesis

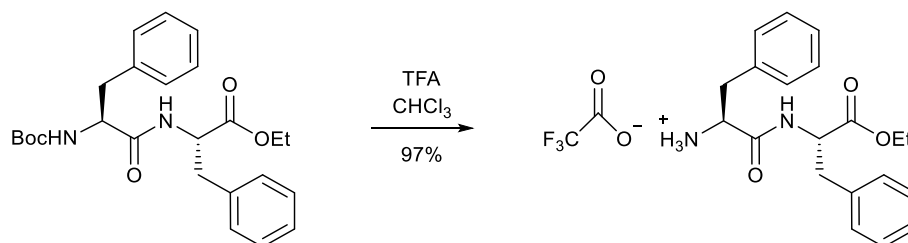
All materials were purchased from commercial suppliers and used as received. The synthesis of 2NapFF was carried out as described previously.<sup>2</sup>



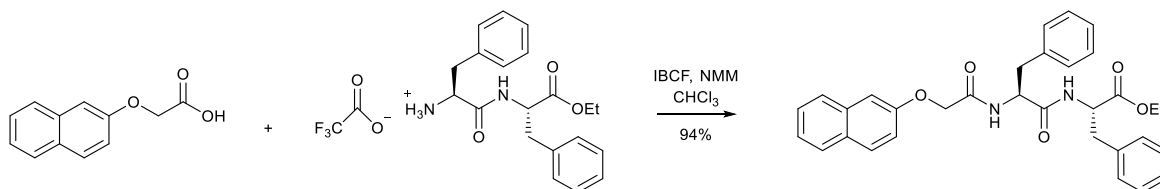
A solution of Boc-L-phenylalanine (5.28 g, 19.9 mmol) in chloroform (50 mL) was prepared. Both iso-butyl chloroformate (1 eq, 2.58 mL) and *N*-methylmorpholine (1 eq, 2.19 mL) were added and allowed to stir for one hour. After this time, L-phenylalanine ethyl ester hydrochloride (1 eq, 4.57 g) and *N*-methylmorpholine (1 eq, 2.19 mL) were then added and the mixture was stirred overnight.

## Chapter 2

The following morning, the clear solution was diluted with chloroform (100 mL) and washed in turn with 1M hydrochloric acid (100 mL), water (100 mL), and brine (100 mL), dried ( $\text{MgSO}_4$ ), and the solvent removed by evaporation under reduced pressure. The crude product was obtained as an off-white solid (8.79 g, 99 %) and used in the next step without further purification.

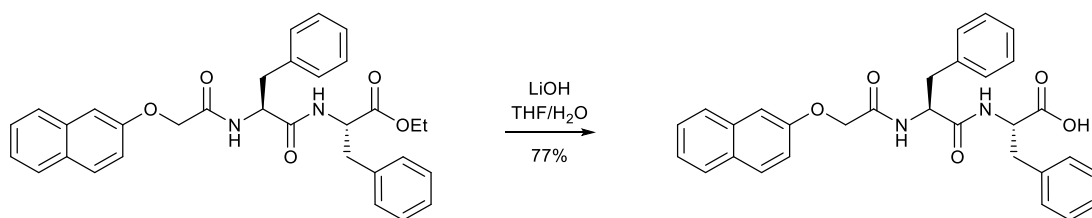


The off-white solid was dissolved in chloroform (30 mL) and trifluoroacetic acid (15 mL, approx. 10 eq) was added and the solution was stirred overnight. After this time, the reaction was concentrated under reduced pressure to remove most of the excess TFA. The resulting viscous orange oil was re-dissolved in chloroform (30 mL), poured into diethyl ether (ca. 500 mL) and stirred overnight. The precipitate was collected by filtration, washed on the filter with a few small portions of diethyl ether and dried under reduced pressure. A white solid was obtained (7.51g, 83 %).



A suspension of 2-naphthoxyacetic acid (3.55 g, 18.0 mmol) in chloroform (50 mL) was prepared and iso-butyl chloroformate (1 eq, 2.28 mL) and *N*-methylmorpholine (1 eq, 1.65 mL) were added and stirred for one hour. A mixture of the product from the previous step (1 eq, 6.82 g) and *N*-methylmorpholine (1 eq, 1.93 mL) in chloroform (50 mL) was then added and the reaction was stirred overnight at room temperature. After this time, the reaction mixture was diluted with chloroform (100 mL) and washed in turn with 1M hydrochloric acid (100 mL), saturated aqueous sodium carbonate solution (100 mL), water (100 mL), and brine (100 mL). After drying over  $\text{MgSO}_4$ , the solvent was removed by evaporation in vacuo, and the crude product was obtained as a light-brown solid (8.62 g, 94 %). This was used in the next step without further purification.

## Chapter 2



To a solution of the light-brown solid (8.62, 16 mmol) in tetrahydrofuran (100 mL) a solution of lithium hydroxide (4 eq, 1.53 g) in water (100 mL) was added and the cloudy mixture was stirred overnight. After this time, the resulting clear solution was poured into 1M hydrochloric acid (500mL) and stirred for 90 minutes. The precipitate was collected by filtration, washed in the filter with water, and then dried by azeotropic distillation with acetonitrile.

The 2NapFF was thus obtained as a white solid (6.04 g, 77 %).  $\delta$ H (400 MHz, DMSO-d<sub>6</sub>) 12.81 (1H, COOH, s), 8.43 (1H, NH, d,  $J$  = 7.84 Hz), 8.12 (1H, NH, d,  $J$  = 8.56 Hz), 7.82-7.84 (2H, Ph, m), 7.72-7.73 (1H, Ph, d,  $J$  = 8.12 Hz), 7.44-7.48 (1H, Ph, m), 7.34-7.38 (1H, m, Ph), 7.12-7.26 (12H, m, Ph), 4.61-4.67 (1H, CH, dt,  $J$  = 9.09, 4.15 Hz), 4.53 (2H, s, OCH<sub>2</sub>), 4.44-4.49 (1H, m, CH), 3.09 (1H, CH<sub>2</sub>Ph, dd,  $J$  = 14.01, 5.30 Hz), 2.99 (1H, CH<sub>2</sub>Ph, dd,  $J$  = 14.05, 4.38 Hz), 2.95 (1H, CH<sub>2</sub>Ph, dd,  $J$  = 13.98, 8.39 Hz), 2.82 (1H, CH<sub>2</sub>Ph, dd,  $J$  = 13.76, 9.57 Hz)

$\delta$ C (100 MHz, DMSO-d<sub>6</sub>) 172.76, 170.88, and 167.24 (C=O), 155.51, 137.54, 137.38, 134.05, 129.38, 129.28, 129.15, 128.77, 128.21, 128.00, 127.53, 126.82, 126.48, 126.45, 126.28, 123.88, 118.48, and 107.34 (CAr), 66.70 (OCH<sub>2</sub>), 53.53 (CaH\*), 53.26 (CbH\*), 37.45 (PhCH<sub>2</sub>CaH\*), 36.71 (PhCH<sub>2</sub>CbH\*). HRMS (ESI)  $m/z$ : [M+Na]<sup>+</sup> calcd for C<sub>30</sub>H<sub>28</sub>N<sub>2</sub>NaO<sub>5</sub> 519.1890; found 519.1907.

## 2.3 Sample Preparation

### 2.3.1 Chapter 3 Sample Preparation

Samples discussed in Chapter 3 were formed using a stock solution of 2NapFF (20 mg/mL) prepared by dissolving the solid gelator in 0.1 M NaOH. This solution was then stirred overnight until a homogeneous solution was observed at pH 10.5. At this point, solutions used for heat/cool samples were heated to 60°C for 1 hour in an oven before being allowed to cool to room temperature on the bench.

## Chapter 2

The solutions were then pH adjusted to pH 7 using 2 M HCl. An equal volume of DMEM was quickly pipetted into Eppendorfs containing 2NapFF solution (20 mg/ mL) at pH 7 and vortexed using a vortex mixer, lab dancer VWR for 5 seconds. The gels were then placed in a cell culture incubator overnight at 37°C and 5% CO<sub>2</sub>. Exact makeup of DMEM used was Gibco Dulbecco's Modified Eagle Medium (DMEM) (Thermo, cat.no. 1196602) with 20% Medium 199, 10% Fetal Bovine Serum (FBS) and 2% Antibiotics. The DMEM + glucose samples refer to Dulbecco's Modified Eagle's Medium (DMEM), with 4500 mg/L glucose and sodium pyruvate (Sigma, D5671-500ML), supplemented with 1% Non-Essential Amino Acids Solution (Gibco, cat.no. 11140050), 10% Fetal Bovine Serum (FBS) 2% of antibiotics.

### 2.3.2 Chapter 4 Sample Preparation

A stock solution of 2NapFF (20 mg/mL) was prepared by dissolving the solid gelator in 0.1 M NaOH. This solution was then stirred overnight until a homogeneous solution is observed at pH 10.5. The solutions were then pH adjusted to pH 7 using 2 M HCl. An equal volume of DMEM was quickly pipetted into Eppendorfs containing 2NapFF solution (20 mg/ mL) at pH 7 and vortexed using a vortex mixer, lab dancer VWR for 5 seconds. The gels were then placed in a cell culture incubator overnight at 37°C and 5% CO<sub>2</sub>.

Solid UPy-G and BF-UPy-PEG powders were weighed and dissolved separately, UPy-G in 80 mM NaOH and BF-UPy-PEG in PBS solution. The ratio of bifunctional to monofunctional monomer used was 1:80 (B: M=1:80). The solutions were heated at 70 °C for 1 hour and 30 minutes for the bifunctional and monofunctional respectively. Neutralisation was achieved by adding 1M HCl to the UPy-G solution. The solutions were pipetted together in the correct proportions to achieve gels at the current weight percentage – 0.25, 0.5% or 1 w/v %. The hydrogels were incubated overnight at 37 °C and 5% CO<sub>2</sub>.

Multicomponent gels were formed by preparing UPy- gels as described, at double the required concentration, before quickly adding an equal volume of 2NapFF solution. The solutions were pipetted up and down until a homogeneous solution remained and were allowed to gel overnight in the incubator at 37 °C and 5% CO<sub>2</sub>.

### 2.3.3 Chapter 5 Sample Preparation

2NapFF was synthesised as described previously. A stock solution of 2NapFF (20 mg/mL) was prepared by dissolving the solid gelator in 0.1 M NaOH.

## Chapter 2

This solution was stirred overnight until a homogeneous solution was observed at pH 10.5. The solutions were then pH adjusted to pH 7 using 2 M HCl. An equal volume of media was quickly pipetted into vials containing 2NapFF solution (20 mg/ mL) at pH 7 and vortexed using a vortex mixer, lab dancer VWR for 5 seconds. In the case of the non-printed samples, the viscous solutions were poured directly into 3D-printed plastic square-shaped moulds ( $19.5 \times 19.5 \times 5$  mm) adhered to a borosilicate glass microscope slide with Araldite®.<sup>3</sup> The printed samples were taken up by a 3 mL syringe after vortexing. The syringe nozzle was covered with parafilm and left overnight. The following morning the samples were printed into moulds.

### 2.4 Shear Rheology

Rheological characterisation has been used throughout this thesis. Initially, the samples were probed for gelation using a vial inversion test. If the material did not flow upon inversion two types of rheology experiments were carried out: strain and frequency sweeps. Both tests measure the storage ( $G'$ ) and loss modulus ( $G''$ ) of a material, which indicate how solid and liquid-like the sample is respectively. It is widely accepted that when  $G'$  is an order of magnitude larger than  $G''$ , and the  $G''/G'$  value ( $\tan\delta$ ) is less than 0.1, the material is a true gel.<sup>4,5</sup> Strain measurements are used to probe the strength of the gel, i.e. how much strain is required to break the gel. This can be defined as the strain percentage where the storage modulus is no longer linear. The crossover point ( $G'' > G'$ ) indicates the complete breakdown of the network. In contrast, frequency sweeps investigate how samples react to increasing frequency. As discussed in Chapter 3, the rheological properties may vary if the samples are prepared differently or measured using a different system or geometry.

Rheology described in Chapter 3 was carried out using an Anton Paar Physica MCR 301 rheometer. The vane (Figure 16a) and PP12.5 (Figure 16b) geometries used for rheological measurements are the ST10-4V-8.8/97.5-SN18190 and the PP12.5-SN50710 models, respectively, both from Anton Paar. Strain sweeps were carried out from 0.01 to 1000% strain.

When required, a 3D printed 24 well plate holder was attached to the rheometer flat plate to facilitate measurements of the gels formed in the wells. Similarly, a 3D printed vial holder was secured to the flat plate to hold Sterilin vials in place when the 12.5 cm parallel plate geometry was used to measure the surface.

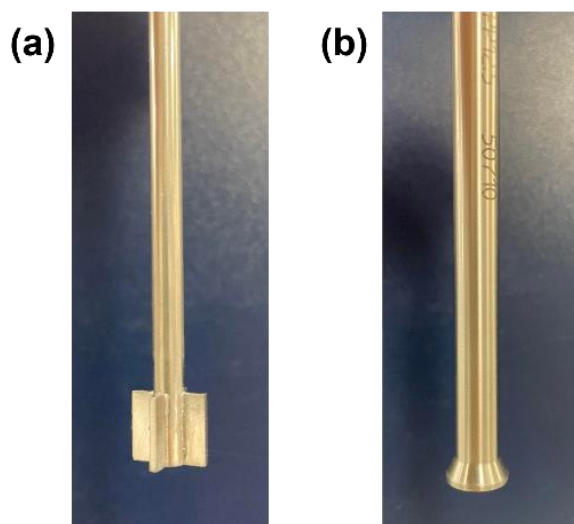


**Figure 16.** (a) vane geometry (b) 12.5 mm parallel plate geometry.

Rheological characterisation in Chapter 4 was carried out using a TA Discovery HR20 or HR 30 (TA instruments) rheometer. Hydrogels were prepared as previously described and pipetting 100  $\mu\text{L}$  of solution into each well of a 96-well plate. Following overnight incubation, the hydrogels were scooped onto the Peltier plate using a spatula. Samples were then analysed using a flat stainless-steel geometry at (diameter 8 mm) at a gap height of 950  $\mu\text{m}$ . Low viscosity silicon oil (47 V 100, RHODORSIL®) was used around the hydrogel to minimize sample drying. Strain sweeps were performed from 0.1-100% strain at an angular frequency of 1 rad/s. Frequency sweeps were carried out at 0.1% strain from 1-100 rad/s. Strain and frequency sweeps were carried out in triplicate and values averaged. Error bars represent the standard deviation between the replicates. All measurements were carried out at 37  $^{\circ}\text{C}$  using a solvent trap to minimise drying.

Rheology was carried out for Chapter 5 using an Anton Paar Physica MCR 301 rheometer. The PP12.5 geometry (PP12.5-SN50710) from Anton Paar was used in each case. Strain sweeps were carried out from 0.01 to 1000% strain. The 3D printed moulds were attached to the plate using cellotape to ensure the PP12.5 was aligned with the centre of the sample.<sup>6</sup>

## 2.5 Cavitation Rheology

All cavitation measurements were undertaken using a custom-built cavitation rheometer.<sup>7</sup> The rheometer is composed of a 10 mL Hamilton™ 1000 series Gastight syringe for air pumping mounted in a syringe pump (World Precision Instruments AL-1000).

## Chapter 2

A high precision manometer (the Cavitation Rheology Analyser Box, or CRAB) with data logging capability was custom-built to control and record the pressure. A digital manometer was connected into the system *via* Y-junction and used to calibrate and confirm pressure readings from the CRAB.<sup>7-9</sup>

### 2.6 Small-Angle Scattering

#### 2.6.1 SAXS

Measurements of samples investigated in Chapter 3 were performed on the offline Xenocs Xeuss 3.0 instrument at Diamond Light Source, funded by EPSRC under grant no EP/R042683/1. All measurements were performed by Chloe Wallace and Simona Bianco (University of Glasgow). Data processing and background subtraction was carried out by Sam Burholt (Diamond Light Source). The samples were loaded into capillaries using pre-gel solutions in 1 mL syringes equipped with a 0.8 x 120 mm 21G needle. Samples that had been prepared before arrival at Diamond in 24 well plates were loaded into a custom-made gel holder with Kapton windows allowing for high transmittance of X-rays.<sup>10</sup> The cell was then placed in the X-ray beam, allowing for SAXS measurements to be carried out. The Kapton was then corrected for during background subtraction as described below. The gel cell allowed eight samples to be loaded at a time. After each sample was measured the set up was removed, cleaned and reused for other samples. The sample-to-detector distance (0.5 m) resulted in a Q range of 0.009 to 0.6 Å<sup>-1</sup>.

Data shown in Chapter 3 Figure 14 was collected at The European Synchrotron Radiation Facility (ESRF) using the BM26 beamline, DUBBLE. All measurements were performed by Chloe Wallace and Simona Bianco (University of Glasgow). Data processing and background subtraction was carried out by Martin Rosenthal (ESRF). The samples were loaded into capillaries using solutions in 1 mL syringes equipped with a 0.8 x 120 mm 21G needle. The sample-to-detector distance (5.41 m) resulted in a Q range of 0.0036 to 0.129 Å<sup>-1</sup>. The data were reduced to 1D scattering plots and fitted to structural models in the SasView 5.0.6 software.

Samples measured in Chapter 4 were loaded into 1.5 mm borosilicate glass capillaries (Capillary Tube Supplies Ltd) and sealed using UV curable adhesive (Norland). SAXS data were collected on a Ganesha 300XL instrument (Xenocs) fitted with a Cu K $\alpha$  source.

## Chapter 2

SAXS data were collected at room temperature over a  $Q$  range of  $0.007 - 0.25 \text{ \AA}^{-1}$  for an exposure time of 3600 seconds. All measurements were corrected for transmission and absolute intensity and had the solvent background and empty capillary scattering subtracted before processing. Data were reduced using SAXSGUI, and model fits were performed using SASView 4.0).<sup>39</sup> To calculate the X-ray scattering length densities (SLDs) for all samples, the NIST neutron activation and scattering calculator was used<sup>40</sup> assuming a density of  $1.58 \text{ g/cm}^3$  for the LMWG.

SAXS measurements for Chapter 5 were performed at the Diamond Light Source, Didcot, at the I22 beamline under experiment number SM33006-1. The beamline operated at an energy of 12.4 keV and the detector distance was set to 8.750 m, allowing a final  $Q$  range of  $0.0017$  to  $0.203 \text{ \AA}^{-1}$ . Samples were prepared in glass vials and loaded into borosilicate glass capillaries (1.56 mm internal diameter) using a 1 mL syringe equipped with a 21G needle immediately. Printed samples were allowed to form in the syringes overnight and “printed” into the capillaries via a 21G needle. For each sample, 1000 x 10 ms frames were collected and averaged to achieve a total exposure of 10 s. The raw data was processed using the Dawn Science software (version 2.27),<sup>11</sup> according to a standard I22 pipeline by A. Sutherland (Diamond Light Source).<sup>12</sup> As part of the processing, the backgrounds were subtracted from the raw 2D SAXS data and a full azimuthal integration was performed to reduce the data to a  $I$  vs  $q$  plot. The plots were then fitted to structural models in the SasView software (5.0.6). To calculate the X-ray scattering length densities (SLDs) for all samples, the NIST neutron activation and scattering calculator was used (<https://www.ncnr.nist.gov/resources/activation/>), assuming a density of  $1.55 \text{ g/cm}^3$  for the low molecular weight gelators.

### 2.6.2 SANS

Samples were prepared as previously described in cuvettes using  $\text{D}_2\text{O}$  and NaOD (0.1 M) to replace  $\text{H}_2\text{O}$  and NaOH. Deuterated culture media used for the 2NapFF media gels was obtained by freeze drying a known volume of DMEM and resuspending in  $\text{D}_2\text{O}$ . SANS experiments were performed using the SANS2d instrument at the ISIS Neutron and Muon source of the STFC Rutherford Appleton Laboratory (Didcot, UK), experiment number 2310032. The samples were measured using a sample changer maintained at  $25 \text{ }^\circ\text{C}$  by water bath.

## Chapter 2

The source to sample/sample to detector distance was set to  $L1 = L2 = 8$  m to access a  $q$  range of 0.0024 to 0.38  $\text{\AA}^{-1}$ , where  $q = 4\pi\sin(\theta/2)/\lambda$ . All samples were measured in UV spectrophotometer grade quartz cuvettes (Hellma) with 2 mm path length. The 2D scattering patterns were azimuthally integrated to obtain 1D plots of intensity vs  $Q$  using Mantid software.<sup>13</sup> The scattering from the  $D_2O$  background and the empty cell were subtracted from the gelator solutions using Mantid and SANS curves were fitted using SasView (5.0.5). To calculate the scattering length densities (SLDs) for all samples, the NIST neutron activation and scattering calculator was used<sup>14</sup> assuming a density of 1.58  $\text{g/cm}^3$  for the LMWG.

### 2.6.3 Fitting Small-Angle Scattering Data with SASView

For all experiments, a direct beam and empty cell scattering were collected as well as a solvent (which in this work was water) and any artefact scattering (eg Kapton from the gel cell). This data was then removed from the sample scattering pattern via a process called background subtraction, carried out using DAWN (Data Analysis Software group, Diamond Light Source Ltd).<sup>15</sup> This produces a scattering pattern specifically for the sample and does not include any artefact scattering from the cell used (for example, Kapton from the gel cell) or the background. The 2D detector scattering pattern was then converted to an “average” 1D scattering curve representing scattering intensity as a function of wave-vector ( $q$ ) via equation 1, where  $\lambda$  is the wavelength of the incident beam and  $\theta$  is half the angle of incidence.

$$q = \frac{4\pi\sin\theta}{\lambda} \quad \text{(Equation 1)}$$

This 1D scattering pattern can be compared to form factors which have previously been defined using mathematical modelling, including cylinders and spheres. This provided information on the structures present in a sample, such as length, radii and polydispersity

Throughout this thesis we have used SasView (5.0.5) to process and fit the 1D scattering pattern of samples. This was carried out by loading the background subtracted data onto the software view the data explorer panel. The data was then plotted by selecting the data in the data explorer window and clicking create new. This allows the data to be checked for errors in background subtractions and allows us to gain an idea of what model would be suitable to fit the data to. Next the data is sent to the fit panel by clicking the “send data to” button and selecting “fitting” from the dropdown.

## Chapter 2

Once the data is ready to be fit a model can be selected depending on the shape of the data. The majority of data collected in this thesis fit best to some variation of cylinder model. Therefore, the data was initially fit to a cylinder model, then an elliptical/hollow cylinder model etc. Once the chosen model was loaded in the model tab, the individual parameters were selected and the data was fit to each. The calculated scattering length densities (SLDs) are also added at this stage. These values are measures of the “scattering power” of a material. SLDs for the solvent and the material being measured need to be considered when fitting scattering data and are calculated as described above for each chapter. These values remained fixed throughout the fitting process.

Polydispersity was enabled to fit systems that do not contain monodisperse structures for certain fits. For the fits discussed in this work, polydispersity of 0.1 was often applied to the radii, suggesting structures with different sized radii are present.

The model which the data fit closest to with the most reasonable parameters and error was then selected and exported. However, when fitting any scattering data is essential also to consider the uniqueness of the fits. This means that while one fit is given to a scattering pattern, a number of other potential solutions may also be appropriate. For this reason, we have attempted to use other techniques such as microscopy to support any scattering data collected.

### 2.7 Cryo-TEM

Vitrified thin films for CryoTEM analysis were prepared using an automated vitrification robot (FEI Vitrobot Mark IV) by plunge vitrification in liquid ethane. Before vitrification, a 200-mesh copper grid covered with a Lacey carbon film (Electron Microscopy Sciences) was surface plasma treated for 40 seconds using a Cressington 208 carbon coater. CryoTEM imaging was carried out on the Glacios (Thermo Fisher), equipped with a field emission gun (X-FEG), Ceta 16M camera and a Falcon 4i direct electron detector. The microscope was operated at 200 kV acceleration voltage in bright-field TEM at a nominal magnification of 6.500× and a dose rate of 2 e<sup>-</sup>/Å<sup>2</sup>·s; or at 24.000× magnification and a dose rate of 4 e<sup>-</sup>/Å<sup>2</sup>·s; both with a 1s image acquisition time.

## Chapter 2

### 2.8 Circular Dichroism

CD is the difference in absorption of left and right circularly polarized light. It is particularly useful for identifying the appearance of chiral structures in proteins. In Chapter 4 we use CD to examine the effect of a crosslinker on the packing of a supramolecular multicomponent system.

Samples were prepared as previously described and pipetted into a quartz cell with a 0.01 mm path length and left overnight to allow gelation to occur. The following morning CD was measured using a Chirascan VX CD spectrometer (Applied Photophysics Limited, U.K.) with the following parameters: scanning mode, continuous; scanning speed, 120 nm/min and bandwidth, 1 nm. All CD data are presented as ellipticity and recorded in millidegree (mdeg). Absorbance and high tension (HT) spectra were recorded concomitantly with CD spectra. An empty cuvette was measured as a background and subtracted from all other measurements. The spectra were recorded in triplicate and averaged.

### 2.9 3D Printing

A modified RepRap Ormerod 2 (version 528.4) 3D printer was used to extrude 3D printed hydrogels.<sup>16</sup> Printed samples were formed by first making gels (2 mL) within polypropylene syringes equipped with 23G needles cut to 3 mm. The syringes were then loaded into a custom gel 3D printer and used to print layers of pre-formed gel in a serpentine pattern at an extrusion rate of 4  $\mu\text{L mm}^{-1}$  and a shear rate ( $\gamma$ ) of 9408  $\text{s}^{-1}$  as previously described.<sup>16</sup>

### 2.10 Cell Culture

All cell lines were thawed prior to use by removing frozen vials from the liquid nitrogen storage tank and immediately placed on dry ice. Next, the vials were placed in a water bath at 37 °C and allowed to thaw. When the cell preservative media had almost totally defrosted, the thawed cells were added to a 15-mL sterile conical tube containing 10 mL of appropriate pre-warmed medium for each cell line (see below). The cells were then centrifuged at 300  $\times$  g for 10 min at room temperature before the media was carefully aspirated without disturbing the cell pellet. The cells were then resuspended in 5 mL of the relevant culture media, gently pipetting up and down to break down the pellet before they were counted and seeded into a T75 flask. The cells were passaged a couple of times before an experiment was carried out to ensure they were healthy.

## Chapter 2

The mesenchymal stem cells (MSCs) used in Chapter 3 were obtained from Promocell. MG-63. The cells were cultured in Dulbecco's modified essential medium (DMEM) (Sigma) supplemented with 5% Foetal Bovine Serum (FBS; Sigma), 1% (v/v) L-glutamine (200 mM, Gibco) and 2% antibiotics (6.74 U/mL penicillinstreptomycin, 0.2 µg/mL fungizone) (Sigma). The cells were cultured in a T75 flask, to approximately 70% confluence, media was changed every 3-4 days, and cells were split 1-2 times a week, depending on confluence. For the 2D celculture studies the MSCs were grown in a T75 flask, washed with PBS, trypsinised, counted with a haemocytometer, and resuspended in appropriate amount of DMEM. The cells were then seeded on top of 1 mL of hydrogel at a density of  $1 \times 10^4$  MSCs per well in 24-well plates and stained at a defined timepoint.

The human normal dermal fibroblasts (hNDFs) used in Chapter 4 were cultured in DMEM Advanced medium (Gibco) supplemented with 10% fetal bovine serum (FBS), 1% penicillin-streptomycin (P/S), and 1% Gluta MAX at 37 °C and 5% CO<sub>2</sub>. 2D cell culture of hNDFS on the hydrogel samples was carried out by preparing the gels in 15-well Ibidi slides (10 µL per well). After overnight incubation the hydrogels were UV-sterilised for 15 minutes, before 30 µL of media was added to the top of each sample and incubated for 1 hour at 37 °C and 5% CO<sub>2</sub>. After this, hNDF cells were seeded at a density of 5000 cells per well.

Macrophage cells used in Chapter 5 were obtained by differentiating THP-1 cells. This was carried out by resuspending the cells in RPMI media with 100 ng/mL phorbol 12-myristate 13-acetate (PMA). Cells were seeded in 24 well plates at a density of seed 200,000 cells/mL in 24-well plates and incubated for 48 hours. Once cells were fully differentiated, dissociation was carried out by removing media and adding 5mM EDTA solution and leaving for 10 minutes at 4°C. The supernatant was collected and washed twice with PBS collecting the PBS each time. This process was repeated twice more before a cell scraper was used to lift as many cells as possible. The collected supernatant was collected and centrifuged at 500g for 5 minutes. The supernatant was then discarded and the cell pellet was resuspended in RPMI media with 100 ng/mL PMA.

## Chapter 2

### 2.10.1 Immunofluorescence

The same immunofluorescence protocol was used to stain the hNDF cells in Chapter 4 and the macrophages in Chapter 5. After overnight incubation media was removed and the samples were washed three times with PBS. The cells were then fixed 3.7% for 10 minutes whereafter 0.5% Triton X-100 in PBS was added for another 10 minutes to permeabilize the cells. Cells were washed twice with PBS and blocked with 10% goat serum in 0.05% Triton X-100 in PBS for 30 minutes. Next, the cells were incubated with the primary antibodies anti-Lamin A (1:200; Abcam ab26300) and vimentin (1:300; Abcam ab20346) diluted in 2% goat serum in 0.05% Triton X-100 in PBS overnight at 4 °C. Thereafter, the cells were washed three times with PBS and incubated with the secondary antibodies anti-rabbit Alexa 647 (for Lamin A) and anti-mouse Alexa 555 (for vimentin) (both 1:250) at room temperature for 2 hours, the cells were then washed three times with PBS and imaged. Imaging was performed using a Leica TCS SP8 X confocal microscope (Leica Microsystems). Images were processed in ImageJ to create max-projection images of the original z-stacks.

### 2.10.2 Live/Dead Assay

hTERT cells were plated onto the prepared hydrogels at a density of 10,000 cells/mL in 1 mL of culture medium. The plate was incubated at 37°C and 5% CO<sub>2</sub> and removed after 3 and 7 days. The Live/dead stain was prepared by adding 2 µmol/L acetomethoxy derivate of calcein (calcein-AM) and 2 µmol/L ethidium homodimer-1 per mL of media. The stain was then added on top of each hydrogel and left in the incubator for 30 minutes. The dye was then removed, and the samples were washed with PBS three times. The examination was carried out as described below.

## 2.11 Confocal Microscopy

Confocal images shown in Chapter 3 (Figure 12) were collected using an A Zeiss LSM710 confocal microscope (Zeiss, Gottingen, Germany) and software Carl Zeiss ZEN 2011 v7.0.3.286 with an LD EC Epiplan NEUFLUAR 50X, 0.55 DIC (Carl Zeiss, White Plains, NY, USA) objective was used. All samples were prepared in a CELLview™ (Greiner Bio-One, Stonehouse, UK) 35 mm plastic cell culture dish with a borosilicate glass bottom. The samples were stained with 0.1 wt% Nile blue A solution, and excited at 634 nm using a He-Ne laser (Zeiss, Gottingen, Germany). Images shown in Chapter 3 (Figure 15) and Chapter 5 were obtained by transferring samples from 24-well plates to glass coverslips using a

## **Chapter 2**

spatula, with side cells were seeded on facing downwards. Imaging was then carried out using a Zeiss confocal LSM 980 microscope using 10x or 20x objective.

Images shown in Chapter 4 were collected using a Leica TCS SP8 X confocal microscope (Leica Microsystems). Images were processed in ImageJ to create max-projection images of the original z-stacks. Imaging in Chapter 5 was performed using a ZEISS LSM 980 confocal microscope. Images were processed in ImageJ to create max-projection images of the original z-stacks.

### **2.12. Bioprinting**

All solutions and equipment were sterilised using UV for 30 minutes before use. Samples were prepared as previously described with RPMI media with 100 ng/mL PMA, containing macrophage cells so the resulting cell density was 200,000 per mL of hydrogel. After vortexing, the pre-gel solution was transferred into a 3 mL syringe cartridge (Cellink: CSC010300102) and incubated for 20 minutes to allow for gel formation. After this time, the syringe was equipped with a 25 G, 24 mm needle (Cellink NZ6250255001) and printed into a 6-well plate using a Cellink Bio X6 printer at the speeds and pressure listed in Chapter 5 Table 4. Post-printing, 1 mL of RPMI media with 100 ng/mL PMA was added to each well and samples were incubated overnight.

## Chapter 2

### 2.12 References

1. E. R. Draper, B. Dietrich, K. McAulay, C. Brasnett, H. Abdizadeh, I. Patmanidis, S. J. Marrink, H. Su, H. Cui, R. Schweins, A. Seddon and D. J. Adams, *Matter*, 2020, **2**, 764-778.
2. L. Chen, K. Morris, A. Laybourn, D. Elias, M. R. Hicks, A. Rodger, L. Serpell and D. J. Adams, *Langmuir*, 2010, **26**, 5232-5242.
3. A. M. Fuentes-Caparrós, Z. Canales-Galarza, M. Barrow, B. Dietrich, J. Läger, M. Nemeth, E. R. Draper and D. J. Adams, *Biomacromolecules*, 2021, **22**, 1625-1638.
4. P. Terech and R. G. Weiss, *Chem. Rev.*, 1997, **97**, 3133-3160.
5. R. G. Weiss, *J. Am. Chem. Soc.*, 2014, **136**, 7519-7530.
6. M. J. S. Hill, A. M. Fuentes-Caparrós and D. J. Adams, *Biomacromolecules*, 2023, **24**, 4253-4262.
7. A. M. Fuentes-Caparrós, B. Dietrich, L. Thomson, C. Chauveau and D. J. Adams, *Soft Matter*, 2019, **15**, 6340-6347.
8. J. A. Zimmerlin, N. Sanabria-DeLong, G. N. Tew and A. J. Crosby, *Soft Matter*, 2007, **3**, 763-767.
9. Y. Ji, A. M. Dagro, G. Dorgant, D. Starr and J. W. Wilkerson, *Exp. Mech.*, 2022, 799-812.
10. C. J. C. Edwards-Gayle, N. Khunti; I. W. Hamley; K. Inoue, N. Cowieson and R. Rambo, *J. Synchrotron Radiat.*, 2021, **28**, 318-321
11. J. Filik, A. W. Ashton, P. C. Y. Chang, P. A. Chater, S. J. Day, M. Drakopoulos, M. W. Gerring, M. L. Hart, O. V. Magdysyuk, S. Michalik, A. Smith, C. C. Tang, N. J. Terrill, M. T. Wharmby and H. Wilhelm, *J. Appl. Crystallogr.*, 2017, **50**, 959-966.
12. B. R. Pauw, A. J. Smith, T. Snow, N. J. Terrill and A. F. Thünemann, *J. Appl. Crystallogr.*, 2017, **50**, 1800-1801
13. O. Arnold, J. C. Bilheux, J. M. Borreguero, A. Buts, S. I. Campbell, L. Chapon, M. Doucet, N. Draper, R. Ferraz Leal, M. A. Gigg, V. E. Lynch, A. Markvardsen, D. J. Mikkelsen, R. L. Mikkelsen, R. Miller, K. Palmén, P. Parker, G. Passos, T. G. Perring, P.

## Chapter 2

F. Peterson, S. Ren, M. A. Reuter, A. T. Savici, J. W. Taylor, R. J. Taylor, R. Tolchenov, W. Zhou and J. Zikovsky, *Nucl. Instrum. Methods Phys. Res. A*, 2014, **764**, 156-166

14. <https://www.ncnr.nist.gov/resources/activation/>.

15. M. Basham, J. Filik, M. Wharmby, P.Chang, B. El Kassaby, M. Gerring, J. Aishima, K. E. Levik, B. Pulford, I. Sikharulidze, D. Sneddon, Webber, M.; Dhesi, S.; Maccherozzi, F.; Svensson, O.; Brockhauser, S.; N aray, G.; Ashton, A., *J. Synchrotron Radiat.*, 2015, **22**

16. M. C. Nolan, A. M. Fuentes Caparr os, B. Dietrich, M. Barrow, E. R. Cross, M. Bleuel, S. M. King and D. J. Adams, *Soft Matter*, 2017, **13**, 8426-8432.

## **Chapter 3: Using Cell Culture Media to Gel 2NapFF**

C.Wallace was responsible for synthesis of 2NapFF, collection of rheological data and carrying out cell work. Preparation of small-angle x-ray scattering (SAXS) samples and collection of SAXS data was carried out by C. Wallace and S. Bianco, R. Ginesi and E. Bowley (University of Glasgow). Processing of SAXS data shown in Figure 14 was carried out by M. Rosenthahal (ESRF). All other SAXS data was processed by S. Burholt (Diamond Light Source) and fitted by C. Wallace. D. Adams conceptualised and supervised the project.

### 3.1 Introduction

Low molecular weight gelators (LMWG) are of great interest in various biomedical fields such as tissue engineering, drug delivery and regenerative medicine. This is largely due to the plethora of advantages associated with these materials including their high-water content, and ability to encapsulate bioactive factors, making them ideal candidates for supporting cell growth and tissue regeneration.<sup>1,2</sup> Additionally, these materials can be functionalised using bioactive motifs to mimic the complexity of the native extracellular matrix.<sup>3</sup> As previously discussed, *N*-protected LMWGs are a widely explored class of peptide-based gelators for biological applications. Our group has thoroughly investigated the *N*-protected dipeptide gelator, 2NapFF (Figure 1). It has previously been reported that this gelator forms worm-like micelles at high pH, which can form different networks depending on the gelation method employed.<sup>4</sup> For example, adding acid or glucono- $\delta$ -lactone (GdL) to these solutions leads to the re-protonation of the carboxyl group, causing the pH to drop and the formation of an entangled fibrous network. In contrast, the addition of a divalent metal salt such as calcium chloride to the solution at high pH results in a metal co-ordinated crosslinked network as two deprotonated hydroxyl group coordinate to a divalent metal cation. (Figure 1).<sup>5</sup> This method is employed in this chapter, as we intend to use our materials for biomedical applications, thus it is essential to maintain a physiological pH.

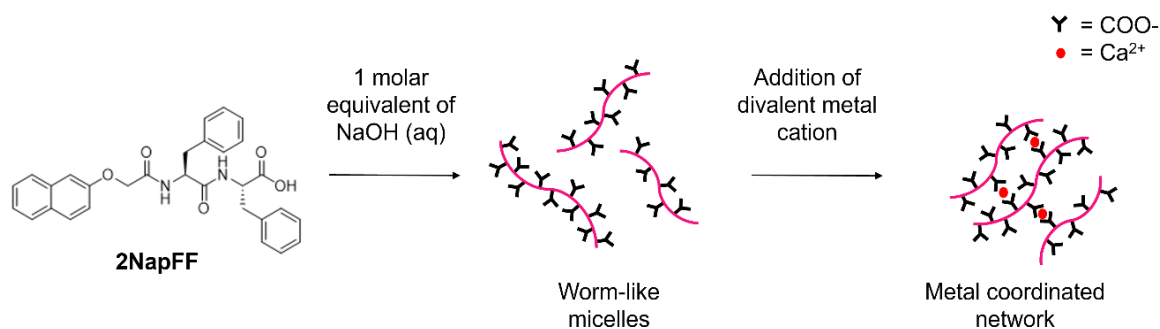


**Figure 1.** Schematic depicting how a solution of 2NapFF forms worm-like micelles at high pH. These micelles then crosslink to form a metal coordinated structure upon addition of a divalent cation to form a metal co-ordinated network. Figure adapted from *Chem*, 2017, **3**, 390-410.<sup>4</sup>

### Chapter 3

It is sometimes possible to control properties of these systems by modifying the pre-gel structures present in the gelator solution.<sup>6,7</sup> This was highlighted in the work of Zhou et al., which revealed that controlling the initial temperature at the liquid-liquid phase separation stage, influences the formation of phase-separated droplets.<sup>8</sup> Adjusting these conditions allowed for control over the self-assembly pathways of these droplets into pre-fibrils, ultimately shaping the morphology of the hydrogel network. These findings allow for fine-tuning of the mechanical strength and recovery performance of the hydrogels.<sup>8</sup> Likewise, it had been found that heating and cooling a solution of 2NapFF at high pH, significantly increases the viscosity of the solution, compared to the unheated solution.<sup>9</sup> Small-angle x-ray scattering measurements revealed that the heat-cool cycle caused the hollow cylinders present in the solution, to increase in length due to the dehydration of the core. Furthermore, when these heat-cooled solutions were gelled using CaCl<sub>2</sub>, the resulting gels were significantly stiffer than those which had not been heated. This phenomenon can be beneficial as the same gelator can be used to create materials with varying properties.

When developing potential biomaterials, growth factors can be added to encourage certain behaviour from the cells present. However, adding these proteins directly to the cell media can lead to a “burst release”, when a large proportion of the bioactive species are released at once.<sup>10</sup> Previous research has shown that burst release kinetics of growth factors can lead to major side effects and hinder the desired therapeutic outcomes.<sup>11</sup> Moreover, burst release can lead to a rapid depletion of the growth factors, resulting in suboptimal tissue regeneration and healing.<sup>12</sup> Therefore, when developing potential biomaterials controlled release profiles are crucial for achieving the desired biological effects without overwhelming the surrounding microenvironment. Polyhedrin Delivery Systems (PODS®) from Cell Guidance Systems, provide a sustained release of growth factors to overcome this issue. These PODS® contain a cargo protein, encased within a microcrystal formed by the self-assembly of a polyhedron protein.<sup>14,15</sup> The encapsulated cargo remains protected within the microcrystal creating a stable system over an extended period. Degradation of the PODS® occurs via cell-mediated, protein-dependant mechanisms, allowing for sustained release of the bioactive cargo.<sup>16</sup> This process permits prolonged delivery to the target site, avoiding any toxicity due to burst release kinetics.<sup>17-19</sup>

## Chapter 3

In this chapter, culture media was used as a source of ions to trigger the gelation of 2NapFF at physiological pH. These systems are then employed to investigate the effects of heating and cooling a pre-gel solution of 2NapFF before triggering gelation. We then compare the hydrogels formed from the heat-cooled solutions to those formed with the native solution across a range of length scales. Finally, we utilise the PODS® technology from Cell Guidance Systems, to functionalise these materials, creating promising systems for future cell culture applications.

### 3.2 Results and Discussion

To test if culture media could be used to crosslink 2NapFF, 1 mL aliquots of 2NapFF 20mg/mL solutions were prepared and pH adjusted to pH 7 as described in section 2.4.2. (Figure 2a). Specific volumes of Gibco Dulbecco's Modified Eagle Medium (DMEM) (1-3 mL) were then quickly pipetted into the vials and vortexed for 5 seconds. The samples were left undisturbed overnight to allow diffusion ions from the DMEM and the gel to form. The sample prepared using 1 mL DMEM (10 mg/mL) formed self-supporting structures that did not move when the vials were inverted (Figure 2b). On the other hand, the solutions prepared using 2 mL and 3 mL DMEM (at concentrations of 6.7 mg/mL and 5 mg/mL 2NapFF respectively) started to flow down the vial when inverted (Figure 2c). Oscillatory rheology confirmed that a reproducible self-supported structure was produced by the 10 mg/mL samples. This was then repeated using different media Sigma Dulbecco's Modified Eagle Medium (DMEM) with high glucose (DMEM + glucose), to determine if the type of media used affects the resulting mechanical properties of the hydrogel formed. It was found that these samples had a significantly lower storage modulus than those composed of Gibco's DMEM. We hypothesise that this variation may be due to differences in ion concentrations between brands or the presence of glucose impacting the self-assembly (Figure 2d and e).

## Chapter 3

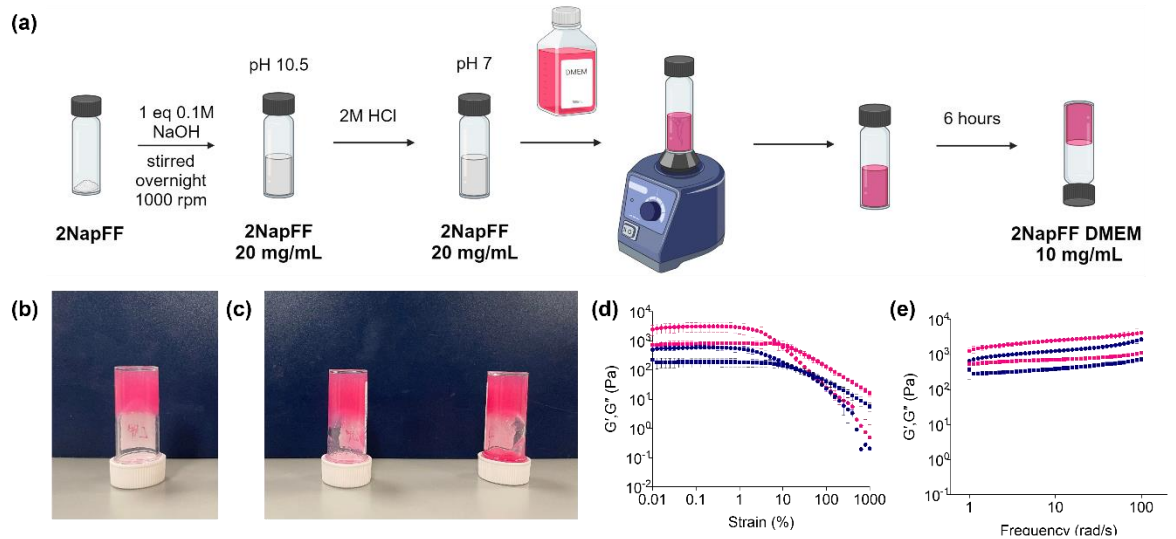


**Figure 2.** (a) Schematic showing the preparation of 2NapFF/DMEM hydrogel samples. (b) 2NapFF/DMEM hydrogels at concentrations of 10 mg/mL (c) 6.7 mg/mL and 5mg/mL respectively (d) Strain sweep data of 10 mg/mL DMEM (pink) and high glucose DMEM (navy) samples (e) Frequency sweeps of 10 mg/mL DMEM (pink) and high glucose DMEM (navy) samples. Error bars are representative of the standard deviation between triplicates.

### 3.2.1 The effect of heating and cooling 2NapFF as a solution

As previously discussed, it has been established that exposing a solution of 2NapFF at high pH to heat-cool cycle before applying a gelation trigger directly affects the properties of the network formed.<sup>9</sup> With this in mind, a solution of 2NapFF at pH 10.5 was heated for an hour at 60 °C, and allowed to cool back to room temperature before neutralisation with 2M HCl and culture media being added, triggering gelation. This temperature was chosen as at higher temperatures the solutions became highly viscous and difficult to stir, leading to inhomogeneous gels. We were then able to compare the bulk properties of these gels with those which had not been heated as solutions using oscillatory rheology. Interestingly, we found that the 2NapFF/DMEM hydrogels whose gelation was triggered after the solution had been through a heat-cool cycle, exhibit a lower  $G'$  (750 Pa) than those which had not (2500 Pa) (Figure 3a and 3c). Additionally, it was noted that the samples that had undergone the heat-cool cycle displayed a longer linear viscoelastic region than those that had not. This implies that while the heat-cooled samples are less stiff than the original hydrogels, they have stronger mechanical properties. This result is particularly interesting as it has been shown that the mechanical properties of biomaterials can have a direct effect on cell behaviour.<sup>20</sup> It also allows us to access materials with different biomechanical properties without changing the chemical composition.

### Chapter 3

In contrast, when investigating the effect of heating and cooling the gelator solution before triggering with high glucose DMEM, we observed a very slight increase in storage modulus and viscoelastic region when the samples were heated and cooled. This further emphasises the influence the cell culture media has over the rheological properties of these hydrogels.

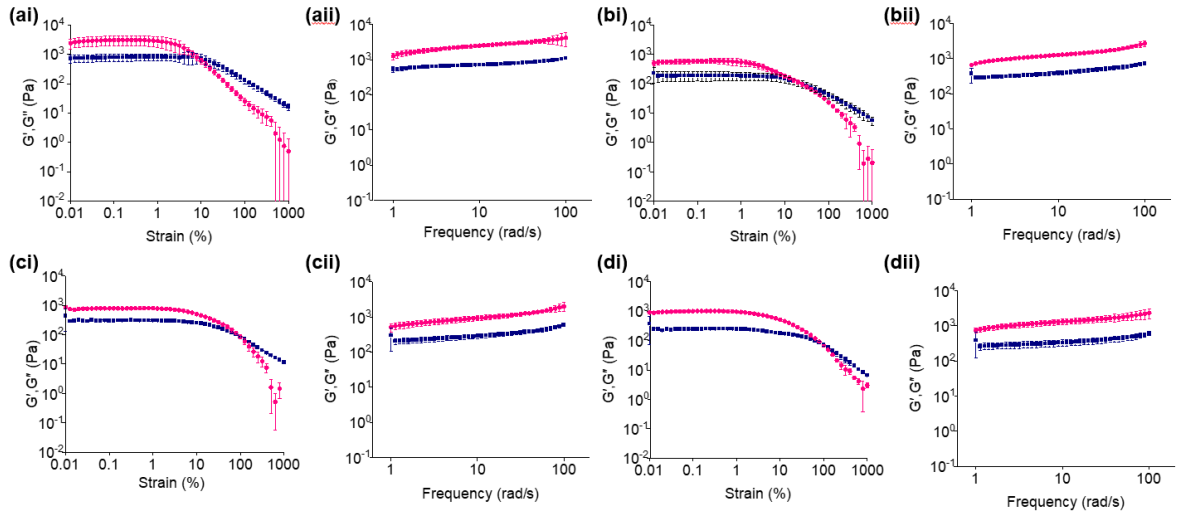


**Figure 3. (ai-ii)** Strain and frequency sweeps of 2NapFF/DMEM gels. **(bi-ii)** Strain and frequency sweep of 2NapFF/DMEM + glucose gels. **(ci-ii)** Strain and frequency sweep of heat/cool 2NapFF/DMEM gels formed from 2NapFF solutions which had been heated for 1 hour at 60°C and allowed to cool before gelation was triggered. **(di-ii)** Strain sweep and frequency sweeps of 2NapFF/DMEM + glucose gels formed from 2NapFF solutions which had been heated for 1 hour at 60°C and allowed to cool before gelation was triggered. All samples were prepared in Sterilin vials and measured using the vane geometry. In each case, the pink data represent  $G'$  and the navy data represents  $G''$ . Error bars are representative of the standard deviation between the three samples measured.

To further investigate the differences between the systems, we decided to carry out viscosity measurements on both media. While culture media is often considered a Newtonian fluid due to its aqueous nature, it may display non-Newtonian, shear thinning behaviour when supplements are added.<sup>21</sup> Both types of media used were supplemented with additives including foetal bovine serum (FBS) (see Section 2.4.2 for exact formulation) which led to the non-Newtonian properties observed (Figure 4a). Notably, the DMEM media with glucose displays a slightly higher viscosity than the DMEM without glucose at lower shear rates. This suggests that even the addition of glucose as a solute affects the viscosity of the media.

### Chapter 3

Next, we examined how aging affected each of the hydrogels. This is especially important for cell culture applications, as variations in stiffness over time can impact cell differentiation.<sup>22</sup> We did this by carrying out strain sweeps on the gels 48 hours after gelation and comparing to the original data obtained after 24 hours (Figure 4b-e). Regarding the 2NapFF/DMEM hydrogels, we discovered that the stiffness of the hydrogels falls from 2600 Pa to 700 Pa between 24 and 48 hours (Figure 4b). Conversely, the 2NapFF/DMEM hydrogels samples which had undergone a heat-cool cycle before gelation increased in stiffness from 800 Pa to 2900 Pa (Figure 4c). The change in  $G'$  illustrated by the 2NapFF/DMEM hydrogels may be desirable for ECM mimics, as the dynamic nature of the ECM means it is constantly changing stiffness.<sup>23</sup> It has previously been found that changes in the mechanical properties, including the stiffness of a substrate, plays a crucial role in cellular mechanotransduction and epigenetic regulation during fibroblast activation.<sup>24, 25, 26</sup> Such properties highlight the potential of the 2NapFF/DMEM systems for tissue engineering applications. In contrast, the samples gelled using DMEM with glucose, displayed very little difference in rheological properties, with the heat-cool samples producing almost identical data (Figure 4 d and e). While the dynamic changes in stiffness observed in the 2NapFF/DMEM gels are appealing for tissue engineering applications as discussed, we decided to focus on the 2NapFF/DMEM with glucose hydrogels for this work. We came to this decision as the consistency in  $G'$  allows us to investigate how various parameters affect the rheological properties of these systems without having to account for any aging effects.

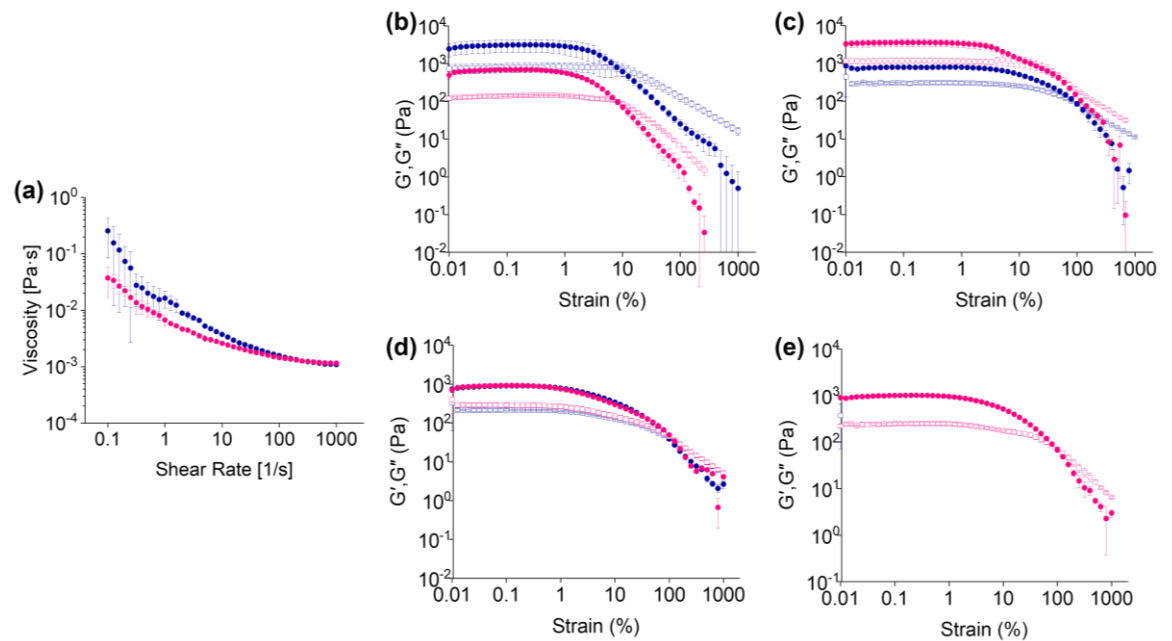


**Figure 4.** (a) Viscosity plot of DMEM (pink) and DMEM with high glucose (navy). (b) Strain sweep data for 2NapFF/DMEM gels measured 24 (navy) and 48 hours (pink) after gelation. (c) Strain sweep data for 2NapFF/DMEM formed from a solution that had been heated and cooled measured 24 (navy) and 48 hours (pink) after gelation. (d) Strain sweep data for 2NapFF/DMEM + glucose gels measured 24 (navy) and 48 hours (pink) after gelation. (e) Strain sweep data for 2NapFF/DMEM + glucose gels formed from a solution that had been heated and cooled measured 24 (navy) and 48 hours (pink) after gelation. Navy data not visible as almost identical to pink data. In each case the filled data points represent  $G'$  and the hollow are  $G''$ . Error bars are representative of the standard deviation between triplicates performed using three separate samples.

Another important factor to consider when developing a biocompatible system is the effect of temperature. So far, all gels have been formed by leaving on the bench top overnight at room temperature. However, if we intend to mimic conditions *in vivo* it is necessary to look at the properties of the gels at physiological temperature (37 °C). This is particularly important if these gels are to be considered for 3D culture applications, as they will need to form inside a cell culture incubator. To explore this, the gels were prepared as previously described, before allowing them to form in a water bath at 37 °C overnight (Figure 5a). The following morning rheology measurements were carried out using the cup and vane set up.

### Chapter 3

Our results revealed that for both hydrogels (regardless of whether they had been heat-cooled before gelation or not) displayed stiffer mechanical properties when formed at 37 °C compared to room temperature. The hydrogels which did not undergo a heat/cool cycle as a solution increased from a  $G'$  of 700 Pa to 2000 Pa (Figure 5b), while the heat-cool samples increased from 1000 Pa to 3400 Pa (Figure 5c). These results are particularly promising as the ability of the gels to assemble at physiological temperature highlights their potential as biomaterials. This observation also reiterates the impact changes in environmental conditions can have on these gelators.

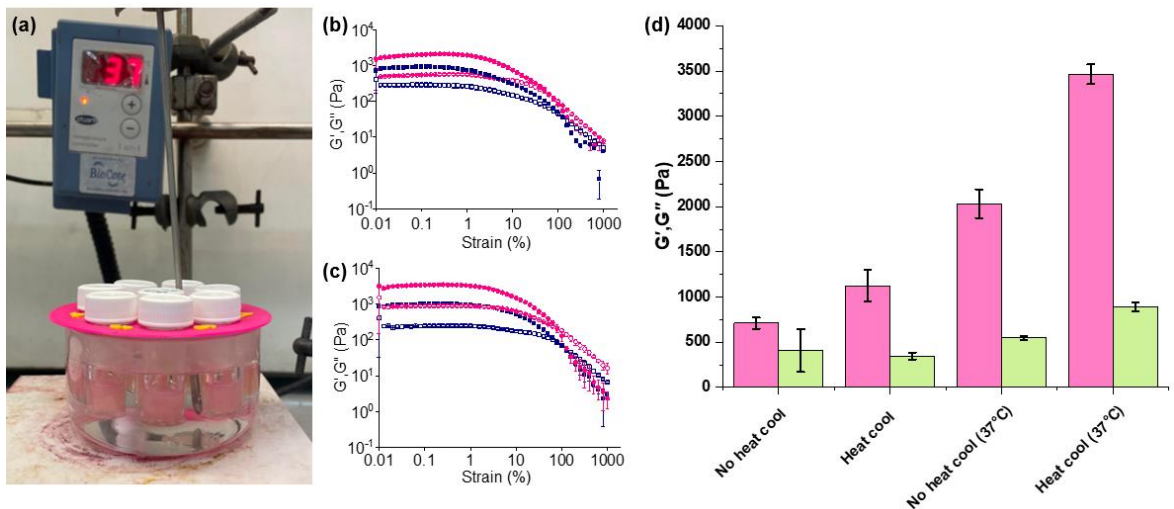


**Figure 5.** (a) Water bath set up used to maintain samples at 37 °C. (b) Strain sweep data for 2NapFF/DMEM + glucose hydrogels formed at 25 °C (navy) and 37 °C (pink). (c) Strain sweep data for 2NapFF/DMEM +glucose gels formed from a solution that had been heated and cooled formed at 25 °C (navy) and 37 °C (pink) (d) Bar chart showing the  $G'$  (pink) and  $G''$  (green) of the samples formed at 25 °C (navy) and 37 °C (pink) where the error bars are representative of the standard deviation between triplicates carried out using three different samples.

The rheological experiments discussed previously have been performed using a vane geometry.<sup>26</sup> An advantage of this set up is that the vane can penetrate a sample without destroying the overall structure. Thus, allowing us to measure the bulk properties of the sample (Figure 6a). However, as we are interested in using these samples as potential biomaterials for 2D cell culture, we deemed it important to also investigate the surface properties of the hydrogels. To do so we employed a parallel plate geometry, which measures the bulk flow of material from the top surface of the sample (Figure 6b).

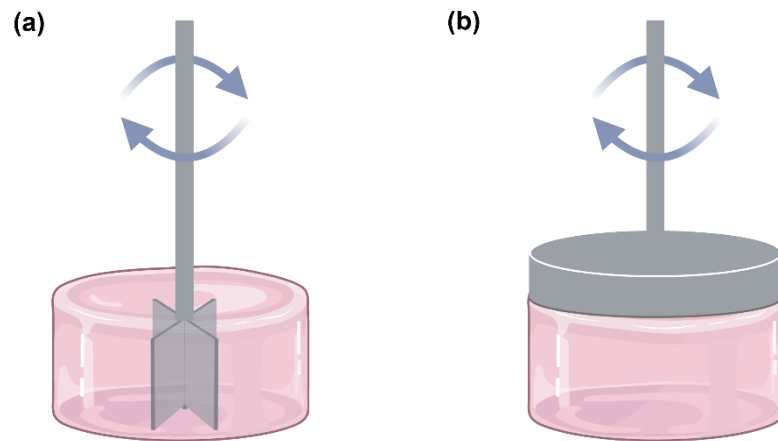


**Figure 6.** (a) Diagram depicting how the vane geometry measures the bulk flow of the material from within the hydrogel sample without breaking the structure. Contrastingly, (b) shows how the parallel plate geometry measures the bulk flow of the material from the surface.

By utilising the parallel plate geometry, we hoped to gain insight to the forces the cells are exposed to when cultured in on top of the samples. We also decided to use the parallel plate to measure the rheological properties of the 2NapFF/DMEM +glucose hydrogels formed in 24 well plates, which would be later used for cell culture. These experiments were carried out using a custom 3D printed 24 well plate holder which attaches to the rheometer plate (Figure 7a). For each sample the 12.5 mm parallel plate was used, and the gap was set by lowering the geometry until the surface of the gel was reached. We opted to set the gap manually for each sample by lowering the geometry until it reached the surface of the gel, as it was noted that using the same gap each time was not suitable due to slight variations in sample height. These height differences are likely to be a result of pouring the pre-gel solution into the 24 well plate. Likewise, we deemed it inappropriate to lower until a particular normal force was reached due to the soft nature of the gels. This meant that when lowered until a particular normal force was reached the plate geometry often penetrated the gel and disrupted the network. Before each measurement, the geometry was left for 5 minutes in the measuring position to allow the sample to adjust to the normal force applied. Initially, 1 mL of hydrogel was formed in the plates, resulting in a sample thickness of approximately 5 mm, as this is the volume used for cell culture (Figure 7bi-cii). These results were then compared to 2 mL samples, with a thickness of around 10 mm, as this is the volume usually used for carrying out cup and vane experiments (Figure 7di-eii). The resulting strain sweep data for each sample displayed very short linear viscoelastic regions, reaching a breakpoint at a strain of less than 0.1 % (Figure 7b-di).

### Chapter 3

We hypothesise that this rapid decrease in moduli with increasing strain, is due to a phenomenon known as slip. This behaviour occurs when a thin liquid layer is formed between the wall and the hydrogel.<sup>28</sup> Slippage tends to be more prominent in measurements taken using a parallel plate set up than a cup and vane.<sup>29</sup> Samples were also found to exhibit a significantly higher  $G'$  and  $G''$  initially than their corresponding vane strain sweeps (Figure 7c and d). This increase in moduli is likely due to the compressional stress stiffening behaviour which is commonly observed in the rheology of soft materials.<sup>29</sup> The rheological data was almost identical for each volume and condition, except for the 2 mL sample which had not undergone a heat-cool cycle (Figure 7d). These samples displayed a lower  $G'$  than the other hydrogels and large error bars at high frequency, suggesting they may not be fully frequency independent (Figure 7dii). This is interesting considering that the cup and vane measurements revealed almost identical strain sweep data for the 2NapFF hydrogels with glucose, regardless of whether they had undergone a heat-cool cycle prior to gelation (Figure 7c and d). To determine if this variation was due to the geometry used or the gel container, we repeated the 2 mL vial measurements using a parallel plate (12.5 mm diameter).

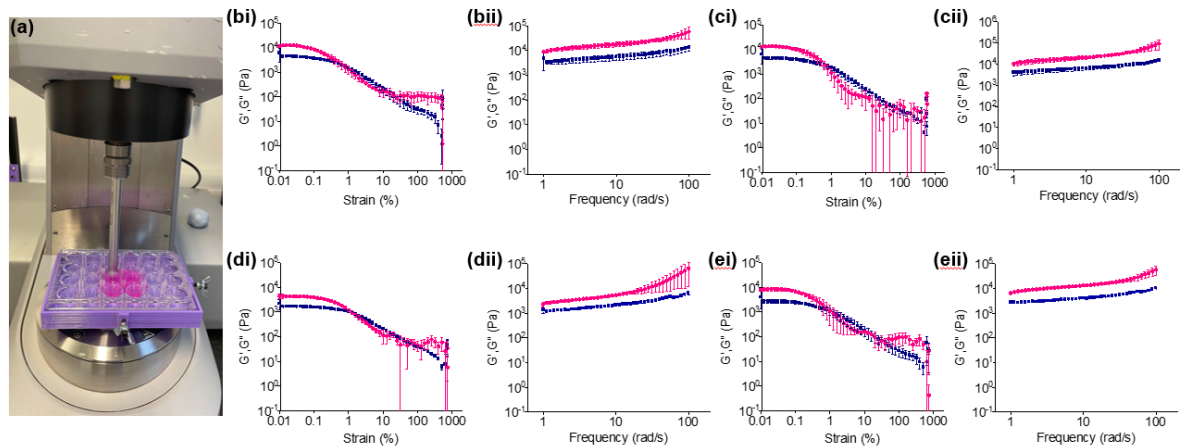


**Figure 7.** (a) Setup used to carry out measurements on gels formed in 24 well plates including custom 3D printed holder using the parallel plate (12.5 mm) geometry. (bi-ii) Strain and frequency sweeps carried out on 1 mL 2NapFF/DMEM gels with glucose formed in 24 well plates (ci-ii) Strain sweep and frequency sweeps carried out on 1 mL 2NapFF/DMEM gels with glucose which had undergone a heat/cool cycle before gelation formed in 24 well plates. (di-ii) Strain and frequency sweeps carried out on 2 mL 2NapFF/DMEM gels with glucose formed in 24 well plates (ei-ii) Strain sweep and frequency sweeps carried out on 2 mL 2NapFF/DMEM gels with glucose which had undergone a heat/cool cycle before gelation formed in 24 well plates. All measurements were carried out using a 12.5 mm parallel plate geometry. In each case, the pink data represent  $G'$  and the black data represent  $G''$ . Error bars are representative of the standard deviation between triplicates carried out using three different samples.

A 3D printed vial holder was secured to the flat plate of the rheometer to allow samples prepared in Sterilin vials to be measured using the 12.5 mm parallel plate geometry (Figure 8a). The results obtained were similar to those carried out on the samples in 24 well plates, with respect to displaying an increase in moduli compared to the measurements using the vane geometry. Again, we assumed this effect was due to compression by the parallel plate. In contrast to the results obtained from the hydrogels formed in 24 well plate, the samples prepared in vials displayed no linear viscoelastic region at all. A possible explanation for this, is that due to the smaller diameter of the vials (14.5 mm) compared to the wells (15.6). While this is a small difference in diameter, we hypothesise that the liquid-like properties of the surface are more concentrated below the parallel plate. In general, these results have shown that relating the storage modulus directly to cell behaviour may be insufficient, as the values differ depending on the set ups used for measurements.

### Chapter 3

This agrees with previous literature which states that in order to relate the viscoelastic properties of a gel to cell behaviour, we must take into consideration the compressional stress applied to the samples, as well as the size of the geometry used.<sup>30, 31</sup> These observations suggested further examination of the surface properties of these hydrogels was necessary.

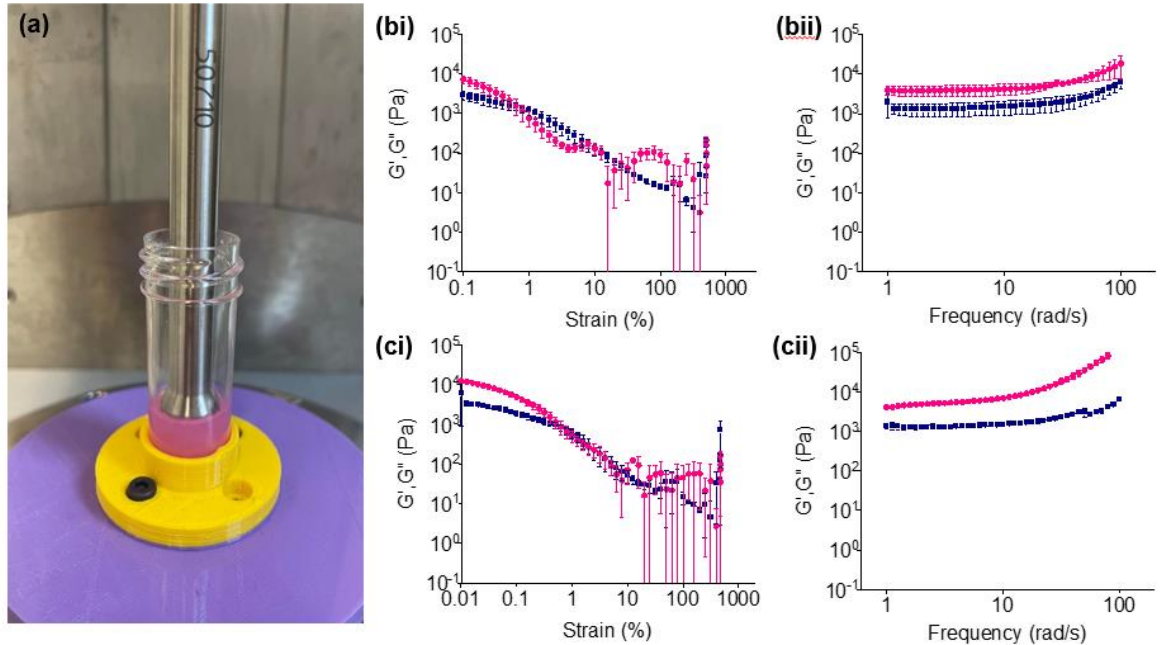


**Figure 8.** (a) Setup used to carry out measurements on gels formed in Sterilin vials using the parallel plate (12.5 mm) geometry, including custom 3D printed holder. (bi-ii) Strain and frequency sweeps carried out on 2 mL 2NapFF/DMEM gels with glucose formed in Sterilin vials (ci-ii) Strain sweep and frequency sweeps carried out on 2 mL 2NapFF/DMEM gels with glucose which had undergone a heat/cool cycle before gelation in Sterilin vials. All measurements were carried out using a 12.5 mm parallel plate geometry. In each case the pink data represent  $G'$  and the black data represent  $G''$ . Error bars are representative of the standard deviation between triplicates carried out using three separate samples.

Cavitation rheology was developed by Zimberlin et al,<sup>32</sup> and allows localised areas within the sample to be examined, as opposed to the bulk which is measured by shear rheology.<sup>32</sup> In summary, the process involves inserting a needle into the sample, through which air is pushed in via a syringe pump, causing the formation of a bubble. As the bubble grows the pressure increases, until the critical pressure ( $P_c$ ) is reached and the bubble bursts (Figure 9a). The data collected can be plotted as shown in Figure 9b. The critical pressure value obtained corresponds to the elastic modulus of the network, with a higher ( $P_c$ ) value denoting a stiffer network.<sup>32, 33</sup>

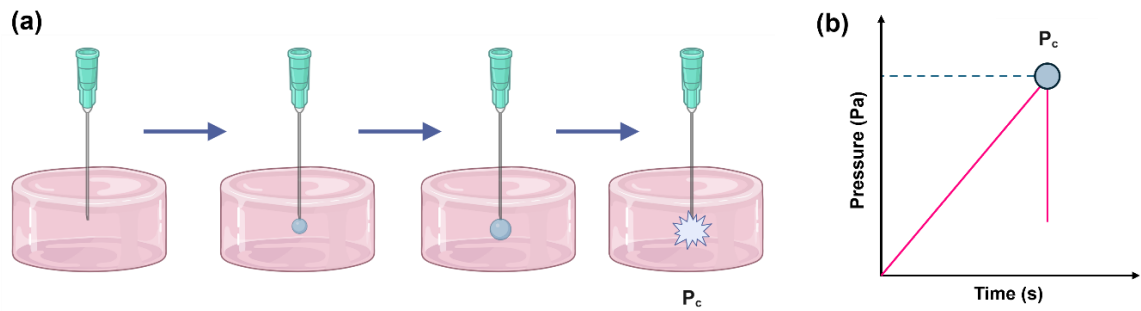


**Figure 9.** (a) Cartoon showing how cavitation rheology is carried out. A needle is inserted into the sample at a certain depth, before air is pushed into the sample causing the formation of a bubble within the gel. As the pressure increases, the bubble grows until the critical pressure ( $P_c$ ) is reached and the bubble bursts. (b) Cartoon showing an example cavitation rheology output, where the  $P_c$  is represented by a blue dot.

Cavitation rheology is particularly useful as it allows samples to be measured in their native environment, while oscillatory rheology requires samples to be prepared in specific vessels to be loaded onto the rheometer.<sup>31</sup> Thus, by employing cavitation rheology we can investigate the surface properties of the gels formed in 24-well culture plates. This approach provides insight into the forces that the cells cultured on the hydrogels experience. We compared samples in 24 well plates and in Sterilin vials (which are used for cup and vane rheology). Furthermore, for 2D culture only 1 mL of hydrogel per well was used, whereas to carry out rheology using the cup and vane geometry 2 mL of the samples must be used. For this reason, we performed cavitation rheology on 1 mL and 2 mL samples in each vessel. Each sample was prepared in triplicate with the needle being inserted in the centre of each gel for measurement at a depth of 1 mm below the surface. The error displays the standard deviation between measurements. The cavitation apparatus used to carry out these measurements was built by Bart Dietrich (University of Glasgow) using the original description from Zimmerlin et al.<sup>31</sup> The apparatus consists of a 10 mL Hamilton™ 1000 series Gas tight syringe mounted in a syringe pump (World Precision Instruments AL-1000). This is equipped with a high precision manometer or CRAB (Cavitation Rheology Analyser Box) with data logging capability was custom-built to control and record the pressure. A digital manometer was connected into the system via Y-junction and used to calibrate and double confirm pressure readings from the CRAB (Figure 10).<sup>33</sup>

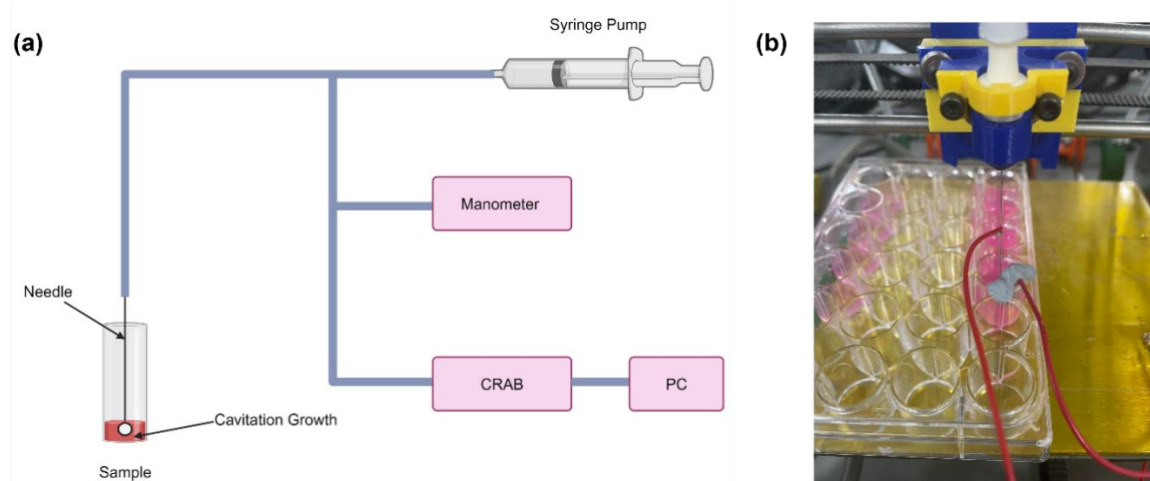


**Figure 10.** (a) Schematic of the cavitation rheometer set up used in this thesis. (b) Image of sample in 24-well plate being measured using the cavitation rheometer set-up.

The results obtained from the 1 mL hydrogels revealed that the 2NapFF/DMEM hydrogels formed in the Sterilin vial reached a significantly higher critical pressure than those formed in a 24 well plate (Figure 11a). This may suggest that the thickness of the sample prepared is affecting the self-assembly, as the Sterilin vials have a smaller surface area than the 24 well plates. We hypothesise that this smaller surface is leading to the fibres packing closer together, resulting in a stiffer network. In contrast, the samples which had undergone a heat-cool cycle before gelation produced critical pressures values within error of each other. A possible explanation for this result is that the high level of order which comes from the heat-cooling a solution of 2NapFF leads to highly reproducible hydrogels.

Regarding the 2 mL samples, it was found that both hydrogels displayed higher critical pressures when formed in 24 well plates compared to in Sterilin vials (Figure 11b). Moreover, both gels displayed similar critical pressures in the vials and 24 well plates, regardless of whether they had undergone a heat/cool cycle before gelation. This result suggests that the vessel in which the samples are prepared may have a larger influence on the surface properties than the pre-gelling heat-cool cycle. Generally, the 2 mL sample measurements displayed a larger error than the 1 mL hydrogels and thus are less reproducible. A possible explanation for this result could be that the larger sample size causes a higher viscosity on the surface of the hydrogels, as noted above with the parallel plate measurements. This increased liquid-like behaviour may be responsible for the higher level of variation observed between the triplicates.

### Chapter 3

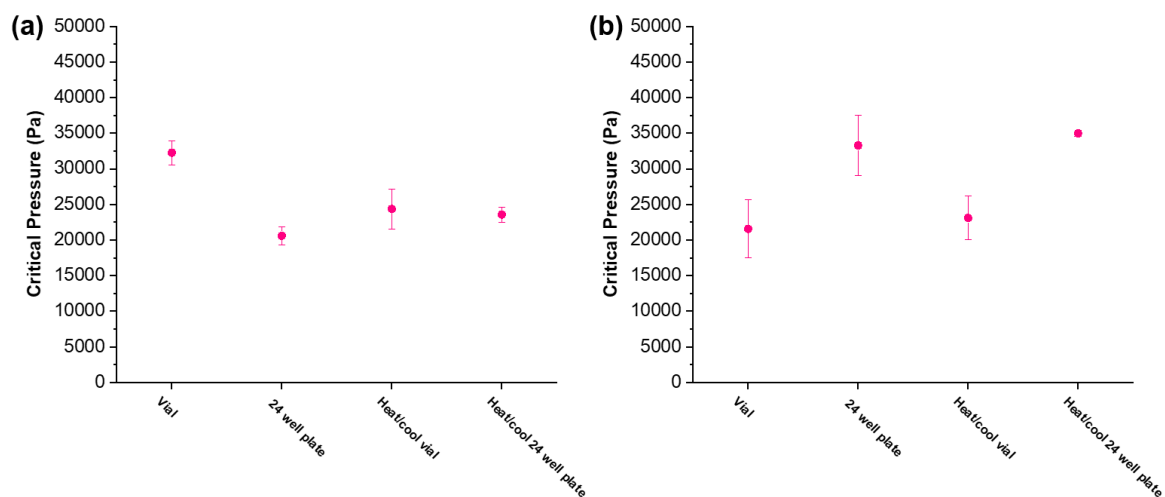


**Figure 11.** (a) Cavitation measurements for the 1 mL hydrogels formed in vials and 24 well plates. (b) Cavitation measurements for the 2 mL hydrogels formed in vials and 24 well plates. Error bars are representative of the standard deviation between triplicate sample. In each case one samples was used per measurement.

To further characterise these systems, confocal microscopy was used to probe their microstructure. This technique is a popular alternative to scanning electron microscopy (SEM) or transmission electron microscopy (TEM) when investigating soft materials, as it does not require the samples to be dried which may lead to artefactual changes in the assembled structures.<sup>33</sup> The addition of a fluorescent dye, in this case Nile blue, to the 2NapFF solution before gelation is triggered allows the dye to be incorporated into the hydrogel network during self-assembly. Therefore, we can image the underlying microstructure in a non-invasive manner. The images obtained suggest there is an underlying fibrous network in these gels, regardless of whether the samples had been heated and cooled before gelation (Figure 12).

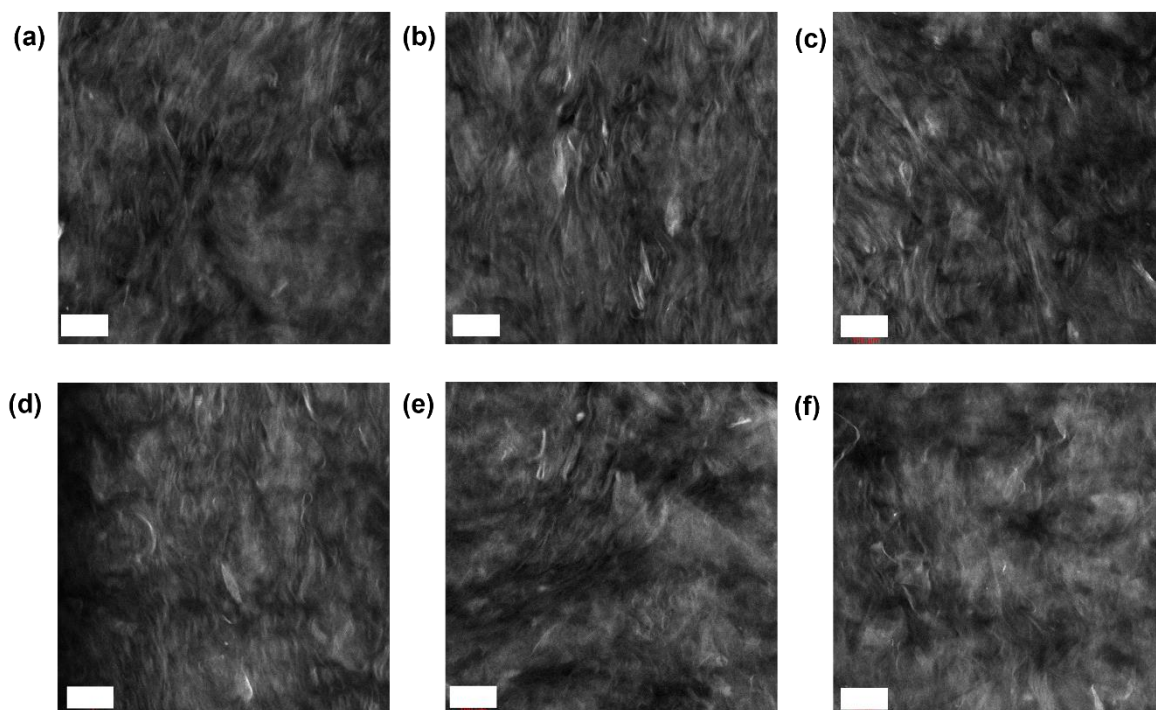


**Figure 12 (a-c)** Confocal images of 2NapFF/DMEM gels with glucose. **(d-e)** Confocal images of 2NapFF/DMEM gels with glucose which have undergone a heat-cool cycle before gelation. Images were collected using an A Zeiss LSM710 confocal microscope (Zeiss, Gottingen, Germany) and software Carl Zeiss ZEN 2011 v7.0.3.286 with an LD EC Epiplan NEUFLUAR 50X, 0.55 DIC (Carl Zeiss, White Plains, NY, USA) objective was used. All samples were prepared in a CELLview™ (Greiner Bio-One, Stonehouse, UK) 35 mm plastic cell culture dish with a borosilicate glass bottom. The samples were stained with 0.1 wt% Nile blue A solution, and excited at 634 nm using a He–Ne laser (Zeiss, Gottingen, Germany). Images were processed in ImageJ to create max-projection images of the original z-stacks. Scale bar represents 100  $\mu\text{m}$  in each case.

While the images obtained using confocal microscopy gave some information about the microstructure of the samples, it was still necessary to probe the one-dimensional structures which underpin these hydrogel systems. To do this, we employed small angle-x-ray scattering (SAXS). This technique allows us to investigate the primary structure at a 1-100 nm scale in its hydrated state. The data output is plotted as an Intensity (I) vs scattering vector (Q) plot, which is fitted to various models using SasView 5.0.6 software. Often the data can be fit to more than one model, thus we must consider the error value ( $\chi^2$ ) of each fit. Generally, if the value is between 1 and 10, we can assume that the model used is a reasonable fit for the data.

### Chapter 3

Our results revealed that the samples that had undergone a heat-cool cycle before gelation, produced significantly different plots to those formed from the pre-heated solution (Figure 13a and d). It was found that the type of media used to trigger gelation has little effect on the resulting one-dimensional fibres. We were able to draw this conclusion as the scattering plots of the 2NapFF/DMEM gels and of 2NapFF/DMEM with glucose could be overlaid (Figure 13a) as could 2NapFF/DMEM gels and of 2NapFF/DMEM with glucose formed from a solution which had undergone a heat-cool cycle (Figure 13d).

For this reason, we decided to fit the data from the 2NapFF/DMEM with glucose hydrogels as we can assume the values obtained will be the same as the 2NapFF/DMEM samples. The data fit best to a flexible cylinder model, with polydispersity applied to the radius. The length was fixed to 2000 Å and not refined during the fitting process (Figure 13b). The values obtained for Kuhn length and radius were 300 Å and 124 Å respectively (Table 1). In contrast, 2NapFF/DMEM with glucose samples which had undergone a heat-cool cycle fit best to an elliptical cylinder model (Figure 11d). These structures were significantly shorter than those formed from the native solution, with a length of 505 Å. The elliptical cylinders were found to have a minor radius of 54 and an axis ratio of 3 (Table 1). These results are particularly interesting when we consider that the 2NapFF/DMEM with glucose gels presented very similar rheological properties, regardless of whether the solution had been heated or not. This suggests that while the pre-gelation heat/cooling may have little effect on the bulk gel properties of these samples, the primary structures underpinning the network are affected. However, as mentioned in section 2.7.3, it is important to evaluate the uniqueness of the chosen SAXS fits. This means that the data may fit to several different form factors thus, future work should involve employing other techniques to verify these fits.

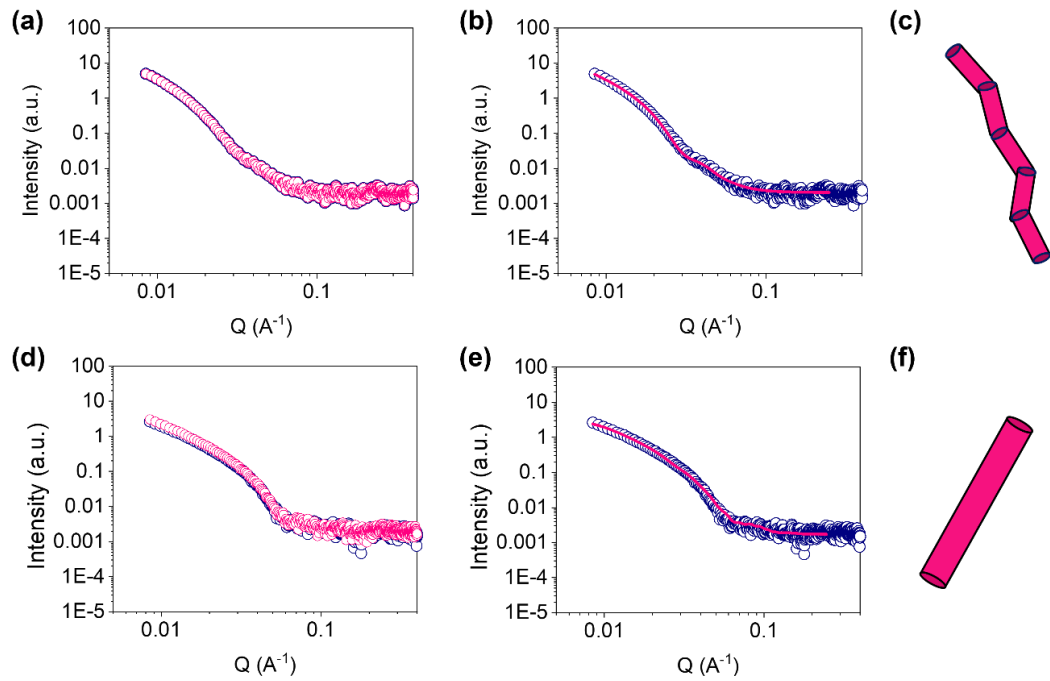


**Figure 13.** (a) Plots of SAXS data of 2NapFF/DMEM gels (pink) and of 2NapFF/DMEM with glucose (navy) overlaid. (b) SAXS data of 2NapFF/DMEM with glucose (navy) and fit (pink). (c) cartoon (not to scale) of structure represented by fit (flexible cylinder) (d) Plots of SAXS data of 2NapFF/DMEM gels (pink) and of 2NapFF/DMEM with glucose (navy) formed from a heat-cooled solution. (e) SAXS data of 2NapFF/DMEM with glucose formed from a heat-cooled solution (navy) and fit (pink). (f) cartoon (not to scale) of the structure represented by fit (elliptical cylinder).

### Chapter 3

**Table 1.** Summary of the parameters obtained from fitting SAXS data collected for each sample. The error of each parameter is shown below each value. Fitting parameters obtained from SasView 5.0.6 model fitting of the SAXS data. In each case the calculated SLD value was 14.196 and 9.469 for the SLD solvent. See section 2.7.3 for full fitting details.

	<b>2NapFF/DMEM + glucose</b>	<b>Heat-cooled 2NapFF/DMEM + glucose</b>
<b>Model</b>	FLEXIBLE CYLINDER	ELLIPTICAL CYLINDER
<b>Scale</b>	$0.000114 \pm 3 \times 10^{-6}$	$0.000154 \pm 6 \times 10^{-7}$
<b>Background</b>	$0.00206 \pm 5 \times 10^{-5}$	$0.00172 \pm 5 \times 10^{-4}$
<b>Length / Å</b>	2000 (fixed)	$505 \pm 9$
<b>Kuhn Length / Å</b>	$300 \pm 28.2$	
<b>Radius / Å</b>	$124 \pm 1$	$53.8 \pm 0.3$
<b>Radius Polydispersity</b>	0.2	
<b>Axis Ratio</b>		$2.87 \pm 0.04$
<b>SLD</b>	14.196	14.196
<b>SLD Solvent</b>	9.469	9.469
$\chi^2$	1.19	1.02

### 3.2.2 Incorporating •PODS® Growth Factors

To determine if these hydrogels have potential to be used for encapsulation of biological species, we decided to incorporate PODS® from Cell Guidance Systems. PODS® are microcrystals formed via the self-assembly of polyhedron proteins which encase a protein cargo, with a typical size of 1-2  $\mu\text{m}$ .<sup>15</sup> Their ability to release proteins, such as growth factors, in a slow and controllable manner allows for the precise control of the cell culture environment, enhancing cell health.<sup>14</sup> Firstly, we investigated the effect these PODS® have on the gel network at a bulk scale, using oscillatory rheology as before. Samples were prepared as previously described, with the PODS® solution being added to the 2NapFF solutions (at a concentration of  $1 \times 10^7$  PODS® per mL), before the addition of DMEM with glucose. For control experiments not involving cells PODS® loaded with Green Fluorescent Protein (GFP-PODS®) were used.

We discovered that the incorporation of the PODS® had very little effect on the bulk rheology of the hydrogels. A slight increase in the linear viscoelastic region was detected when the PODS® were added to the 2NapFF/DMEM + glucose hydrogels, which may suggest that the PODS® are interacting with the hydrogel network in such a way that increases the strength of the gels (Figure 14a and b). Alternatively, no significant difference was observed at all when the PODS® were added to the heat-cooled samples (Figure 14c and d). Confocal microscopy was utilised to confirm the presence of GFP-PODS® in both systems (Figure 14e and f). However, it is difficult to gain any information on how the PODS® interact with the surrounding network from these images alone. Thus, we opted to use small angle scattering to further investigate the effect of PODS® on the hydrogels. The SAXS data revealed that 2NapFF/DMEM gels with glucose and  $1 \times 10^7$  PODS® per mL could be overlaid with the samples not containing PODS® (Figure 14g). This was also observed for the samples which had been heated to 60°C for 1 hour and allowed to cool before gelation. Therefore, the data from the samples containing PODS® can be fitted to the same model as the pristine hydrogels, i.e. the samples which had not undergone heat-cool cycles fit to a flexible cylinder model and those which were heated and cooled fit to an elliptical cylinder model (Table 1). These results indicate that the PODS® do not alter the primary one-dimensional structure of the hydrogel, as well as having no significant effect on the bulk rheological properties. This implies that PODS® can potentially be added to a hydrogel for functionalisation purposes, without disrupting the underlying network.

### Chapter 3

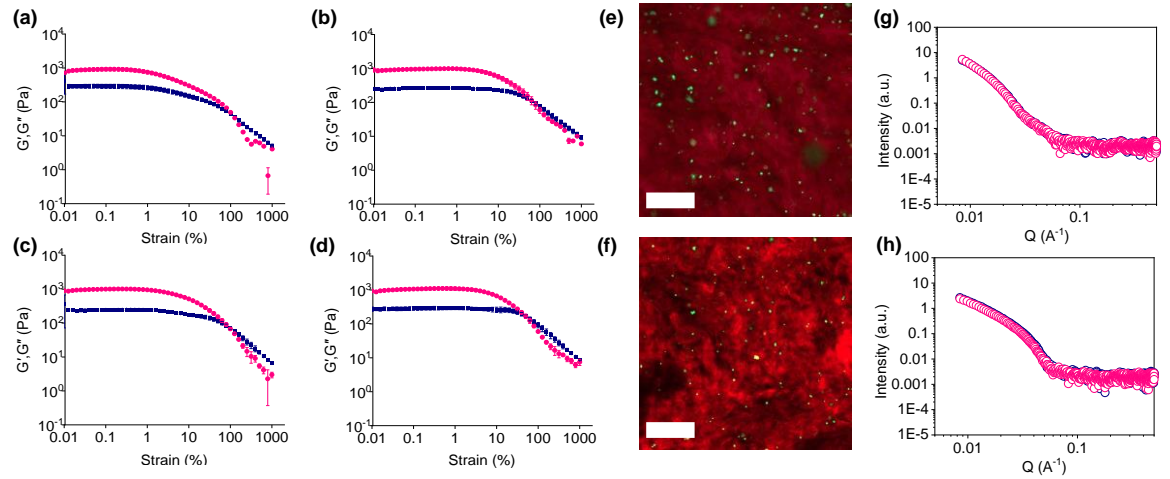


**Figure 14.** (a) Strain sweep data of 2 mL 2NapFF/DMEM+ glucose gels. (b) Strain sweep data of 2 mL 2NapFF/DMEM+ glucose gels with containing  $1 \times 10^7$  PODS® per mL. (c) Strain sweep data of 2 mL 2NapFF/DMEM + glucose heat-cool gels. (d) Strain sweep data carried out on 2 mL 2NapFF/DMEM + glucose heat-cool gels containing  $1 \times 10^7$  PODS® per mL. All measurements were carried out using the vane geometry with samples prepared in Sterilin vials. In each case the pink data is  $G'$  and the black is  $G''$ . In each case the error bars are representative of the standard deviation between triplicates, where one samples was used per measurement. (e) Confocal microscopy image of 2NapFF/DMEM+ glucose gels containing  $1 \times 10^7$  GFP-PODS® per mL. (f) Confocal images of 2NapFF/DMEM+ glucose heat cool gels containing  $1 \times 10^7$  GFP-PODS® per mL. Hydrogels stained red and PODS® green. Images were collected using an A Zeiss LSM710 confocal microscope (Zeiss, Gottingen, Germany) and software Carl Zeiss ZEN 2011 v7.0.3.286 with an LD EC Epiplan NEUFLUAR 50X, 0.55 DIC (Carl Zeiss, White Plains, NY, USA) objective was used. All samples were prepared in a CELLview™ (Greiner Bio-One, Stonehouse, UK) 35 mm plastic cell culture dish with a borosilicate glass bottom. The samples were stained with 0.1 wt% Nile blue A solution, and excited at 634 nm using a He–Ne laser (Zeiss, Gottingen, Germany). Scale bar represents 100  $\mu\text{m}$  in each case. (g) Plots of SAXS data of 2NapFF/DMEM + glucose gels (navy) and 2NapFF/DMEM + glucose, containing  $1 \times 10^7$  PODS® per mL (pink) overlaid. (h) Plots of SAXS data of 2NapFF/DMEM + glucose heat-cool gels (navy) and 2NapFF/DMEM + glucose heat-cool gels containing  $1 \times 10^7$  PODS® per mL (pink) overlaid.

### Chapter 3

As we intend to use these systems to culture mesenchymal stem cells (MSCs), we decided to also investigate how these cells affect the primary structures of the hydrogels. MSCs are much larger than PODS®, with an average diameter to 15-30  $\mu\text{m}$ .<sup>35</sup> To carry out this experiment, the mesenchymal stem cells were seeded on top of the hydrogels in 24 well plates at a density of  $1 \times 10^4$  cells per well. The samples were incubated overnight, before being fixed the following morning for ease of transport to the beamline. Cell fixation was carried out by removing the media, washing three times with PBS and adding formaldehyde on top of the samples. After 20 minutes, the formaldehyde was removed and three subsequent washes with PBS were carried out.

Finally, 1 mL of PBS was added on top of the gels to prevent drying out during transportation. Upon arrival, the samples were loaded into the gel cell apparatus for measuring as detailed in section 2.6.1.

Our results show that the scattering data produced by 2NapFF/DMEM + glucose gels, seeded with MSCs fit best to an elliptical cylinder with a power law (Figure 13 a and b). This is interesting as these samples usually fit to a flexible cylinder when cells are not included (Figure 13b). Previous work has shown that cylinders can laterally associate to form structures with elliptical cross-sections.<sup>36</sup> One possibility is that this increased aggregation may be due to the presence of the of the MSCS leading to crowding of the fibres (Figure 13e). Another possible explanation is that the formaldehyde used during fixation, lowers the pH of the hydrogel causing further aggregation. On the other hand, samples which had been through a heat-cool cycle before gelation, still fit best to an elliptical cylinder model when the cells were included. Despite this, the SAXS data does not completely overlay with the data from the heat-cool gels alone due to the different apparatus used, as samples containing cells were measured using a gel cell whereas all other samples were loaded into capillaries. To determine if the change of model observed for the samples which had not been heated before gelation was a result of the cells or the fixing process, we carried out SAXS, on samples which had been fixed but not containing cells.

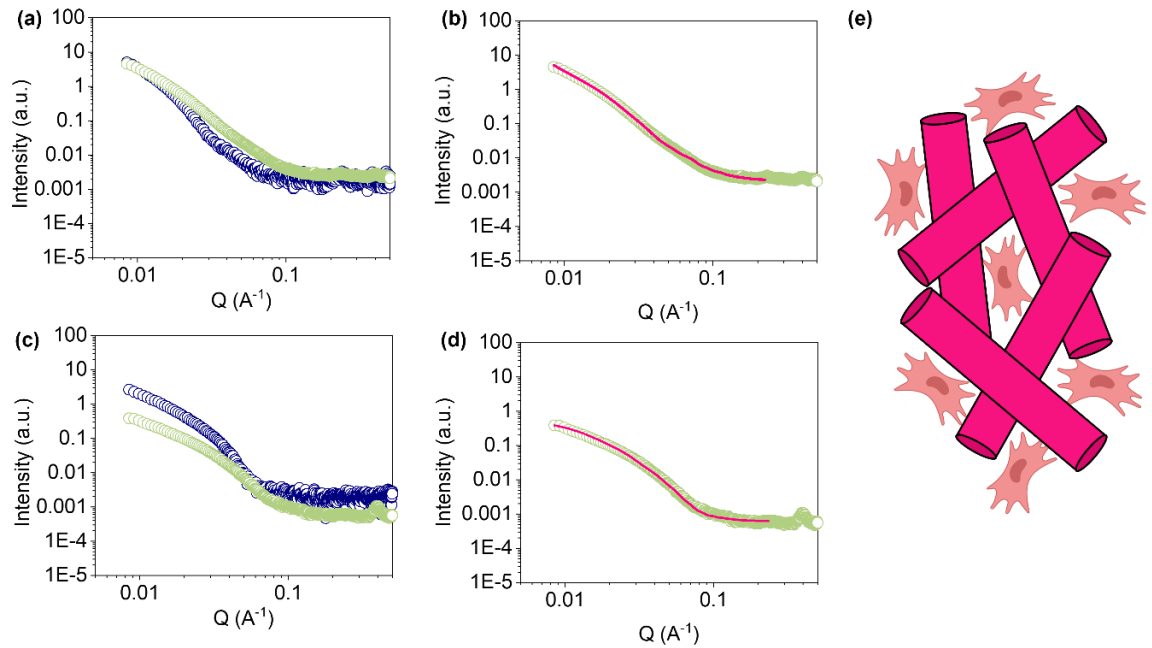


**Figure 15** Plots of SAXS data of 2NapFF/DMEM gels with glucose (navy) and of 2NapFF/DMEM with glucose seeded with  $1 \times 10^4$  MSCs per well (green) overlaid. **(b)** SAXS data of 2NapFF/DMEM with glucose seeded with  $1 \times 10^4$  cells per well (green) and fit (pink). **(c)** Plots of SAXS data of 2NapFF/DMEM heat-cool gels with glucose (navy) and of 2NapFF/DMEM heat-cool gels with glucose seeded with  $1 \times 10^4$  MSCs per well (green). **(d)** SAXS data of 2NapFF/DMEM heat-cool gels with glucose, seeded with  $1 \times 10^4$  cells per well (green) and fit (pink). **(e)** cartoon (not to scale) of the structure represented by fits (elliptical cylinder) with MSCs.

### Chapter 3

**Table 2.** Summary of the parameters obtained from fitting SAXS data collected for each sample. The error of each parameter is shown below each value. Fitting parameters obtained from SasView 5.0.6 model fitting of the SAXS data. In each case the calculated SLD value was 14.196 and 9.469 for the SLD solvent. See section 2.7.3 for full fitting details

	<b>2NapFF/DMEM + glucose with MSCs</b>	<b>Heat-cooled 2NapFF/DMEM + glucose with MSCs</b>
<b>Model</b>	ELLIPTICAL CYLINDER + POWER LAW	ELLIPTICAL CYLINDER
<b>A Scale</b>	$3.12 \pm 2 \times 10^{-7}$	$4.42 \pm 1.03 \times 10^{-7}$
<b>Background</b>	$0.00215 \pm 9.23 \times 10^{-6}$	$0.000619 \pm 4.57 \times 10^{-6}$
<b>A Length / Å</b>	$310 \pm 1.65$	1000 (Fixed)
<b>A Radius / Å</b>	$72.0 \pm 0.238$	$35.5 \pm 0.109$
<b>Axis Ratio</b>	$1.84 \pm 0.0150$	$2.84 \pm 0.0189$
<b>B Scale</b>	$1.59 \times 10^{-6} \pm 2.27 \times 10^{-8}$	
<b>B Power</b>	$3.08 \pm 0.00415$	
$\chi^2$	6.18	3.29

### Chapter 3

The 2NapFF/DMEM with glucose samples produced data which fit best to a flexible cylinder model with polydispersity applied to the radius, after fixation with formaldehyde for 20 minutes (Figure 16a). While this is the same model these samples fit to without cells or exposure to formaldehyde, there is variation between individual parameters. For example, the radius calculated for 2NapFF/DMEM with glucose is around 124 Å (Table 1), whereas once the samples undergo fixation, the radius is 46 Å, with 0.1 polydispersity applied (Table 3). Polydispersity is an indication that the structures present are not uniform in size, suggesting that structures with different-sized radii are present. This polydispersity may also point towards the increased aggregation of structures we could expect from the lowering of pH. Samples that had been through a heat-cool cycle prior to gelation still fit to an elliptical cylinder after the fixation process. The parameters for these samples showed no significant changes when cells were added or fixation occurred (Table 1-3), suggesting the primary structures remained unaltered by these processes. However, it is difficult to make any certain conclusions from these results as PODS® and MSCs are both outside the range measured by SAXS (1-100 nm), thus we can only draw conclusions about the effect on the structure within this scale.<sup>37</sup>

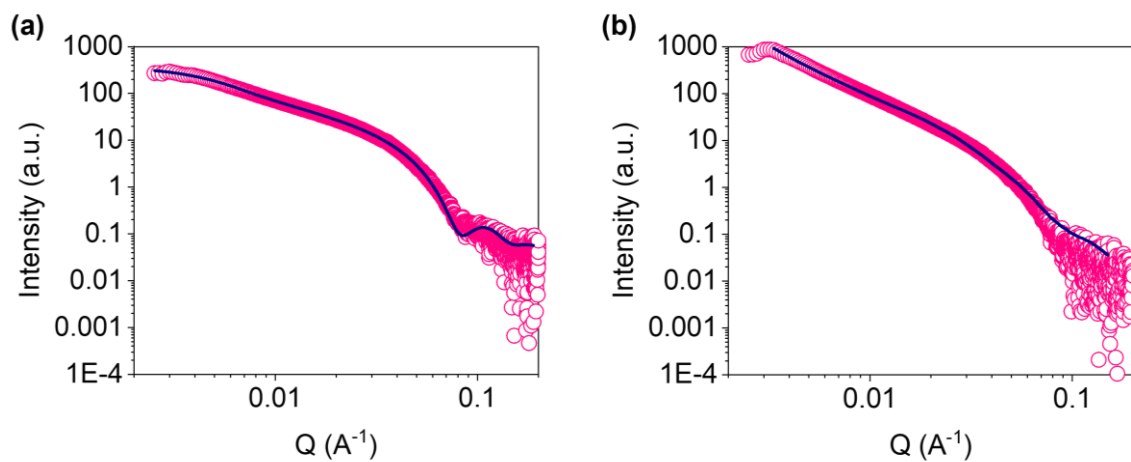


**Figure 16.** (a) SAXS data of 2NapFF/DMEM with glucose after exposure to formaldehyde for 20 minutes. (pink) and fit (navy). (b) SAXS data of 2NapFF/DMEM with glucose, which had undergone a heat-cool cycle before gelation, after exposure to formaldehyde for 20 minutes (pink) and fit (navy).

### Chapter 3

**Table 3.** Summary of the parameters obtained from fitting SAXS data collected for each sample. The error of each parameter is shown below each value. Fitting parameters obtained from SasView 5.0.6 model fitting of the SAXS data. In each case the calculated SLD value was 14.196 and 9.469 for the SLD solvent. See section 2.7.3 for full fitting details

	<b>2NapFF/DMEM + glucose after fixation with formaldehyde</b>	<b>Heat-cooled 2NapFF/DMEM + glucose after fixation with formaldehyde</b>
<b>Model</b>	FLEXIBLE CYLINDER	ELLIPTICAL CYLINDER + POWER LAW
<b>A Scale</b>	$0.0143 \pm 1.78 \times 10^{-5}$	$0.00721 \pm 5.69 \times 10^{-5}$
<b>Background</b>	0.002	0.002
<b>A Length / Å</b>	$1780 \pm 11.2$	$654 \pm 9.43$
<b>A Radius / Å</b>	$46.1 \pm 0.0405$	$38.3 \pm 0.2$
<b>A Radius Polydispersity</b>	0.1	
<b>Axis Ratio</b>		$2.60 \pm 0.0230$
<b>Kuhn length</b>	$510 \pm 3$	
<b>B Scale</b>		$0.000129 \pm 5.58 \times 10^{-6}$
<b>B Power</b>		$2.75 \pm 0.00768$
$\chi^2$	1.50	4.00

### 3.2.3 2D culture of mesenchymal stem cells

To investigate the biocompatibility of these hydrogels 2D culture was carried out on the gels using mesenchymal stem cells (MSCs). These cells were selected due to their non-hematopoietic, multipotent nature and their capacity to differentiate into cells such as osteocytes, adipocytes and chondrocytes as well neurocytes and hepatocytes.<sup>38</sup> These unique properties mean that they are of particular interest for tissue engineering applications. PODS® loaded with FGF-2 were used as this growth factor has been shown to stimulate growth of MSCs<sup>39</sup> as well as promote undifferentiated proliferation.<sup>40</sup>

### Chapter 3

After 3 and 7 days respectively, a live/dead viability assay was carried out and the cells were imaged using confocal microscopy. This assay involves two dyes; Ethidium homodimer-1 and Calcein-AM. Ethidium homodimer-1 stains dead cell nuclei red indicating loss of plasma membrane integrity as it is a cell-impermeable dye, and Calcein-AM is a cell-permeable dye which indicates intracellular esterase activity seen in live cells by staining with green fluorescence. Therefore, the live and dead cells exhibit green and red fluorescence, respectively. All cells imaged on the samples were found to be live.

We hypothesize that due to the lack of adhesive motifs included on the gels, any dead cells had been washed away during PBS washes before the dye was applied. It was also found that the 2NapFF/DMEM hydrogels are highly auto-fluorescent and stained by the Calcein-AM, thus we were unable to carry out analysis of the images. Nevertheless, we were still able to make some observations from the images collected. By day 3 both samples which did not contain PODS® contained very few cells and required a higher magnification to image small groups of cells (Figure 17a and b). A possible reason for this lack of cells, despite seeding at  $1 \times 10^4$  MSCs per well, is that many cells did not adhere to the gels and have been washed away. The FBS in the media used to form the hydrogels is possibly responsible for the few cells observed. After 7 days, there seemed to be some signs of cell proliferation (Figure 17g and h), particularly for the samples which did not undergo a heat-cool cycle. (Figure 17g). When the PODS® were added, more cells were visible by day 3 for both samples (Figure 15c and d). By day 7, the number of viable cells seemed to have increased (Figure 17i and j). In this case, the cargo used was FGF-2, which promotes cell proliferation and migration.<sup>41</sup> These results show an increased number of cells spread throughout the samples after seven days, when the PODS® are present (Figure 17i and j) compared to when they are not (Figure 17g and h). Therefore, this discovery supports the claim that PODS® release bioactive cargo over a prolonged time. In general, little difference in cell behaviour was noted between samples containing PODS® which had undergone a heat-cool cycle prior to gelation and those that had not. This implies that the incorporation of FGF-2 PODS® improves the biocompatibility of the heat-cooled samples at the day 7 time point. However, the control samples present more elongated phenotypes than the MSCs cultured on the hydrogels (Figure 17e and k), particularly when the PODS® are included (Figure 17f and i). Again, this is likely due to the lack of adhesive motifs included in the network.

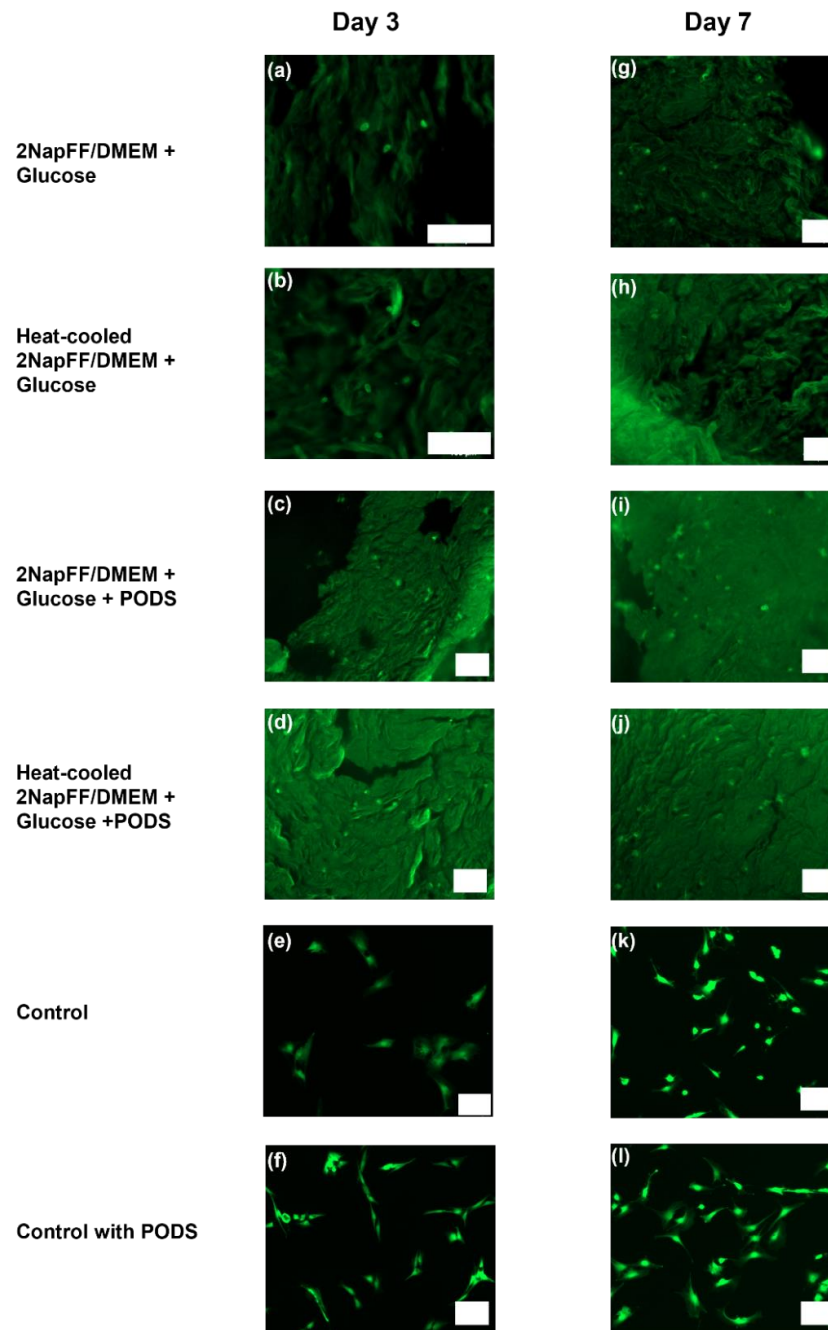


**Figure 17.** Live/dead cell viability assay of MSC cells cultured on the 1 mL 2NapFF/DMEM + glucose in 24 well plates with and without  $1 \times 10^7$  FGF-2 PODS® per mL. The cells were cultured for 3 day or 7 days and then stained with the Cellstain double staining kit. The live and dead cells show green and red fluorescence, respectively. MSC grown on the 24 well plate without a hydrogel were used as a control to ensure the cells were viable. MSCs grown on the 24 well plate with  $1 \times 10^7$  FGF-2 PODS® were used as a second control. Imaging was carried out using a Zeiss LSM 980 microscope using 10x objective. Images were processed in ImageJ to create max-projection images of the original z-stacks. Scale bar represents 100  $\mu\text{m}$ .

### 3.3 Conclusions

In this chapter, we have demonstrated the gelation of 2NapFF hydrogels at physiological pH using cell culture media. We then went on to investigate the effect of heating a solution to 60°C and cooling to room temperature before gelation was triggered. While the rheological properties of the 2NapFF/DMEM hydrogels with glucose were very similar, regardless of whether they had been heated as solutions, the SAXS data produced fit to two different cylinder models. In contrast, it was noted that the media used to carry out the crosslinking of 2NapFF impacts the rheological properties of the resulting hydrogel, but SAXS measurements found negligible variation between the primary fibres. These findings reiterate the importance of characterisation across multiple length scales to understand these materials. We also believe this is a significant finding considering media with different supplements are often used interchangeably. Furthermore, we found that when samples were prepared at physiological temperature, they experienced an increase in storage modulus. This highlights the impact that temperature has on the self-assembly of this gelator and underlines the need to maintain consistent environmental conditions for reproducibility.

We also carried out a thorough rheological study using different geometries and measuring samples formed in various vessels. Our results emphasise the effect of the measuring system used on the rheological properties observed, with the vane and parallel plate producing vastly different data for the same samples. Small angle scattering experiments were conducted to investigate the differences in primary structures when PODS® were introduced. It was concluded that these additives had little impact on the one-dimensional fibres present and thus can be used to elevate the bioactivity of the systems, without altering the network. The increase in bioactivity was confirmed by a live/dead assay which showed higher cell proliferation after 7 days when PODS® were included. However, issues with imaging the samples may mean that further work is needed to confirm these findings. Furthermore, while the SAXS data remained unchanged by the presence of PODS® at a nanoscale, ultra-small angle x-ray scattering (USAXS) offers a larger range of up to 6 µm. Similarly, Dynamic Light Scattering (DLS) can be used to analyse structures up to 10µm. These techniques may provide further insight to the interactions occurring between PODS® and the hydrogel network.

### **Chapter 3**

To conclude, we have successfully characterised using a range of techniques including, oscillatory rheology, cavitation rheology, confocal microscopy, and small-angle x-ray scattering. Using PODS® from Cell Guidance Systems, were able to enhance the biocompatibility of the hydrogels to culture mesenchymal stem cells over seven days. Our findings point towards the potential use of these systems for use as cell culture scaffolds in the future, while highlighting the need for thorough characterisation of future biomaterials.

### 3.4 References

1. M. L. Jagrosse, P. Agredo, B. L. Abraham, E. S. Toriki and B. L. Nilsson, *ACS Biomater. Sci. Eng.*, 2023, **9**, 784-796.
2. B. L. Abraham, P. Agredo, S. G. Mensah and B. L. Nilsson, *Langmuir*, 2022, **38**, 15494-15505.
3. K. Wang, Z. Wang, H. Hu and C. Gao, *Supramolecular Materials*, 2022, **1**, 100006.
4. E. R. Draper and D. J. Adams, *Chem*, 2017, **3**, 390-410.
5. C. Colquhoun, E. R. Draper, R. Schweins, M. Marcello, D. Vadukul, L. C. Serpell and D. J. Adams, *Soft Matter*, 2017, **13**, 1914-1919.
6. R. E. Ginesi and E. R. Draper, *Soft Matter*, 2024, **20**, 3887-3896.
7. S. Debnath, S. Roy, Y. M. Abul-Haija, P. W. J. M. Frederix, S. M. Ramalhetete, A. R. Hirst, N. Javid, N. T. Hunt, S. M. Kelly, J. Angulo, Y. Z. Khimiyak and R. V. Ulijn, *Chem. Eur. J.*, 2019, **25**, 7881-7887.
8. P. Zhou, R. Xing, Q. Li, J. Li, C. Yuan and X. Yan, *Matter*, 2023, **6**, 1945-1963.
9. E. R. Draper, H. Su, C. Brasnett, R. J. Poole, S. Rogers, H. Cui, A. Seddon and D. J. Adams, *Angew. Chem. Int. Ed.*, 2017, **56**, 10467-10470.
10. X. Huang and C. S. Brazel, *J. Control Release*, 2001, **73**, 121-136.
11. J. C. Berkmann, A. X. Herrera Martin, C. Pontremoli, K. Zheng, C. H. Bucher, A. Ellinghaus, A. R. Boccaccini, S. Fiorilli, C. Vitale Brovarone, G. N. Duda and K. Schmidt-Bleek, *Pharmaceutics*, 2020, **12**.
12. W. J. E. M. Habraken, O. C. Boerman, J. G. C. Wolke, A. G. Mikos and J. A. Jansen, *Key Eng. Mater.*, 2008, **361-363**, 527-530.
13. P. Trucillo, *Materials*, 2024, **17**, 456.
14. Y. Matsuzaki, R. Maruta, K. Takaki, E. Kotani, Y. Kato, R. Yoshimura, Y. Endo, C. Whitty, C. Pernstich, R. Gandhi, M. Jones and H. Mori, *Biomolecules*, 2019, **9**, 510.
15. F. Coulibaly, E. Chiu, S. Gutmann, C. Rajendran, P. W. Haebel, K. Ikeda, H. Mori, V. K. Ward, C. Schulze-Briese and P. Metcalf, *Proc. Natl. Acad. Sci. U S A*, 2009, **106**, 22205-22210.
16. A. Wendler, N. James, M. H. Jones and C. Pernstich, *Biodes. Res.*, 2021, **14**, 9816485.
17. C. Whitty, C. Pernstich, C. Marris, A. McCaskie, M. Jones and F. Henson, *Osteoarthr. Cartil. Open*, 2022, **4**, 100240.

### Chapter 3

18. N. Nishishita, H. Ijiri, C. Takenaka, K. Kobayashi, K. Goto, E. Kotani, T. Itoh, H. Mori and S. Kawamata, *Biomaterials*, 2011, **32**, 3555-3563.
19. G. Matsumoto, R. Hirohata, K. Hayashi, Y. Sugimoto, E. Kotani, J. Shimabukuro, T. Hirano, Y. Nakajima, S. Kawamata and H. Mori, *Biomaterials*, 2014, **35**, 1326-1333.
20. B. Yi, Q. Xu and W. Liu, *Bioact. Mater.*, 2022, **15**, 82-102.
21. A. Wyma, L. Martin-Alarcon, T. Walsh, T. A. Schmidt, I. D. Gates and M. S. Kallos, *Biotechnol. Bioeng.*, 2018, **115**, 2101-2113.
22. L. R. Smith, S. Cho and D. E. Discher, *Physiology*, 2018, **33**, 16-25.
23. S. Li, Y. Zeng, W. Hou, W. Wan, J. Zhang, Y. Wang, X. Du and Z. Gu, *Mater. Horiz.*, 2020, **7**, 2944-2950.
24. J. L. Sumey, P. C. Johnston, A. M. Harrell and S. R. Caliari, *Biomater. Sci.*, 2023, **11**, 2886-2897.
25. M. D'Urso and N. A. Kurniawan, *Front. Bioeng. Biotechnol.*, 2020, **8**, 609653.
26. A. J. Engler, S. Sen1, H. L. Sweeney and D. E. Discher, *Cell*, **126**, 2006, 677 - 689
27. J. R. Stokes and J. H. Telford, *J. Nonnewton. Fluid Mech*, 2004, **124**, 137-146.
28. B. R. Maciel, K. Baki, C. Oelschlaeger and N. Willenbacher, *Chem. Ing. Tech*, 2022, **94**, 393-401.
29. H. A. Barnes in *A handbook of elementary rheology*, University of Wales, Institute of Non-Newtonian Fluid Mechanics, Wales (UK), 2000.
30. R. Ferraro, S. Guido, S. Caserta and M. Tassieri, *Soft Matter*, 2023, **19**, 2053-2057.
31. G. Ciccone, O. Dobre, G. M. Gibson, J. M. Rey, C. Gonzalez-Garcia, M. Vassalli, M. Salmeron-Sanchez and M. Tassieri, *Adv. Healthc. Mater.*, 2020, **9**, 2000517.
32. J. A. Zimmerman, N. Sanabria-DeLong, G. N. Tew and A. J. Crosby, *Soft Matter*, 2007, **3**, 763-767.
33. A. M. Fuentes-Caparrós, B. Dietrich, L. Thomson, C. Chauveau and D. J. Adams, *Soft Matter*, 2019, **15**, 6340-6347.
34. L. L. Mears, E. R. Draper, A. M. Castilla, H. Su, B. Dietrich, M. C. Nolan, G. N. Smith, J. Douth, S. Rogers and R. Akhtar, *Biomacromolecules*, 2017, **18**, 3531-3540.
35. J. Gao, J. E. Dennis, R. F. Muzic, M. Lundberg and A. I. Caplan, *Cells Tissues Organs*, 2001, **169**, 12-20.
36. E. R. Draper, B. Dietrich, K. McAulay, C. Brasnett, H. Abdizadeh, I. Patmanidis, S. J. Marrink, H. Su, H. Cui, R. Schweins, A. Seddon and D. J. Adams, *Matter*, 2020, **2**, 764-778.

### Chapter 3

37. N. Allec, M. Choi, N. Yesupriya, B. Szychowski, M. R. White, M. G. Kann, E. D. Garcin, M. C. Daniel and A. Badano, *Sci. Rep.*, 2015, **5**, 12085.
38. I. Ullah, R. B. Subbarao and G. J. Rho, *Biosci. Rep.* 2015, **35**, 25797907
39. L. Chen, M. Carlton, X. Chen, N. Kaur, H. Ryan, T. J Parker, Z. Lin, Y. Xiao and Y. Zhou, *Stem. Cell Res. Ther.*, 2021, **12**, 1757-6512
40. D. L. Coutu, M. François, J. Galipeau, *Blood*, 2011, **117**, 6801–6812.
31. L. Benington, G. Rajan, C. Locher and L. Y. Lim, *Pharmaceutics*, 2020, **12**.

## **Chapter 4: Investigating the self-assembly of 2NapFF and ureido-pyrimidinone multicomponent systems for cell culture**

This Chapter is adapted from the following publication:

“Investigating the self-assembly of 2NapFF and ureido-pyrimidinone multicomponent systems for cell culture.”

**Chloe M. Wallace**, Maritza M. Rovers, Riccardo Bellan, Martin G. T. A. Rutten, Annela Seddon, Matthew J. Dalby, Patricia Y. W. Dankers and Dave J. Adams

Preparation of small-angle x-ray scattering (SAXS) samples was carried out by C. Wallace (University of Glasgow). Collection and processing of SAXS data was carried out by A. Seddon (University of Bristol) and fitted by C. Wallace. Preparation of small-angle neutron scattering (SANS) samples was carried out by C. Wallace. Collection of SANS data was carried out by D. Adams and E. Draper (University of Glasgow). Processing of SANS data was carried out by J. Douth (ISIS Neutron Scattering) and data fitted by C. Wallace. Rheology data for system B was collected and processed by M. Rutten. All other rheology data were collected and processed by C. Wallace. Cryo-TEM measurements were carried out by R. Bellan. Cell work and imaging was carried out by M. Rovers.

### 4.1 Introduction

Supramolecular hydrogels are of growing interest for applications in regenerative medicine and bioengineering due to their unique properties.<sup>1</sup> Unlike covalently bonded hydrogels, the self-assembly of supramolecular hydrogels is driven by non-covalent interactions such as hydrogen bonding and  $\pi$ - $\pi$  stacking.<sup>2</sup> The ability of these gelators to self-assemble without covalent bonds mimics the hierarchical nature of extracellular matrix formation.<sup>3</sup> This property emphasises their potential use for tissue engineering.<sup>4</sup> As well as this, supramolecular hydrogels exhibit highly tuneable mechanical properties and degradability, which is crucial when developing biocompatible scaffolds and encapsulating bioactive moieties.<sup>1</sup> Ureido-pyrimidinone (UPy) based supramolecular polymers are promising candidates in the field of biomaterials and have already been employed as minimally invasive drug delivery systems to the heart and kidneys.<sup>5-7</sup> UPy-based supramolecular materials assembly via fourfold hydrogen bonding between self-complementary UPy-moieties (Figure 1a).<sup>8</sup> The resulting interaction is relatively strong but reversible due to the non-covalent nature of the hydrogen bonding.<sup>9</sup> By modifying a hydrophilic prepolymer, i.e. poly(ethylene glycol) (PEG) with UPy-units at the chain ends using a hydrophobic alkyl linker and additional urea groups, transient aqueous networks and hydrogels are formed.<sup>3, 5, 10, 11</sup>

Generally, these systems involved two types of molecular building blocks, monofunctional (M) and bifunctional (B) (Figure 1b).<sup>3, 12</sup> Previous work has revealed that UPy-monomers form one-dimensional fibres, and the bifunctional species act as crosslinkers to form transient networks.<sup>3</sup> When these gelators are utilised for cell culture applications the monomer UPy-cRGD is typically incorporated at a concentration of 1 mM, to enhance the cell adhesion of the hydrogels.<sup>3, 12</sup>

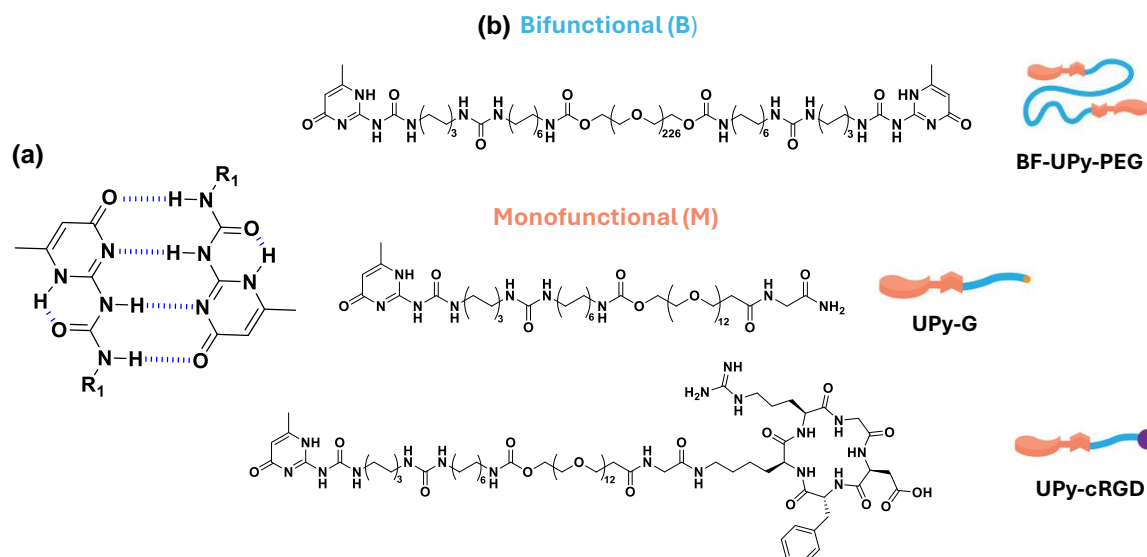


**Figure 1.** (a) Diagram showing the self-complementary quadruple hydrogen bonding between two UPy- units, where “R” represents the respective polymer linker. (b) Structures of bifunctional (B)-type and monofunctional (M)-type molecules as the supramolecular building blocks and additives.

The monofunctional (M)-type UPy monomers belong to a sub-category of supramolecular gelators called low molecular weight gelators (LMWG), which are of great interest in the biomedical field.<sup>13, 14</sup> As noted previously, these gelators are small molecules that self-assemble into one-dimensional structures, which then entangle into bundles or form a viscoelastic network when a (B)-type crosslinker is present ( $M_n = 10$  kDa, which yields  $n=226$  on average; where  $n$  is the number of repeating PEG units; BF-UPy-PEG).<sup>3</sup> As mentioned in Chapter 2, *N*-protected dipeptides are another group of widely explored LMWG. Such dipeptides are commonly protected with a fluorenylmethyloxycarbonyl (Fmoc) or naphthalene (Nap) group at the N-terminus, which contributes to the  $\pi$ - $\pi$  stacking interactions that promote gelation.<sup>15-17</sup> The aromatic residues present have been found to affect the elasticity of a gel.<sup>18</sup> One thoroughly investigated LMWG within our group is 2NapFF, a naphthalene-protected diphenylalanine.<sup>19, 20</sup> This amphiphilic dipeptide is capable of forming hydrogels via a range of different triggers including crosslinking with divalent cations. This occurs when a divalent metal salt is added to a geator solution at high pH, causing a metal-coordinated crosslinked gel structure to form.<sup>21</sup>

## Chapter 4

Multicomponent supramolecular systems can be used to access novel properties of a material.<sup>22-25</sup> This is because the self-assembly of these systems, results in the formation of either self-sorted or co-assembled structures.<sup>26, 27</sup> Self-sorted systems arise from each self-assembled structure containing only one of the species present.<sup>28</sup> In contrast, co-assembled structures are composed of a mixture of each component.<sup>29</sup> However, it is also worth noting that the properties of the individual components can be compromised when a multicomponent approach is employed. For this reason, fine-tuning each component is required to maximise the benefits of a multicomponent system.

A plethora of multicomponent LMWG systems have been reported for cell culture applications, including a combination of FmocFF with FmocRGD<sup>30</sup> or FmocS.<sup>31</sup> In this Chapter we investigate the multicomponent self-assembly of 2NapFF and UPy-based networks as a complementary approach. To do so we exploit a combined system with UPy building blocks that allows for a modular approach, enabling the integration of various UPy functionalities. Moreover, different UPy additives have been found to positively impact cellular response.<sup>32</sup> We examine these systems across a range of length scales using techniques including small-angle X-ray scattering (SAXS), small-angle neutron scattering, cryo-transmission electron microscopy (cryo-TEM) and rheology. Finally, we analyse the biocompatibility of the systems using fibroblast cells (Figure 2).

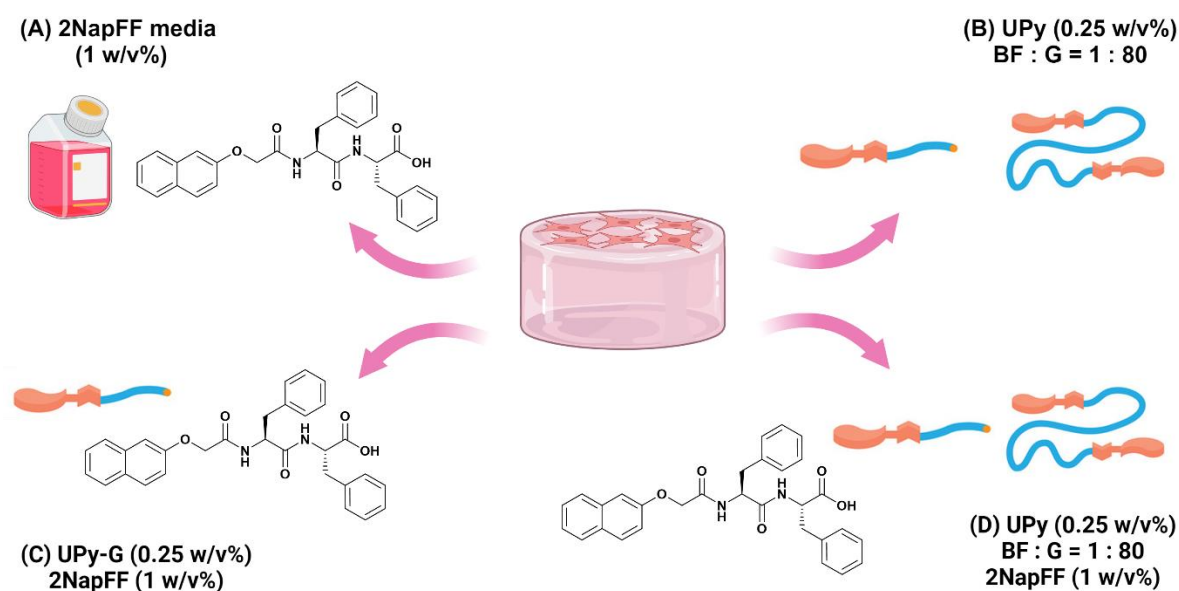


**Figure 2.** Graphical abstract depicting the work discussed in this chapter, involving the use of 2NapFF/UPy multicomponent systems for cell culture applications.

## 4.2 Results and Discussion

In this chapter, we compare the 2NapFF hydrogels crosslinked with DMEM discussed throughout this thesis, with a biocompatible UPy hydrogel system. We used the bifunctional UPy-PEG species as a crosslinker and the monofunctional UPy-G (Figure 1b). The UPy components were prepared by dissolving UPy-G in 80 mM NaOH and BF-UPy-PEG in PBS (1X) solution. The ratio of bifunctional to monofunctional monomer used was 1:80 (B:M=1:80). The solutions were heated at 70 °C for 1 hour and 30 minutes for the bifunctional and monofunctional respectively before the UPy-G solution was neutralised with 1 M HCl. The solutions were then mixed in the correct proportions to achieve gels at the desired concentrations, before adding this solution to an equal volume of 2NapFF solution at pH 7 if required (Figure 3). For clarity, we have named these systems A-D as detailed in Table 1.

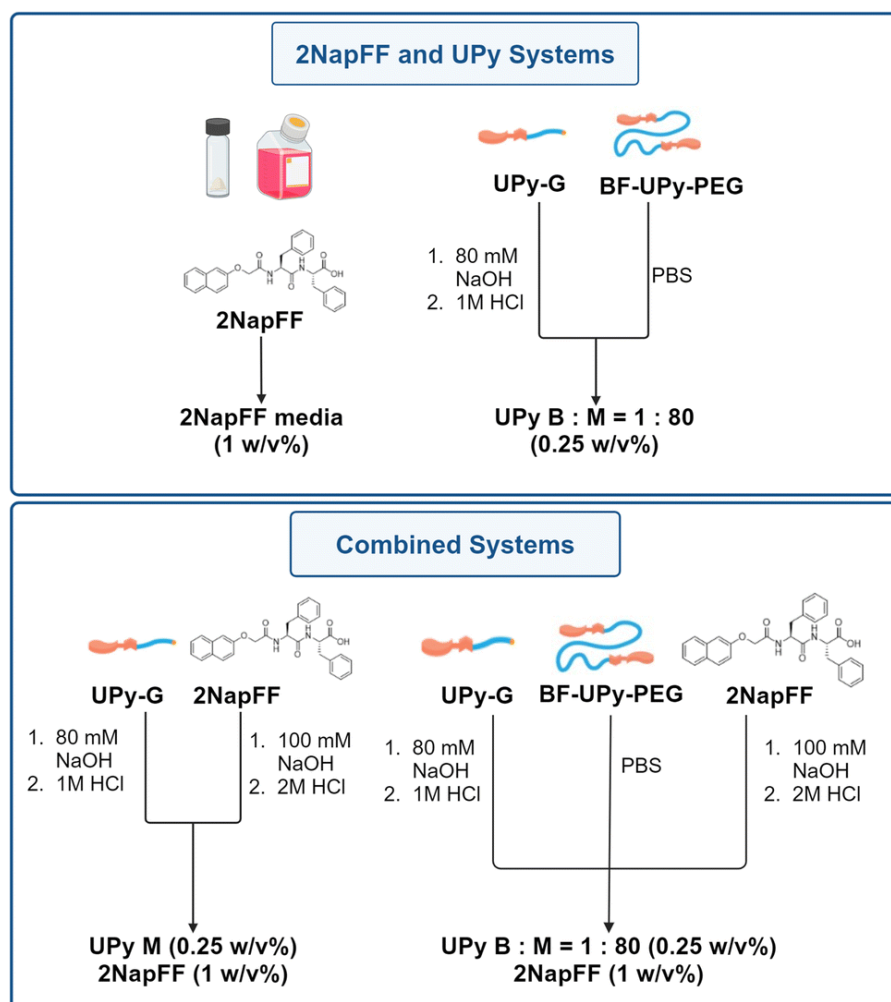


**Figure 3.** Schematic showing the preparation of the four gel systems used here formed from 2NapFF, UPy-G and BF-UPy-PEG in different combinations. For full experimental details see experimental section 3.4.

**Table 1.** Table showing the names of samples (A-D) and their corresponding composition

Name	Hydrogel Composition
<b>A</b>	<b>2NapFF media (1 w/v%)</b> - 2NapFF crosslinked with Gibco Dulbecco's Modified Eagle Medium (DMEM)
<b>B</b>	<b>UPy B: M = 1:80 (0.25 w/v%)</b> - bifunctional BF-UPy-PEG species as a crosslinker and the monofunctional UPy-G. The ratio of bifunctional to monofunctional monomer used was 1:80.
<b>C</b>	<b>UPy M (0.25 w/v%), 2NapFF (1 w/v%)</b> - Monofunctional UPy-G and 2NapFF.
<b>D</b>	<b>UPy B: M = 1:80 (0.25 w/v%), 2NapFF (1 w/v%)</b> - BF-UPy-PEG and UPy-G at a ratio of 1:80 combined with 2NapFF.

#### 4.2.1 Small-Angle Scattering (SAXS and SANS)

To analyse the nanoscale structures present in these systems, we used small-angle X-ray scattering (SAXS). The SAXS data collected for the 2NapFF gels (A) fit best to a cylinder model (Figure 4a), with the fit showing that the underpinning structures have a radius of 44 Å and a length of 541 Å (Table 2). This is different from the models that 2NapFF hydrogels have previously been fitted to and is likely due to the neutral pH and the salts present in the DMEM buffer.<sup>20</sup> On the other hand, the data for the UPy hydrogels (B), fit best to a flexible elliptical cylinder model (Figure 4b). The resulting fits revealed the UPy structures to be significantly longer than the 2NapFF, with a length of over 898 Å, a Kuhn length of 225 Å, minor radius of 36 Å and an axis ratio of 1.7 Å. The C systems also generated data that best fit a flexible elliptical cylinder model, with parameters resembling those of the pristine UPy samples (Figure 4c) (Table 2). Notably, upon introducing the bifunctional crosslinking species, the D hydrogels fit best to a cylinder model with parameters within the error of those obtained from the 2NapFF (A) hydrogels (Figure 4d).

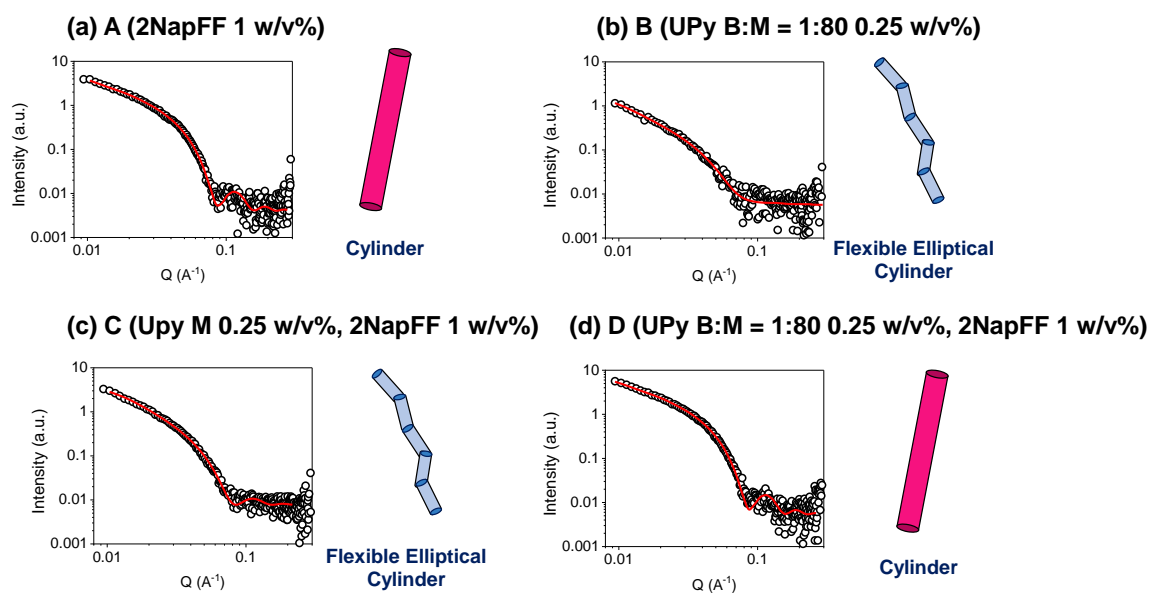


**Figure 4.** Plots of SAXS data (circles) and fits (red solid lines) along with cartoon (not to scale) of structure represented by fit for (a) A (2NapFF 1 w/v%) (b) B (UPy B:M = 1:80, 1 w/v %) (c) C (UPy-M 1.25 w/v %, 2NapFF 1 w/v%) (d) D (UPy B:M = 1:80 1.25 w/v)

**Table 2.** Summary of the parameters obtained from fitting SAXS data collected for each system. The error of each parameter is shown below each value. Fitting parameters obtained from SasView 5.0.6 model fitting of the SAXS data. The calculated SLD values were 14.196, 9.862, 12.177 and 18.140 for systems A-D respectively. The SLD solvent used was 9.469. See section 2.7.3 for full fitting details

	2NapFF 1w/v%	UPy 0.25w/v% B:M = 1:80	UPy 0.25w/v% 2NapFF 1w/v%	UPy B:M =1:80 2NapFF 1w/v%
Model	CYLINDER	FLEXIBLE ELLIPTICAL CYLINDER	FLEXIBLE ELLIPTICAL CYLINDER	CYLINDER
Scale	$0.001 \pm 4 \times 10^{-6}$	$135.8 \pm 10.6$	$0.0004 \pm 1 \times 10^{-5}$	$0.0003 \pm 1 \times 10^{-6}$
Background	$0.004 \pm 1.8 \times 10^{-4}$	$0.006 \pm 2 \times 10^{-4}$	$0.007 \pm 1.8 \times 10^{-4}$	$0.005 \pm 2.2 \times 10^{-4}$
Length / Å	$541 \pm 26$	$898 \pm 198$	$738 \pm 47$	$525 \pm 23$
Kuhn Length / Å		$225 \pm 58$	$184 \pm 21$	
Radius / Å	$44 \pm 0.1$	$36 \pm 1.7$	$38 \pm 0.6$	$44 \pm 0.1$
Axis Ratio		$1.7 \pm 0.2$	$1.5 \pm 0.06$	
X <sup>2</sup>	1.52	1.07	1.10	1.33

## Chapter 4

To understand why system C fit best to a flexible elliptical cylinder but system D fit to a cylinder, we decided to fit both data sets to a combined cylinder and flexible elliptical cylinder model (Figure 5) (Table 3). This allowed us to set the parameters as those of the A and B fits respectively and gauge the contribution of each model by fitting the scales.<sup>33</sup> System C produced a scale of  $7.9 \times 10^{-6}$  for the cylinder model and  $6.2 \times 10^{-5}$  for the flexible elliptical model. In contrast, the D hydrogels resulted in a scale of 0.003 and  $1.4 \times 10^{-5}$  for the cylinder and flexible elliptical cylinder models respectively. The variation between the scales suggests that the scattering data corresponding to system D, bears a closer resemblance to that of 2NapFF alone (A) than the pristine UPy samples (B). With this in mind, we hypothesise that the BF-UPy-PEG crosslinker leads to self-sorting of UPy and 2NapFF fibers as two separate networks. We propose that the highly scattering nature of 2NapFF may be dominating the scattering compared to the UPy network.<sup>34</sup> When the crosslinker is removed (system C), the scale values of the combined models are relatively close ( $7.9 \times 10^{-6}$  and  $6.2 \times 10^{-5}$  respectively) with a slightly greater contribution for the flexible elliptical cylinder model. This suggests that without the crosslinking species, the monofunctional UPy-M and 2NapFF undergo coassembly into fibres similar to those of the pristine UPy.

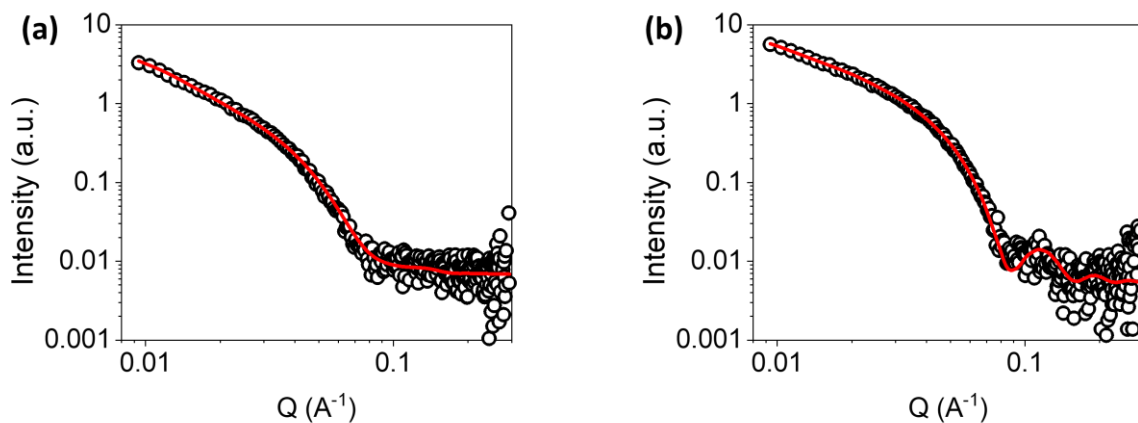


**Figure 5.** Plots of SAXS data (circles) and fits (red solid lines) for **(a)** UPy M 0.25 w/v% 2NapFF 1 w/v% **(b)** UPy B:M =1:80 0.25 w/v% 2NapFF 1w/v% when fitted to a combined cylinder and flexible elliptical cylinder model. For full parameters see Table S2.

## Chapter 4

**Table 3.** Summary of the parameters obtained when UPy M 0.25 w/v% 2NapFF 1 w/v% and UPy B:M =1:80 0.25 w/v% 2NapFF 1w/v% are fitted to a combined cylinder and flexible elliptical cylinder model. In each case, most parameters are fixed and only A Scale (the contribution from the cylinder model) and B Scale (the contribution from the flexible elliptical cylinder model) are fitted. The error of each parameter is stated below each value. Fitting parameters obtained from SasView 5.0.6 model fitting of the SAXS data. The calculated SLD values were 12.177 and 18.140 for systems C and D respectively. The SLD solvent used was 9.469. See section 2.7.3 for full fitting details

	UPy 0.25w/v% 2NapFF 1w/v%	UPy B:M =1:80 2NapFF 1w/v%
Model	CYLINDER + FLEXIBLE ELLIPTICAL CYLINDER	CYLINDER + FLEXIBLE ELLIPTICAL CYLINDER
A Scale	$7.9 \pm 2 \times 10^{-6}$	$0.0003 \pm 4 \times 10^{-6}$
Background	0.005	0.005
A Length / Å	541	541
A Radius / Å	44	44
B Scale	$6.2 \times 10^{-5} \pm 1 \times 10^{-6}$	$1.4 \times 10^{-5} \pm 2.4 \times 10^{-6}$
B Length / Å	898	898
B Kuhn Length / Å	225	225
B Radius / Å	36	36
Axis Ratio	1.7	1.7
X <sup>2</sup>	1.62	1.23

A contrast matching small-angle neutron scattering (SANS) approach was used in attempt to analyse the assembly of the multicomponent systems, by overcoming the dominant scattering from the 2NapFF. This was achieved using a heavily deuterated analogue of 2NapFF (d-2NapFF),<sup>35</sup> to decrease its scattering, allowing us to focus on the scattering from the UPy structures.

## Chapter 4

When fitting the data obtained to the standard cylinder models, we found that the data for the 2NapFF DMEM 1 w/v% hydrogels were fit best to a flexible cylinder model with a power law (Figure 6a). This varies from the SAXS data which fits best to a cylinder model.

However, the radius values calculated for each were similar (i.e. 40 Å from the SANS and 44 Å from the SAXS). While there was little scattering produced by UPy (B:M = 1:80) 0.25 w/v%, the data fit best to an elliptical cylinder model with a power law with a length of 26 Å, axis ratio of 2.6 and a radius minor of 14 Å. (Figure 6d) (Table 4). Once again, this differs from the SAXS data which fit best to a cylinder model with a length of 525 Å and radius of 44 Å. When 2NapFF and UPy-G were combined without the bifunctional crosslinker in system C (UPy M 0.25 w/v%, 2NapFF 1 w/v%), the data were best fit to a hollow cylinder model with a power law (Figure 6b). The radius, thickness and length of the hollow cylinders were found to be 83 Å, 34 Å and 990 Å respectively (Table 4). By using contrast matching to mask the scattering from 2NapFF, we could focus on how the UPy structures assembled. The data fit well to a cylinder model with a power law, with a radius of 44 Å and a length of 180 Å. (Figure 6c) (Table 5). Similarly, when 2NapFF was added to UPy-G with the bifunctional crosslinker in system D (UPy B:M = 1:80 0.25 w/v%, 2NapFF 1 w/v%), the data also fit well to a hollow cylinder model (Figure 5e). The radius and thickness values both resembled those obtained for the system C (UPy M 0.25 w/v%, 2NapFF 1 w/v%) system (36 Å and 83 Å respectively). When the 2NapFF species was deuterated, the data fit to a power law alone (Figure 6f) (Table 5). Once again, it is essential to consider the uniqueness of the chosen SAXS fits as explained in section 2.7.3.

Unfortunately, as both multicomponent systems fit to hollow cylinders according to the SANS, but flexible elliptical cylinders from the SAXS data, it is not possible to draw conclusions on the self-assembly of the systems from this data. However, we can deduce that the variation between the SAXS and SANS data is likely to be an effect of switching from H<sub>2</sub>O to D<sub>2</sub>O. While it is often assumed the deuteration of the solvent has negligible effect on the self-assembly, previous studies have found that this is not always the case.<sup>36</sup>

## Chapter 4

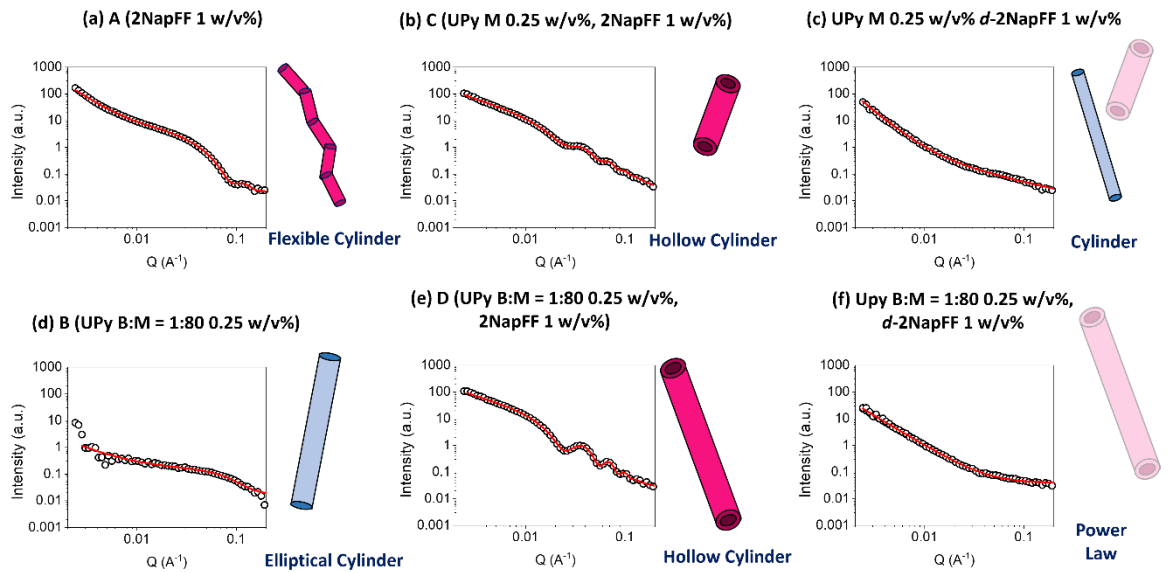


**Figure 6.** Plots of SANS data (circles) and fits (red solid lines) along with cartoon (not to scale) of the structure represented by fit for system (a) A (2NapFF 1 w/v%) (b) C (UPy M 0.25 w/v %, 2NapFF 1 w/v%) (c) UPy M 0.25 w/v, % *d*-2NapFF 1 w/v% (d) B (UPy B:M = 1:80 0.25 w/v %) (e) D (UPy B:M = 1:80 0.25 w/v %, 2NapFF 1 w/v%) (f) UPy B:M = 1:80, 0.25 w/v% *d*-2NapFF 1 w/v%. Full parameters from the fits are listed in Tables 4 and 5.

## Chapter 4

**Table 4.** Summary of the parameters obtained from fitting SANS data collected for each system. Fitting parameters obtained from SasView model fitting of the SANS data. The calculated SLD values were 2.73, 0.673, 1.974, 1.70 for systems A-D respectively. The SLD solvent used was 6.393. See section 2.7.3 for full fitting details. See section 2.7.3 for full fitting details

	2NapFF 1 w/v%		Elliptical cylinder + Power law	UPy B:M =1:80 0.25 w/v%		Hollow cylinder + Power law	UPy M 0.25 w/v% 2NapFF 1 w/v%		UPy B:M =1:80 0.25 w/v% 2NapFF 1 w/v%	
	Value	Error		Value	Error		Value	Error	Value	Error
<b>Scale</b>	1		<b>Scale</b>	1		<b>Scale</b>	1		1	
<b>Background (cm<sup>-1</sup>)</b>	0.013		<b>Background (cm<sup>-1</sup>)</b>	0.0031		<b>Background (cm<sup>-1</sup>)</b>	0.002		0.015	
<b>A scale</b>	5.70e-04	3e-05	<b>A_scale</b>	4.36e-04	3e-04	<b>A scale</b>	4.59e-04	2e-05	7.70e-04	1e-05
<b>A length (Å)</b>	257	20	<b>A length (Å)</b>	26	290	<b>A length (Å)</b>	987	56	1719	130
<b>A Kuhn length (Å)</b>	79	12	<b>Axis ratio</b>	2.60	30	<b>A thickness(Å)</b>	34	1	36	1
<b>A radius (Å)</b>	40	0.3	<b>A radius minor (Å)</b>	14	160	<b>A radius (Å)</b>	83	1	83	0.4
<b>B scale</b>	1.64e-04	2e-05	<b>B scale</b>	9.01e-04	7e-04	<b>B scale</b>	0.0023	7e-05	9.43e-04	6e-04
<b>B power</b>	2.24	0.02	<b>B power</b>	1.14	0.15	<b>B power</b>	1.68	0.008	1.72	0.02
<b><math>\chi^2</math></b>	3.14			1.09		<b><math>\chi^2</math></b>	8.38		3.17	

## Chapter 4

**Table 5.** Summary of the parameters obtained from fitting SANS data collected for *d*-2NapFF samples. Fitting parameters obtained from SasView model fitting of the SANS data. The calculated SLD values were 2.549 and 2.277 respectively. The SLD solvent used was 6.393. See section 2.7.3 for full fitting details. See section 2.7.3 for full fitting details

See section 2.7.3 for full fitting details.

Cylinder + Power law	UPy M 0.25 w/v% <i>d</i> -2NapFF 1 w/v%		Power Law	UPy B:M =1:80 0.25 w/v% <i>d</i> -2NapFF 1 w/v%	
	Value	Error		Value	Error
Scale	1		Scale	4.55e-05	3e-06
Background (cm <sup>-1</sup> )	0.0028		Background (cm <sup>-1</sup> )	0.039	7e-04
A scale	0.0037	6e-05	Power	2.16	0.01
A length (Å)	179	3			
A radius (Å)	44	0.14			
B scale	3.50e-04	1e-05			
B power	2.90	0.03			
$\chi^2$	2.04		$\chi^2$	2.24	

### 4.2.2 Cryogenic Transmission Electron Microscopy (cryo-TEM)

To further investigate the underlying structure of these materials we used cryogenic transmission electron microscopy (cryo-TEM) (Figure 7). All samples produced images displayed long fibrillar structures in agreement with the SAXS and SANS data. Regarding the combined systems, C (Figure 7d) appeared significantly more densely packed compared to the other conditions, making it difficult to analyse individual fibres. From visual inspection, the fibres present in C (Figure 7d) appear longer than in D (Figure 7e) which coordinates with the SAXS data collected (Table 2). As the fibres present in D were less densely packed, we could successfully analyse the dimensions. We found the average radius of the fibrils to be 42 Å, which is consistent with the SAXS data collected (40 Å). The fibre length was calculated as 1000 Å, which is longer than the length suggested by the SAXS

## Chapter 4

data (525 Å). This discrepancy may be due to the fibre length being outside the measurement range of SAXS.

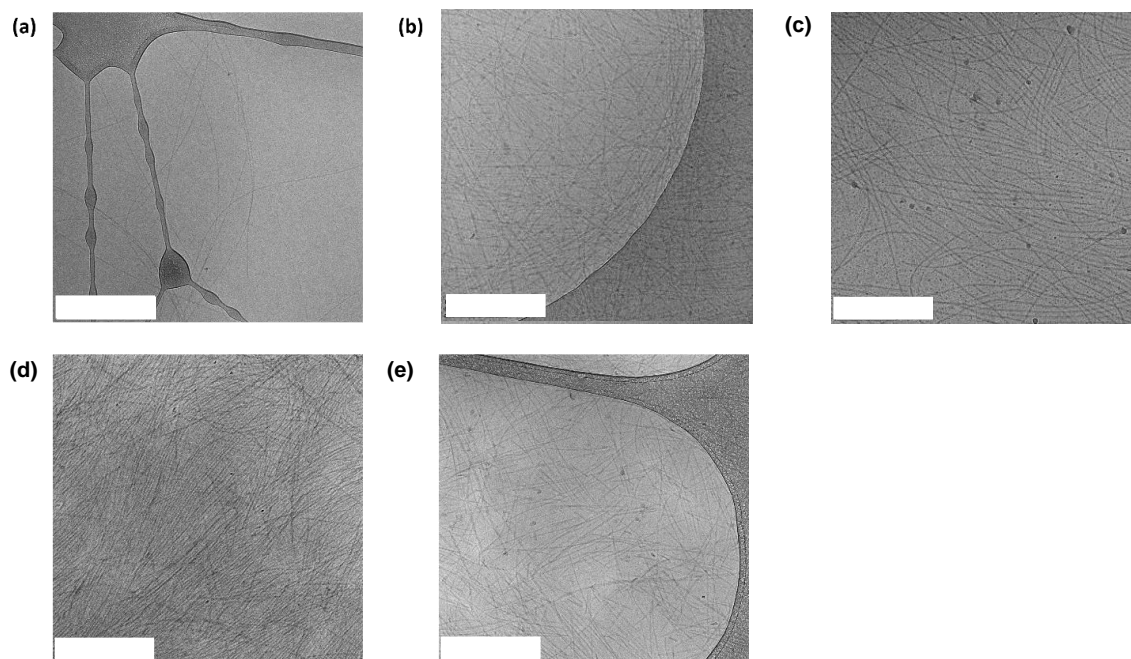


**Figure 7.** Representative cryo-TEM images for (a) A (2NapFF 1 w/v% hydrogel) (b) UPy M 0.25 w/v% (c) B (UPy B:M 1:80 0.25 w/v%) (d) C (UPy M 0.25 w/v%, 2NapFF 1 w/v%) (e) D (UPy B:M 1:80 0.25 w/v%, 2NapFF 1 w/v%). The scale bars represent 500 nm in each case.

### 4.2.3 Rheology and Circular Dichroism

Oscillatory rheology was employed to probe the bulk material properties and examine these systems at larger scales. By doing so, it was discovered that the 2NapFF hydrogels (Figure 8a) and the pristine UPy hydrogel, B (Figure 8b) display significantly different rheological properties. Namely, the storage modulus ( $G'$ ) of the 2NapFF (A) was much higher than the UPy gels. (B) (1300 Pa and 30 Pa respectively). Furthermore, the B system has a crossover point at a strain of 100%, whereas the A samples seem to display a drop in  $G'$  at 0.3% strain, before reaching a plateau. In the frequency sweep data, the 2NapFF media system shows an increase in storage modulus at frequencies exceeding 10 rad/s (Figure 8aii). We believe that this is a consequence of an increase in  $\text{Tan}\delta$  at higher frequencies, causing the inertia of the rheometer itself to dominate over the hydrogel properties. We noticed that frequency

## Chapter 4

sweep data obtained from B displayed larger error bars than the other systems (Figure 8bii) due to the very low values. Moreover, from the corresponding strain sweeps we found that the data points have large errors at strains below 1% (Figure 8bii).

As all the frequency sweeps were carried out at 0.1% strain, we concluded that the noisy data was a result of the low strain and soft material. Regarding the multicomponent systems, C (Figure 8c) produced a slight increase in  $G'$  (5000 Pa) compared to when the bifunctional crosslinker was included in sample D (1200 Pa) (Figure 8d). A possible explanation for this change in stiffness is that the 2NapFF and UPy M fibres are interacting in C, which is disrupted by the addition of the crosslinker, due to UPy M having a higher affinity for BF-UPy-PEG. It may be the case that when the crosslinker is added the UPy B:M 1:80 and 2NapFF form two separate networks, thus D (Figure 8d) may be the sum of both these networks. To test this hypothesis, we used a technique called circular dichroism (CD). This method of absorption spectroscopy is based on the differential absorption of left and right circularly polarized light.<sup>37</sup>

The 2NapFF DMEM and the 2NapFF UPy-G systems display very similar spectra with a peak at 225-230 nm, denoting the  $\pi$ - $\pi$  stacking of the phenyl groups present in 2NapFF (Figure 9a and b). The high-tension (HT) voltage (Figure 9c) confirms that enough photons reached the detector to produce a valid signal. If the voltage detected was above the threshold of 700 V, the measurement could not be considered accurate as not enough light was reaching the detector. As the voltage detected was below the limit we can assume that our CD data collected is reliable.

Upon the addition of the crosslinker, the spectrum changed greatly. To confirm that the change in the spectra is a consequence of a change in self-assembly of 2NapFF and UPy M when BF-UPy-PEG is introduced, BF-UPy-PEG alone was also investigated. The crosslinker alone did not produce any signal which confirmed our theory. This self-sorting is consistent with the SAXS data obtained for the system. Alternatively, due to the higher storage modulus of 2NapFF, it may be the only component being measured, with the UPy having little or no influence. This hypothesis is reinforced by the similarities in the  $G'$  of A (Figure 8a) and D (Figure 8d).

## Chapter 4

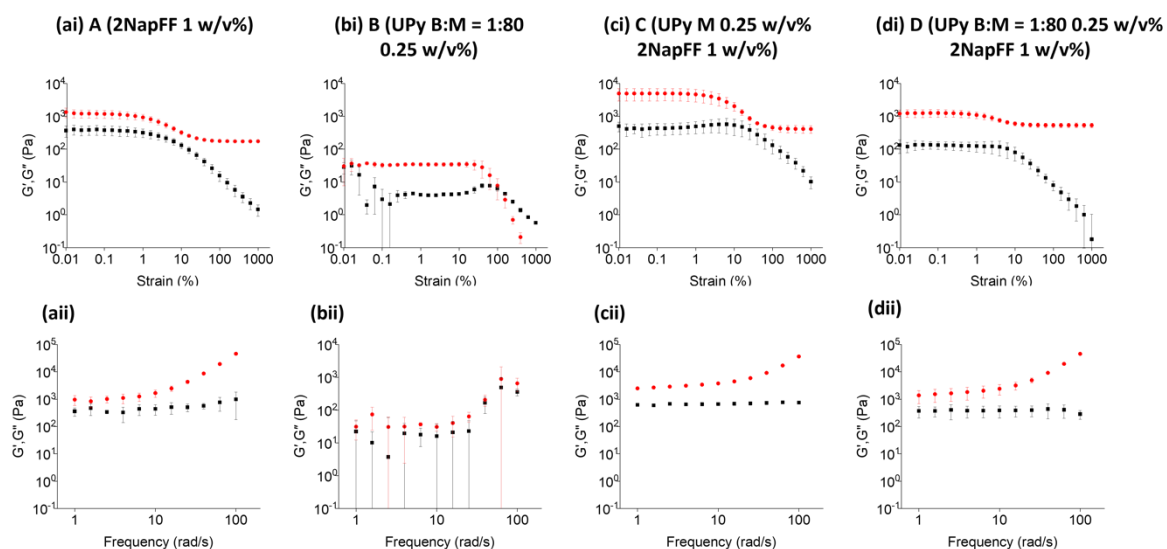


**Figure 8.** (ai-di) Strain sweeps of four systems investigated. In each case  $G'$  data is red and the storage modulus ( $G''$ ) is black. (aii-dii) Frequency sweeps of four systems investigated. In each case  $G'$  data is red and the storage modulus ( $G''$ ) is black. Error bars are representative of the standard deviation between triplicates where one sample was used per measurement.

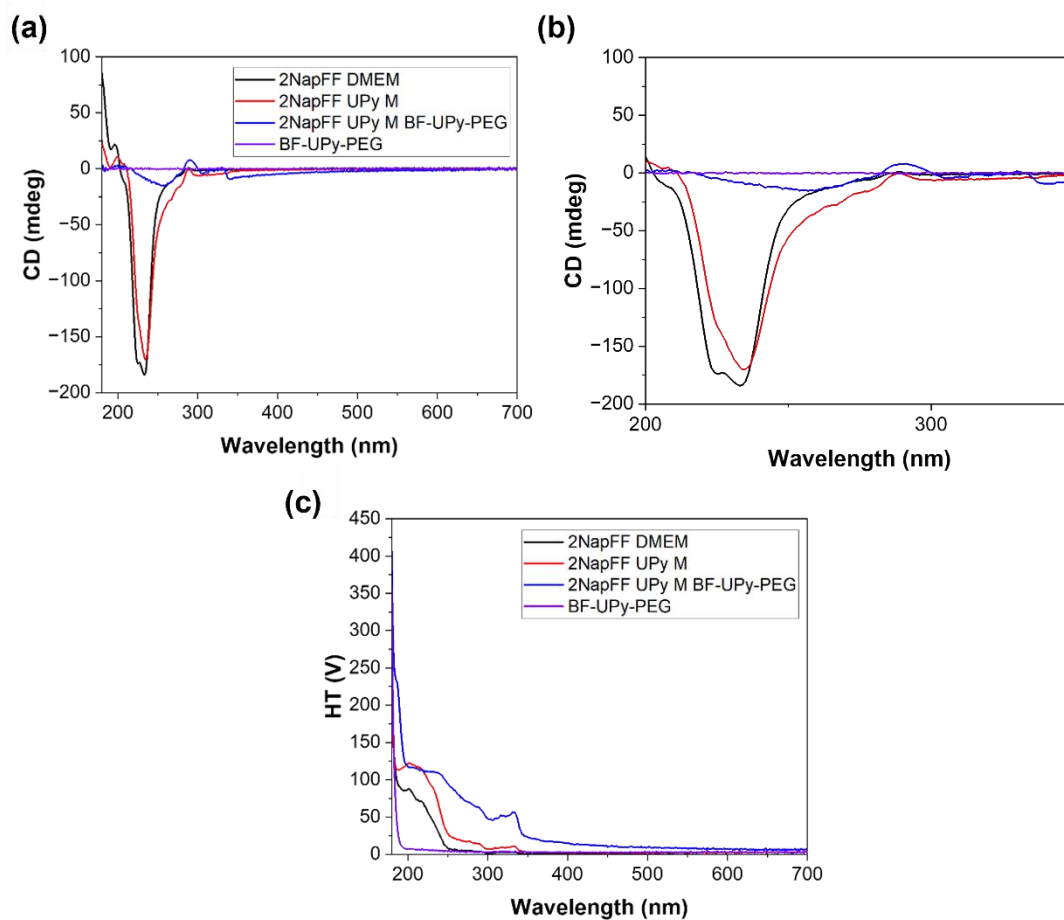


**Figure 9.** (a) Full CD spectra (b) CD spectra zoomed from 200-250 nm and (c) HT (high tension) spectra recorded for systems A, C, D and BF-UPy-PEG alone.

### 4.2.4 Cell Culture Studies

To access the biocompatibility of these systems, we used them to carry out 2D fibroblast culture. Fibroblasts were chosen for this study as they are the main cellular component of connective tissue and produce several ECM proteins including collagen.<sup>38</sup> Therefore, we hoped that by exposing them to the hydrogels we could gain valuable insight into how the systems interact with the ECM.

As previously alluded to, 1 mM UPy-cRGD was incorporated into the UPy-G mixtures, both with and without the crosslinker to enhance cell adhesion. Once seeded, the cells were incubated overnight, before staining and imaging the following morning. We opted for an immunostaining approach to allow us to study the morphology of the cells and determine if the scaffold is supportive. For example, if a live/dead assay was used, the round cells might stain as live cells, although the material does not support their spreading. Likewise, SEM would not offer representative images of the systems as the process requires drying of the samples, which leads to morphological changes in such materials.<sup>39</sup>

It was found that the cells cultured on the 2NapFF hydrogels (A) showed little sign of cell spreading and displayed a round morphology (Figure 10a). In contrast, fibroblasts cultured on the UPy only hydrogels (B) adhered effectively and showed clear indications of cell spreading (Figure 10b). We attributed the difference in cell behaviour and morphology to the presence of UPy-cRGD in the UPy system, while the 2NapFF gels lack any bioactive species. Regarding the mixed systems, we observed that only a few cells adhered to the C hydrogels, and those that did display a round morphology. Conversely, cells cultured on the D samples (Figure 10d) seem to exhibit morphology closer to those cultured on UPy alone B gels (Figure 10a). Based on these results, we hypothesise that the UPy-G fibres require the bifunctional UPy-PEG molecule to form a network. This is supported by the fact that pristine UPy-G assemblies are solutions and do not form hydrogels without a crosslinker.<sup>3</sup>

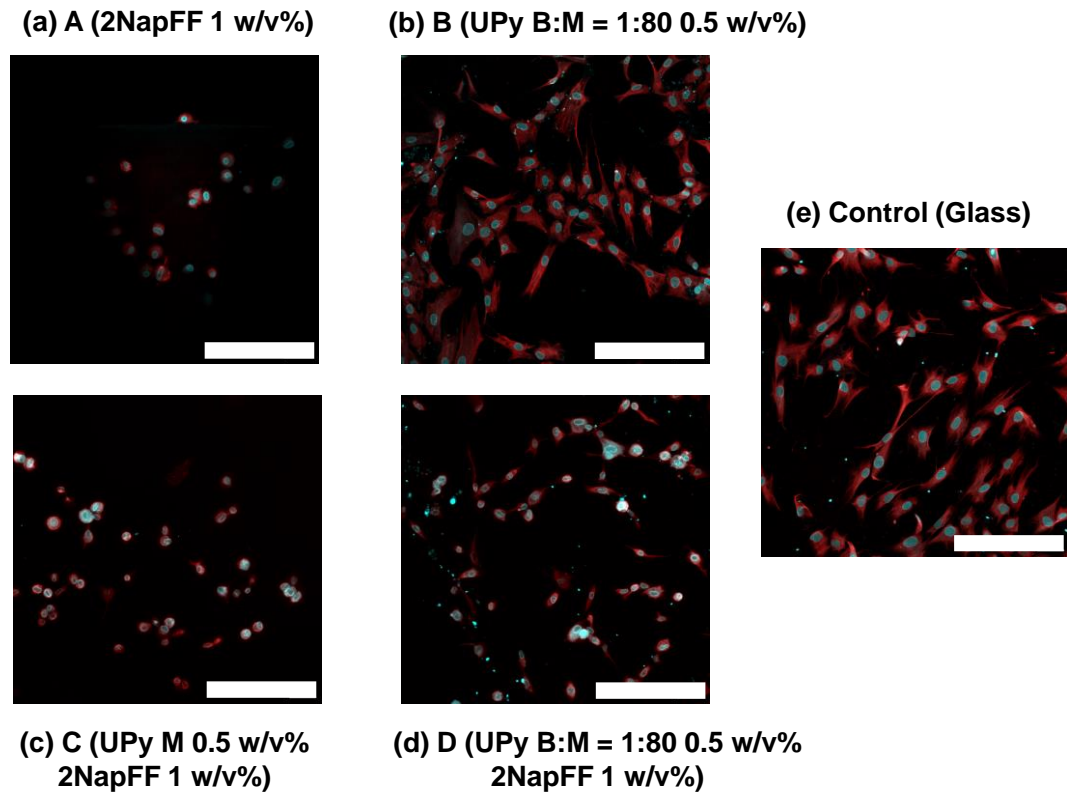


**Figure 10.** Images of hNDFs 24 hours after seeding on the surface of the hydrogels and stained for nuclei (blue) and actin (red). The cells were seeded on **(a)** A (2NapFF 1 w/v%) **(b)** B (UPy B:M=1:80 0.5 w/v%) **(c)** C (UPy M 0.5 w/v%, 2NapFF 1 w/v%) **(d)** D (UPy B:M = 1:80 0.5 w/v%, 2NapFF 1 w/v%) **(e)** glass tissue culture plate. For each sample including the UPy-G monomer, 1 mM UPy-cRGD was also included to enhance cell adhesion. Images were collected using a Leica TCS SP8 X confocal microscope (Leica Microsystems) using 20x objective. Images were processed in ImageJ to create max-projection images of the original z-stacks. Scale bar represents 200  $\mu\text{m}$  in each case.

### 4.3 Conclusions

In this chapter, we have described how two different supramolecular systems interact across multiple length scales. Using SAXS allowed us to probe the nanoscale structures present in the systems and deduce that C fits to a flexible elliptical cylinder model with parameters like that of the pristine UPy samples (B). From this, we were able to conclude that the UPy component is driving the self-assembly of these samples, with little contribution from the 2NapFF. Moreover, when the bifunctional crosslinker BF-UPy-PEG was incorporated, D fit best to a cylinder model with parameters within error of those obtained from the 2NapFF 1 w/v% hydrogels. We theorised that these results point towards the formation of two separate networks, with the 2NapFF network dominating the scattering. This hypothesis was supported by CD and rheology data which imply that when BF-UPy-PEG is added to the UPy M and 2NapFF system, two separate networks are formed at a bulk scale. Finally, we investigated the biocompatibility of these materials by performing 2D fibroblast culture. The images collected showed that BF-UPy-PEG is crucial for crosslinking UPy-Gly fibers and thus forming a network to which cells can adhere.

Our results reiterate that a change of assembly occurs in the presence of the crosslinker and highlights how understanding such processes can enhance bioactivity. While further optimisation is required for cell culture applications, our work reinforces the importance of thorough characterisation of materials. Such characterisation will help us understand and develop finely controllable novel biomaterials in the future.

## 4.4 References

1. R. Dong, Y. Pang, Y. Su and X. Zhu, *Biomater. Sci.*, 2015, **3**, 937-954.
2. J. Omar, D. Ponsford, C. A. Dreiss, T.-C. Lee and X. J. Loh, *Chem. Asian J.*, 2022, **17**, e202200081.
3. M. Diba, S. Spaans, S. I. S. Hendrikse, M. M. C. Bastings, M. J. G. Schotman, J. F. van Sprang, D. J. Wu, F. J. M. Hoeben, H. M. Janssen and P. Y. W. Dankers, *Adv. Mater.*, 2021, **33**, e2008111.
4. J. E. Scott, *J. Anat.*, 1995, **187 ( Pt 2)**, 259-269.
5. P. Y. Dankers, T. M. Hermans, T. W. Baughman, Y. Kamikawa, R. E. Kieltyka, M. M. Bastings, H. M. Janssen, N. A. Sommerdijk, A. Larsen, M. J. van Luyn, A. W. Bosman, E. R. Popa, G. Fytas and E. W. Meijer, *Adv. Mater.*, 2012, **24**, 2703-2709.
6. M. M. Bastings, S. Koudstaal, R. E. Kieltyka, Y. Nakano, A. C. Pape, D. A. Feyen, F. J. van Slochteren, P. A. Doevendans, J. P. Sluijter, E. W. Meijer, S. A. Chamuleau and P. Y. Dankers, *Adv. Healthc. Mater.*, 2014, **3**, 70-78.
7. P. Y. Dankers, M. J. van Luyn, A. Huizinga-van der Vlag, G. M. van Gemert, A. H. Petersen, E. W. Meijer, H. M. Janssen, A. W. Bosman and E. R. Popa, *Biomaterials*, 2012, **33**, 5144-5155.
8. F. H. Beijer, R. P. Sijbesma, H. Kooijman, A. L. Spek and E. W. Meijer, *J. Am. Chem. Soc.*, 1998, **120**, 6761-6769.
9. R. P. Sijbesma, F. H. Beijer, L. Brunsveld, B. J. Folmer, J. H. Hirschberg, R. F. Lange, J. K. Lowe and E. W. Meijer, *Science*, 1997, **278**, 1601-1604.
10. M. M. C. Bastings, S. Koudstaal, R. E. Kieltyka, Y. Nakano, A. C. H. Pape, D. A. M. Feyen, F. J. van Slochteren, P. A. Doevendans, J. P. G. Sluijter, E. W. Meijer, S. A. J. Chamuleau and P. Y. W. Dankers, *Adv. Healthc. Mater.*, 2014, **3**, 70-78.
11. L. Rijns, J. W. Peeters, S. I. S. Hendrikse, M. E. J. Vleugels, X. Lou, H. M. Janssen, E. W. Meijer and P. Y. W. Dankers, *Chem. Mater.*, 2023, **35**, 8203–8217
12. L. Rijns, M. J. Hagelaars, J. J. B. van der Tol, S. Loerakker, C. V. C. Bouten and P. Y. W. Dankers, *Adv. Mater.*, 2300873.
13. D. M. Raymond, B. L. Abraham, T. Fujita, M. J. Watrous, E. S. Toriki, T. Takano and B. L. Nilsson, *ACS Appl. Bio. Mater.*, 2019, **2**, 2116-2124.
14. D. K. Smith, *Soft Matter*, 2024, **20**, 10-70.
15. S. Fleming and R. V. Ulijn, *Chem. Soc. Rev.*, 2014, **43**, 8150-8177.
16. X. Du, J. Zhou, J. Shi and B. Xu, *Chem. Rev.*, 2015, **115**, 13165-13307.

## Chapter 4

17. K. Tao, A. Levin, L. Adler-Abramovich and E. Gazit, *Chem. Soc. Rev.*, 2016, **45**, 3935-3953.
18. Z. Yang, L. Wang, J. Wang, P. Gao and B. Xu, *J. Mater. Chem.*, 2010, **20**, 2128-2132.
19. E. R. Draper and D. J. Adams, *Chem*, 2017, **3**, 390-410.
20. E. R. Draper, B. Dietrich, K. McAulay, C. Brasnett, H. Abdizadeh, I. Patmanidis, S. J. Marrink, H. Su, H. Cui, R. Schweins, A. Seddon and D. J. Adams, *Matter*, 2020, **2**, 764-778.
21. L. Chen, G. Pont, K. Morris, G. Lotze, A. Squires, L. C. Serpell and D. J. Adams, *Chem. Comm.*, 2011, **47**, 12071-12073.
22. Y. M. Abul-Haija, S. Roy, P. W. Frederix, N. Javid, V. Jayawarna and R. V. Ulijn, *Small*, 2014, **10**, 973-979.
23. V. Jayawarna, S. M. Richardson, A. R. Hirst, N. W. Hodson, A. Saiani, J. E. Gough and R. V. Ulijn, *Acta Biomater.*, 2009, **5**, 934-943.
24. L. J. Marshall, S. Bianco, R. E. Ginesi, J. Dutch, E. R. Draper and D. J. Adams, *Soft Matter*, 2023, **19**, 4972-4981.
25. E. V. Alakpa, V. Jayawarna, K. E. V. Burgess, C. C. West, B. Péault, R. V. Ulijn and M. J. Dalby, *Sci. Rep.*, 2017, **7**, 6895.
26. L. Li, R. Sun and R. Zheng, *Mater. Des.*, 2021, **197**, 109209.
27. E. R. Draper and D. J. Adams, *Chem. Soc. Rev.*, 2018, **47**, 3395-3405.
28. B. Adelizzi, N. J. Van Zee, L. N. J. de Windt, A. R. A. Palmans and E. W. Meijer, *J Am. Chem. Soc.*, 2019, **141**, 6110-6121.
29. P. Makam and E. Gazit, *Chem. Soc. Rev.*, 2018, **47**, 3406-3420.
30. Y. L. Wang, S. P. Lin, S. R. Nelli, F. K. Zhan, H. Cheng, T. S. Lai, M. Y. Yeh, H. C. Lin and S. C. Hung, *Macromol. Biosci.*, 2017, **17**, 1600192.
31. E.V. Alakpa, V. Jayawarna, A. Lampel, K. V. Burgess, C. C. West, S. C. J. Bakker, S. Roy, N. Javid, S. Fleming, D. A. Lamprou, J. Yang, A. Miller, A. J. Urquhart, P. W. J. M. Frederix, N. T. Hunt, B. Péault, R. V. Ulijn and M. J. Dalby, *Chem*, 2016, **1**, 298-319.
32. A. F. Vrethen, J. F. van Sprang, M. J. G. Schotman and P. Y. W. Dankers, *Mater. Today Bio*, 2024, **26**, 101021.
33. D. McDowall, B. J. Greeves, R. Clowes, K. McAulay, A. M. Fuentes-Caparrós, L. Thomson, N. Khunti, N. Cowieson, M. C. Nolan, M. Wallace, A. I. Cooper, E. R. Draper, A. J. Cowan and D. J. Adams, *Adv. Energy Mater.*, 2020, **10**, 2002469.

#### Chapter 4

34. K. L. Morris, L. Chen, J. Raeburn, O. R. Sellick, P. Cotanda, A. Paul, P. C. Griffiths, S. M. King, R. K. O'Reilly, L. C. Serpell and D. J. Adams, *Nat. Commun.*, 2013, **4**, 1480.
35. L. J. Marshall, M. Wallace, N. Mahmoudi, G. Ciccone, C. Wilson, M. Vassalli and D. J. Adams, *Adv. Mater.*, 2023, **35**, 2211277.
36. K. McAulay, H. Wang, A. M. Fuentes-Caparrós, L. Thomson, N. Khunti, N. Cowieson, H. Cui, A. Seddon and D. J. Adams, *Langmuir*, 2020, **36**, 8626-8631.
37. R. P. Gregory and S. Raps, *Biochem. J.*, 1974, **142**, 193-201.
38. C. Wiegand and U.C. Hipler, *Skin Pharmacol Physiol.*, 2009; **22** :74-82.
39. L. L. Mears, E. R. Draper, A. M. Castilla, H. Su, B. Dietrich, M. C. Nolan, G. N. Smith, J. Douth, S. Rogers and R. Akhtar, *Biomacromolecules*, 2017, **18**, 3531-3540.

## **Chapter 5: 3D Printing of 2NapFF Media Hydrogels**

C.Wallace was responsible for synthesis of 2NapFF, collection of rheological data and carrying out cell work. Preparation of r small-angle x-ray scattering (SAXS) samples and collection of SAXS data was carried out by C. Wallace and S. Bianco, L. Marshall and M. Hill (University of Glasgow). Processing of SAXS data was carried out by A. Sutherland (Diamond Light Source) and fitted by C. Wallace. D. Adams conceptualised and supervised the project.

### 5.1 Introduction

Since its introduction, 3D printing technology has steadily increased its impact on society and is transforming the science and engineering of advanced materials.<sup>1,2</sup> One sector which has benefited from these advancements is the rapidly growing field of bioprinting. This technique involves exploiting the progression of 3D printing technology, to print materials that incorporate viable cells for applications in areas such as tissue engineering and biomedicine.<sup>3-5</sup> In fact, in recent years bioprinting has allowed for the construction of a number of tissues including multilayered skin,<sup>6</sup> bones,<sup>7</sup> muscle structures,<sup>8</sup> and retinal tissue.<sup>9</sup>

Extrusion-based, inkjet-based and laser-assisted bioprinting are three of the most common bioprinting methods used today (Figure 1). The ease of use and low application cost of extrusion-based bioprinting have made it the most widely employed variation.<sup>10</sup> Firstly, the bioink is loaded into a syringe or cartridge, before being mechanically extruded onto a platform.<sup>11</sup> Despite the popularity of extrusion-based printing, applications may be limited by its low printing resolution and high rate of cell death due to the shear stress experienced by the cells when extruded through the nozzle or needle.<sup>12</sup> Another bioprinting technique is inkjet-based printing, which enables non-contact printing by dispensing droplets of dilute solutions using thermal or piezoelectric processes.<sup>13</sup> While this method is generally fast, accurate and low-cost, it requires low-viscosity bioinks and the heating effects can cause damage to cells.<sup>14</sup> Finally, laser-assisted bioprinting uses a laser as the energy source to deposit bioink onto a substrate. The process requires a pulsed laser source, an energy-absorbing layer coated in the bioink and a donor slide. Essentially, the laser pulses cause the formation of a cavitation-like bubble within the bioink. The bubble expands until it bursts, leading to the creation of a jet which transfers the bioink onto the substrate as microdroplets.<sup>15</sup> Although laser-assisted bioprinting offers several advantages, such as the ability to print high cell densities with high viability, we must also consider the high cost of the equipment required and the time-consuming nature of the setup needed (i.e. loading the bioink onto the energy-absorbing layer).<sup>16</sup>

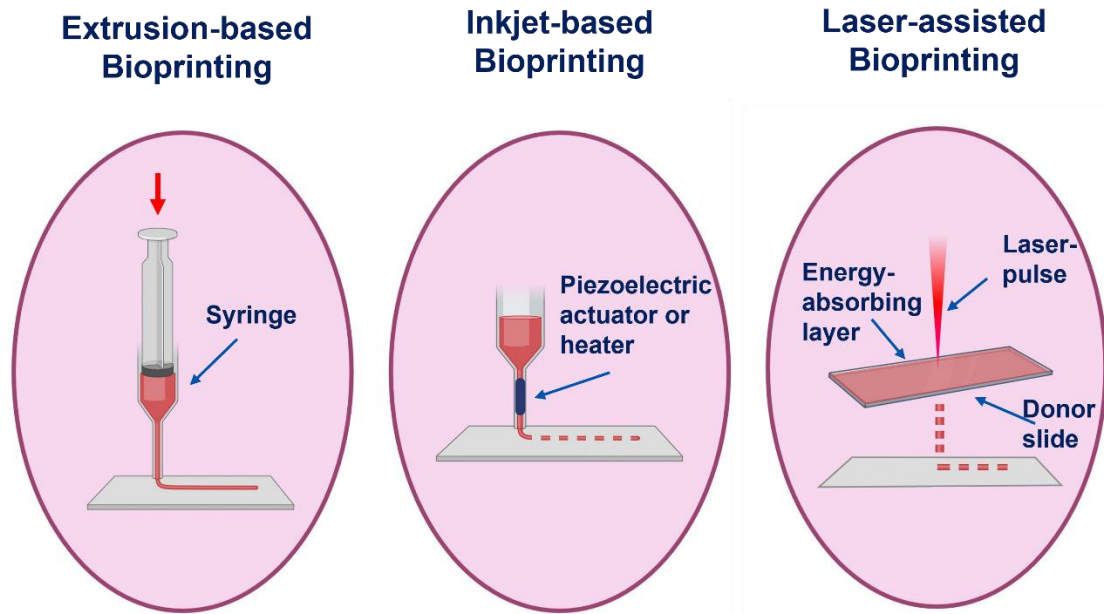


**Figure 1.** Schematic of different bioprinting variations.

Another important factor to consider when fabricating materials via bioprinting is the bioink used. Bioinks usually comprise living cells, a support material and biological additives such as matrix and signalling molecules (Figure 2).<sup>17, 18</sup> Hydrogels are the most common support material used when designing potential bioinks for printing, due to their high water content, and ability to mimic the extracellular matrix.<sup>19, 20</sup> While natural hydrogels are commonly used for such applications, they often lack the mechanical strength and shape fidelity required for printing.<sup>16</sup> Synthetic polymers possess several characteristics that make them appealing candidates for bioinks, including the ability to fine-tune their mechanical and physiochemical properties.<sup>21</sup> However, issues may arise due to their low printing resolution and limited load-bearing capacity.<sup>22</sup> Low molecular weight gelators (LMWG) or supramolecular gelators are less commonly employed for bioprinting purposes. These molecules self-assemble via non-covalent interactions resulting in anisotropic structures that form a network capable of immobilizing a solvent.<sup>23, 24</sup> LMWGs present a compelling alternative to natural hydrogels for these applications because of their unique properties. For example, these gelators have the optimal viscoelasticity required for cell culture and consume minimal materials making them efficient and practical alternatives for bioprinting.<sup>16</sup>

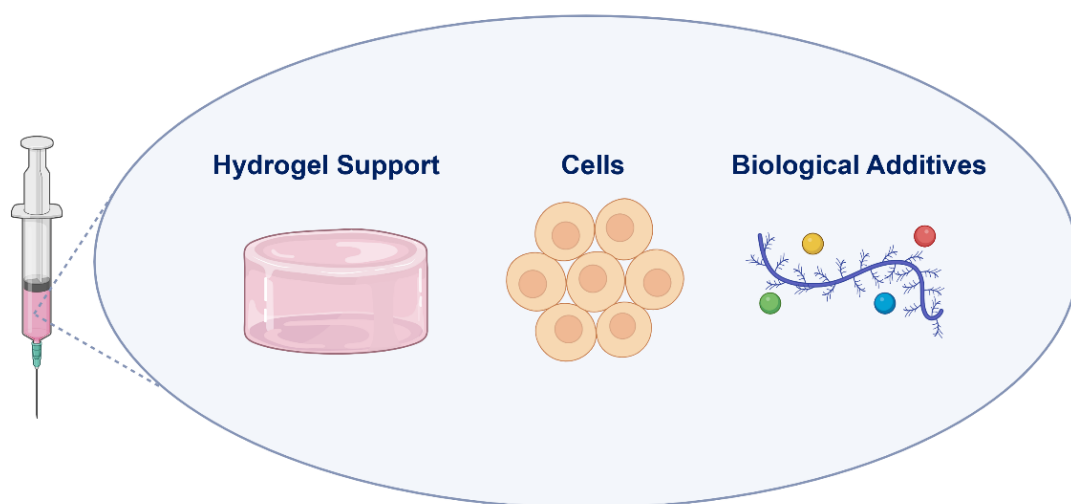


**Figure 2.** Cartoon displaying components which constitute a bioink.

A plethora of peptide-based LMWG have previously been used for cell culture and 3D bioprinting applications.<sup>25-29</sup> For example, the work of Rauf et al. illustrates the ability of tetra peptides IVZK and IVFK (Figure 3a and b) to coextrude with mesenchymal stem cell and fibroblast cell lines, producing a mesh scaffold.<sup>30</sup> Previously, our group has highlighted the 3D printing potential of dipeptide gelators including Fmoc-FF (Figure 3c).<sup>31,32</sup> However, the solvent switch and pH gelation triggers needed rendered them unsuitable for biological applications. In this chapter, we attempt to combat these issues using the 2NapFF media hydrogels at physiological pH, as discussed throughout this thesis. We also utilise these systems to investigate the effect different culture media have on the gelation process and the properties of the resulting hydrogels at varying length scales via rheology and small-angle scattering. Finally, we compare the printing properties of the systems and evaluate their biocompatibility by using them to print macrophage-containing structures.

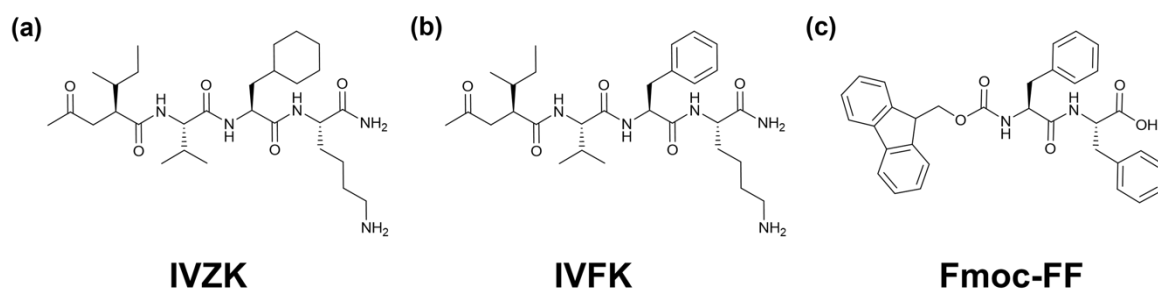


**Figure 3.** Chemical structure of peptide gelators which have been 3D printed in the literature where the letters are abbreviations of the amino acids present. (a) IVZK represents an isoleucine, valine, glutamine, lysine tetrapeptide (b) IVFK is an isoleucine, valine, phenylalanine, lysine tetrapeptide (c) Fmoc-FF is a diphenylalanine protected by an Fmoc group at the *N*-terminus.<sup>30 31, 32</sup>

## 5.2 Results and Discussion

Testing the rheological properties of potential bioinks is essential as they directly impact the fidelity of the printed structure and the viability of cells. Some rheological properties influencing the final 3D printed materials include viscosity, viscoelasticity and shear thinning behaviour.<sup>33</sup> It is crucial to evaluate the viscosity of the hydrogels as higher viscosities enhance structural stability but reduce cell viability. On the other hand, lower viscosity decreases structural stability but improves cell viability, thus a balance of structural integrity and biocompatibility is required.<sup>10, 34</sup> Viscoelasticity refers to the behaviour of materials with both elastic and viscous properties when deformed.<sup>35</sup> The elastic component is denoted by the storage modulus ( $G'$ ) and viscous by the loss modulus ( $G''$ ). These factors impact the printability of a material with a higher storage modulus leading to a higher structural stability.<sup>36</sup> Lastly, the shear thinning behaviour of the material should also be evaluated. This refers to the decrease in viscosity observed when shear stress is applied.<sup>37</sup> It is also important to note that high shear rates are not ideal for bioprinting as they lead to an increase in cell death.<sup>10</sup>

To evaluate the potential of 2NapFF media hydrogels for bioprinting, we began by probing the effect of using different media to carry out the gelation. This involved carrying out the gelation procedure as previously described in Chapter 2, using 1 mL of various media. The seven media investigated were DMEM, DMEM + glucose, DMEM F12, RPMI, IDIM, HPLM and Medium 199. The 2NapFF (20 mg/mL) solution at pH 7 was combined with an equal volume of media before being transferred into a 3D-printed plastic square-shaped moulds ( $19.5 \times 19.5 \times 5$  mm) adhered to a borosilicate glass microscope slide. After being left overnight, each 2NapFF/media combination formed a self-supporting structure. Oscillatory rheology was then carried out using a 12.5 mm parallel plate (Figure 4a). Using the 3D printed holder set-up was necessary to compare to printed samples later. Overall, the strain sweep data obtained for most of the hydrogels were very similar. Contrastingly, the hydrogels formed from DMEM + glucose (Figure 4c) and RPMI (Figure 4e) had a higher  $G'$ , suggesting a stiffer network. The strain sweeps obtained from these samples were also very similar with both hydrogels exhibiting an increase in  $\tan \delta$  compared to the other samples (i.e. there is less of a difference between  $G'$  and  $G''$ ). This indicates that when 2NapFF is gelled with DMEM + glucose and RPMI the structures formed are more “liquid-like” than the hydrogels produced from the other media despite having a higher stiffness.

## Chapter 5

Regarding the frequency sweep data (Figure 5), we found moduli for all samples to be frequency-independent except for IDIM and HPLM which became frequency-dependent at high frequencies (Figure 5e and f).

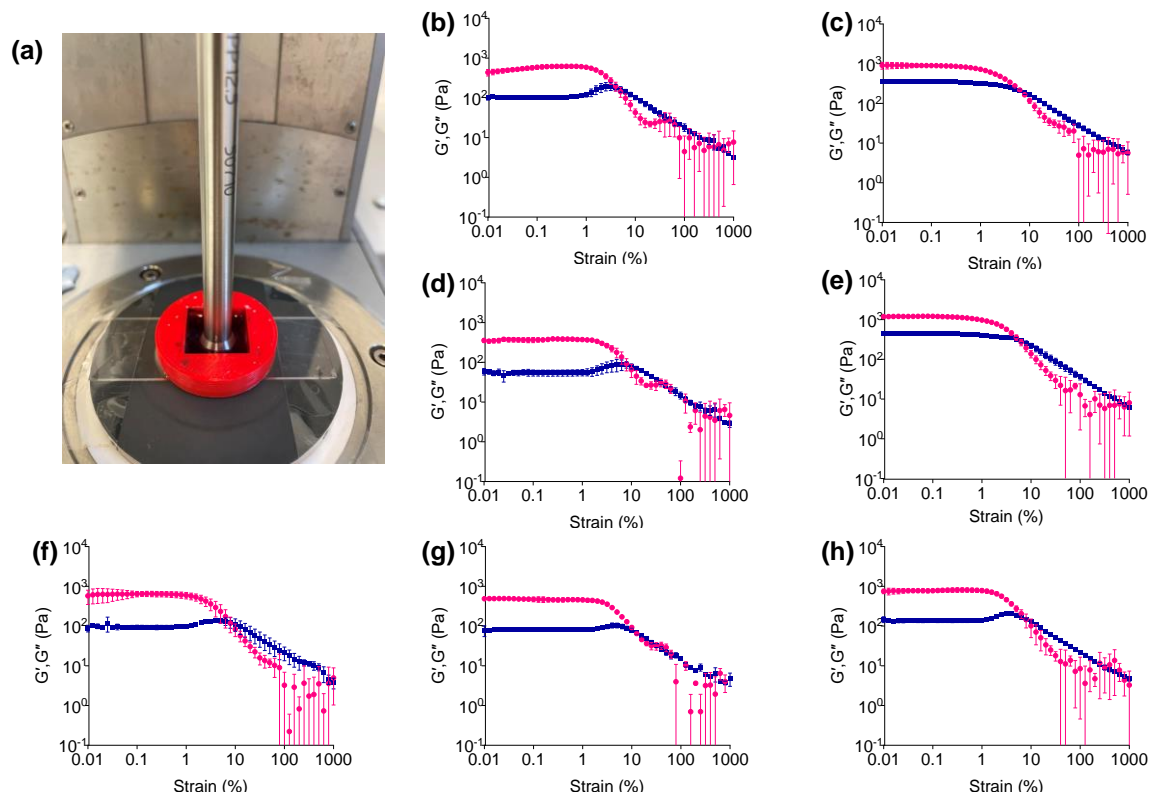


**Figure 4.** (a) Setup used to measure gels formed in custom 3D printed moulds attached to borosilicate glass slides using parallel plate (12.5 mm) geometry. Strain sweeps carried out on 2 mL 2NapFF gels formed in mould with (b) DMEM (c) DMEM + glucose (d) DMEM F12 (e) RPMI (f) IDIM (g) HPLM (h) Medium 199. In each case, the pink data represent  $G'$  and the black data represent  $G''$ . Error bars are representative of the standard deviation between triplicates, where one sample was used per measurement.

## Chapter 5

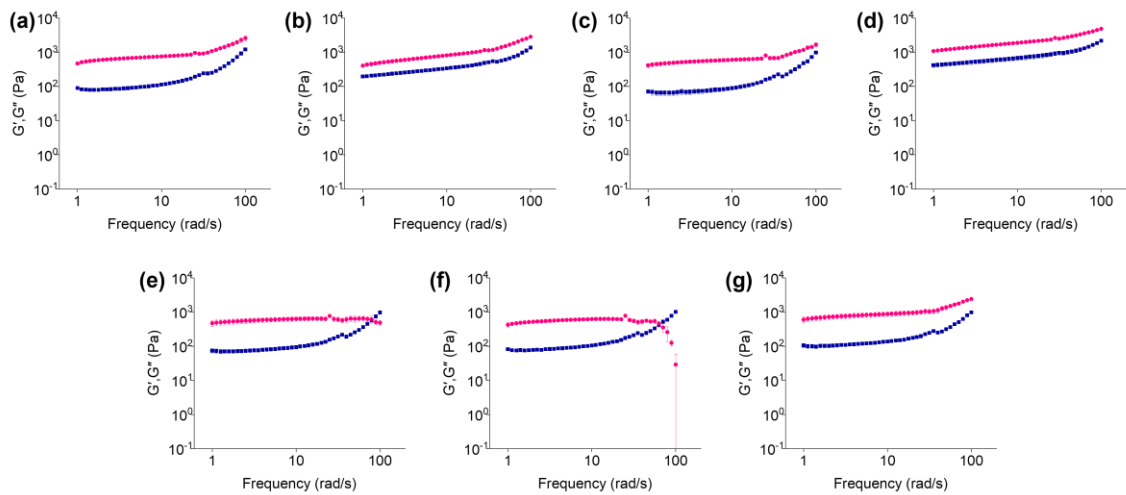


**Figure 5.** Frequency sweeps carried out on 2 mL 2NapFF gels formed in mould with (a) DMEM (b) DMEM + glucose (c) DMEM F12 (d) RPMI (e) IDIM (f) HPLM (g) Medium 199. In each case, the pink data represent  $G'$  and the black data represent  $G''$ . Error bars are representative of the standard deviation between triplicates. One gel sample was used per measurement.

### 4.2.1 Optimisation of 3D printing parameters

Preliminary testing to evaluate the potential of the hydrogels for printing involved using an extrusion-based 3D printer to print 5 cm lines of 2NapFF with different media. The samples were prepared as previously described but taking the pre-gel solution up with a 3 mL syringe, the nozzle of which was then covered in parafilm and left overnight (Figure 6). Before printing the syringes were equipped with a 23G needle (with a diameter of 0.6 mm) cut to 3 mm to print the thinnest lines possible to mimic the bioprinting process.

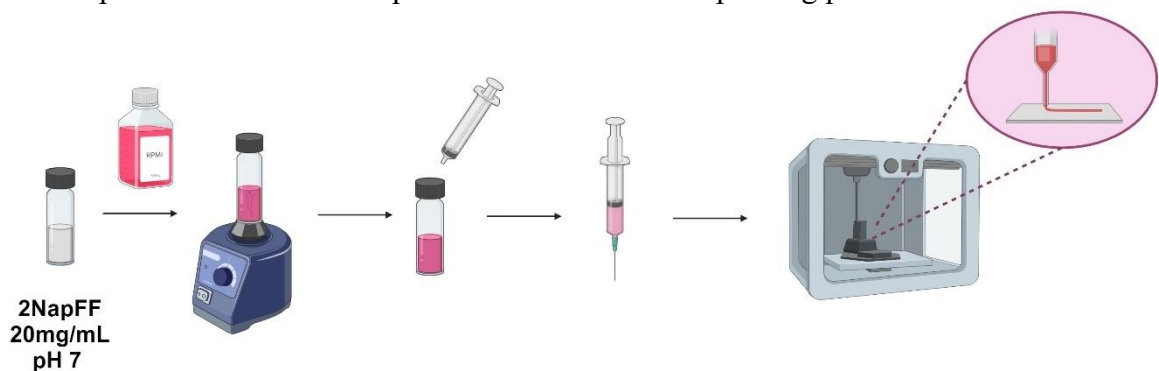


**Figure 6.** Cartoon depicting sample preparation for printing hydrogels. To a solution of 20 mg/mL 2NapFF pH 7, an equal volume of cell culture media was added. The resulting solution was vortexed for 5 seconds. The pre-gel solution was then taken up by a 3 mL syringe after and the nozzle was covered with parafilm, before being left overnight. The following morning the samples were printed.

## Chapter 5

Several parameters were varied to optimise the printing process including the volume and speed of extrusion.<sup>31</sup> Gaining fine control over these properties allowed us to control the shear rate at which the hydrogel is extruded from the syringe nozzle as shown in Equation 1. This equation demonstrates how the shear rate ( $\gamma$  in  $s^{-1}$ ), of a non-Newtonian fluid relates to the volume of the extruded gel ( $V$  in  $m^3$ ), the radius of the needle ( $r$  in  $m$ ), and the time taken to extrude the volume of the gel ( $t$  in  $s$ ). This equation was used to calculate the shear rate of extrusion for the samples using parameters set by the 3D printer (Figure 7a).

$$\text{Shear rate, } \gamma = \frac{4V}{\pi r^3 t} \quad \text{(Equation 1)}$$

Initially, each hydrogel was printed at varying shear rates of 500, 750, 1000, 1500, 3000, 5000, 7000 and 10,000  $s^{-1}$  (Figure 7c). The shear rate which printed the smoothest and most continuous line was then used to print lines with varying extrusion rates. Finally, once the optimal extrusion and shear rate was chosen the height of the needle from the print bed was changed. In each case, the set of parameters resulting in the thinnest, continuous printed 50 mm line was considered the optimum conditions (Figure 7d-j).

Interestingly, the same optimal parameters for all samples were found to be a shear rate of 1000  $s^{-1}$ , extrusion speed of 4  $\mu L \text{ mm}^{-1}$  and a needle height of 3 mm above the surface. The hydrogels formed with Medium 199 were the only samples not capable of printing a continuous line (Figure 7k). This finding may indicate that the culture media has little to no effect on the printing properties of the hydrogels formed. The results are also interesting considering the variation in rheological properties of the 2NapFF/RPMI and 2NapFF/RPMI DMEM + glucose hydrogels in comparison to the others.

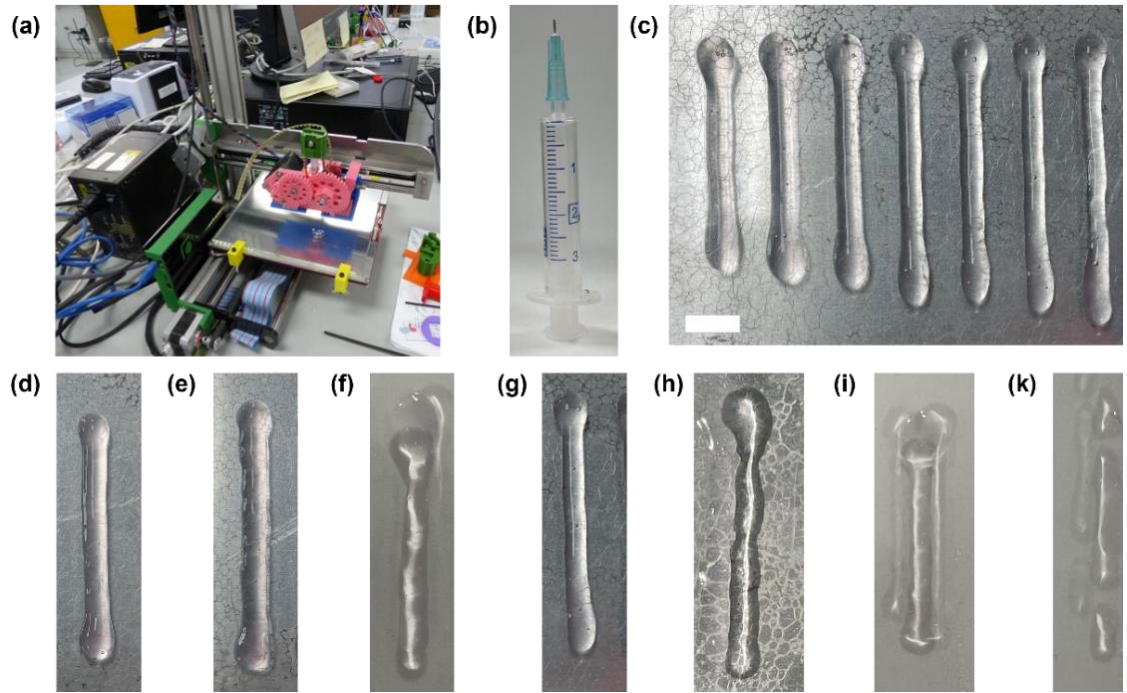


**Figure 7.** (a) Photograph of the custom-made 3D printer used. (b) 3 mL syringe with 3 mm 23G needle attached for printing (c) 2NapFF RPMI hydrogels printed at various shear rates for optimisation. Scale bar represents 1 cm. (d-k) 2NapFF hydrogels gelled with DMEM, DMEM + glucose, DMEM, F12, RPMI, IDIM, HPLM and medium 199 respectively printed at optimised conditions for each sample.

When considering potential bioinks, it is common to focus on the rheological properties of the materials before printing due to the challenges posed by measuring the printed samples.<sup>38, 39</sup> Previous work from our group has suggested a possible technique to overcome this by printing the hydrogels into the moulds used to measure the pre-printing samples in a serpentine fashion, before measuring with the 12.5 mm parallel plate.<sup>32</sup> Unfortunately, the shear thinning effect of printing led to samples that were more “liquid-like” than the non-printed samples. Numerous samples were no longer structurally stable after printing into the moulds (Figure 8). Only the 2NapFF/RPMI and 2NapFF/HPLM remained self-supporting hydrogels after printing, but the viscous nature of the samples meant it was not possible to form distinct lines in the mould, as printed gel merged (Figure 9d). The lack of shape retention also meant it was not possible to create layers of printed gels.

## Chapter 5

The post-extrusion rheology data for these samples produced reproducible strain and frequency sweep data (Figure 9b, c, e and f). Concerning the 2NapFF/RPMI hydrogels, we observe an increase in stiffness after the printing process, with  $G'$  increasing from 1180 Pa to 2200 Pa, resulting in a recovery 185 %. In contrast, the HPLM hydrogels display a slight decrease in  $G'$  after printing from 491 Pa to 355 Pa, meaning that only 72 % of the initial storage modulus was recovered. A possible explanation for the printability of 2NapFF with RPMI media is that the high storage modulus of the pre-printed gel which has been found to correlate with a higher structural stability.<sup>36</sup> Despite this, the same effect was not observed from the 2NapFF hydrogels formed from DMEM+Glucose which also exhibited a similar  $G'$  value. Moreover, this does not explain the printability of the 2NapFF and HPLM samples. These findings further reinforce the need for characterisation of hydrogels after the printing process as pre-printing rheological properties may not correspond to printability. Furthermore, the samples gelled with RPMI undergo a slight increase in  $G'$  after printing which would not be accounted for if only the non-printed gels were examined.

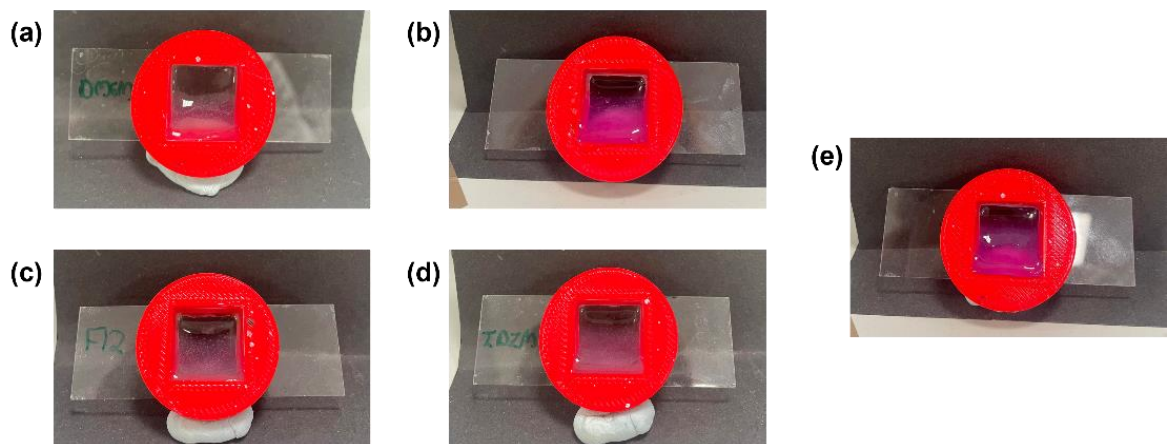


**Figure 8.** Photos of 2NapFF gels after printing with (a) DMEM (b) DMEM + glucose (c) DMEM F12 (d) IDIM (e) medium 199.

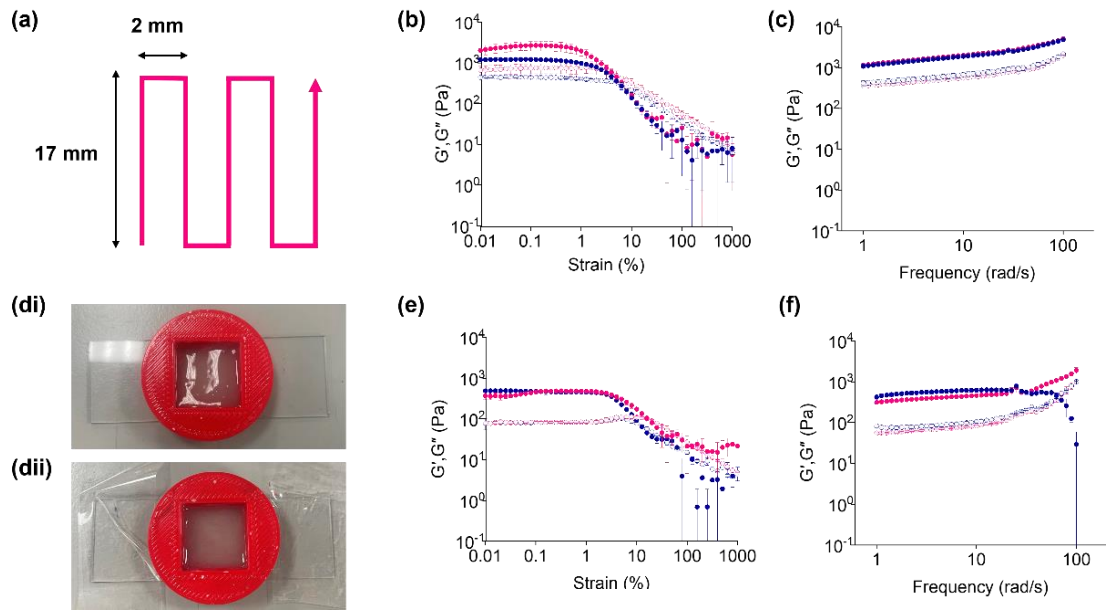


**Figure 9** (a) Schematic of serpentine pattern used to 3D print hydrogels into holders for rheological characterisation. (b) Strain sweeps of 2NapFF/RPMI printed (pink) and non-printed (blue) hydrogels. (c) Frequency sweeps of 2NapFF/RPMI printed (pink) and non-printed (blue) hydrogels. (di) 2NapFF/RPMI hydrogel printed into 3D printed holder. (dii) 2NapFF/HPLM hydrogel printed into 3D printed holder. (e) Strain sweeps of 2NapFF/HPLM printed (pink) and non-printed (blue) hydrogels (f) (c) Frequency sweeps of 2NapFF/HPLM printed (pink) and non-printed (blue) hydrogels. In all cases, error bars represent the standard deviation between triplicates. One printed sample was used per measurement.

From our findings in Chapter 2, we concluded that DMEM caused the gelation of 2NapFF either by a buffering effect, crosslinking via divalent cations present in the culture media or a combination of both. To test this theory and understand why some of the gels print better than others we turned to the inorganic salts present in each media (Table 1). We noted that HPLM contains  $\text{CaCl}_2$ ,  $\text{MgSO}_4$ ,  $\text{MgCl}_2$  and  $(\text{Ca}(\text{NO}_3)_2 \cdot 4\text{H}_2\text{O})$ , all of which consist of divalent cations. As previous work has confirmed that 2NapFF can be gelled using divalent cations,<sup>40</sup> the high cation concentration may be causing an increased number of crosslinks within the network, enhancing the printability. Interestingly, RPMI only contains  $\text{MgSO}_4$  and  $(\text{Ca}(\text{NO}_3)_2 \cdot 4\text{H}_2\text{O})$  with regards to divalent salts, but, notably, the concentration of  $(\text{Ca}(\text{NO}_3)_2 \cdot 4\text{H}_2\text{O})$  is significantly higher (0.4 mM) than in HPLM (0.04 mM) which could explain the high stiffness and printability of the 2NapFF/RPMI gel.

**Table 1.** Table showing the inorganic salts present in each media examined.

	DMEM	DMEM+Glu	DMEM F12	RPMI	IDIM	HPLM	Medium 199
CaCl <sub>2</sub>	✓	✓	✓	x	✓	✓	✓
Fe(NO <sub>3</sub> ) <sub>3</sub> ·9H <sub>2</sub> O	✓	✓	✓	x	x	x	x
MgSO <sub>4</sub>	✓	✓	✓	✓	✓	✓	✓
KCl	✓	✓	✓	✓	✓	✓	✓
NaHCO <sub>3</sub>	✓	✓	✓	✓	✓	✓	✓
NaCl	✓	✓	✓	✓	✓	✓	✓
NaH <sub>2</sub> PO <sub>4</sub>	✓	✓	✓	✓	x	x	x
CuSO <sub>4</sub> ·5H <sub>2</sub> O	x	x	✓	x	x	x	x
FeSO <sub>4</sub> ·7H <sub>2</sub> O	x	x	✓	x	x	x	x
MgCl <sub>2</sub>	x	x	✓	x	x	✓	x
NaH <sub>2</sub> PO <sub>4</sub> ·H <sub>2</sub> O	x	x	✓	x	✓	✓	✓
ZnSO <sub>4</sub> ·7H <sub>2</sub> O	x	x	✓	x	x	x	x
Ca(NO <sub>3</sub> ) <sub>2</sub> ·4H <sub>2</sub> O	x	x	x	✓	x	✓	x
KNO <sub>3</sub>	x	x	x	x	✓	x	x
Na <sub>2</sub> SeO <sub>3</sub> ·5H <sub>2</sub> O	x	x	x	x	✓	x	x
NH <sub>4</sub> Cl	x	x	x	x	x	✓	x
K <sub>2</sub> HPO <sub>4</sub>	x	x	x	x	x	✓	x
Fe(NO <sub>3</sub> ) <sub>3</sub> ·9H <sub>2</sub> O	x	x	x	x	x	x	✓

### 5.2.2. Using SAXS to investigate the effect of 3D printing

While rheological measurements indicate how the bulk network is affected by printing, we also wanted to investigate the printing process's effect on a nanoscale level. Therefore, we used small-angle x-ray scattering (SAXS) to probe the one-dimensional structures present in both the non-printed and printed gels. In each case, the printed data collected was almost identical to the non-printed data (Figure 10). This was reflected in the values obtained from fitting parameters (Table 2 and 3). Before printing, all samples fit to a cylinder model with a power law (Figure 11). The length was reported as outside of the range measured by SAXS and thus the value was fixed to 2000 Å for all samples, except for the 2NapFF/DMEM + Glucose hydrogel, which had a length of 504 Å (Table 2). Similarly, all the fits reported a radius between 33.3 Å and 48.7 Å. The consistency of the values obtained from each fit suggests that the media used to gel the 2NapFF has little effect on the primary structures formed. Post-printing the samples produced data that still fit best to the cylinder model with a power law and a fixed length of 2000 Å (Figure 12). The radius values for these samples ranged between 38.7 Å and 46.1 Å (Table 2). Unusually high  $\chi^2$  values were obtained for the printed samples, particularly HPLM (65.1). However, before applying polydispersity to the radius the  $\chi^2$  values was significantly higher and as the parameters aligned with the other samples we felt the model was a reasonable choice. In general, these findings suggest that printing the hydrogels had little to no effect on the hydrogels at a nanoscale level.

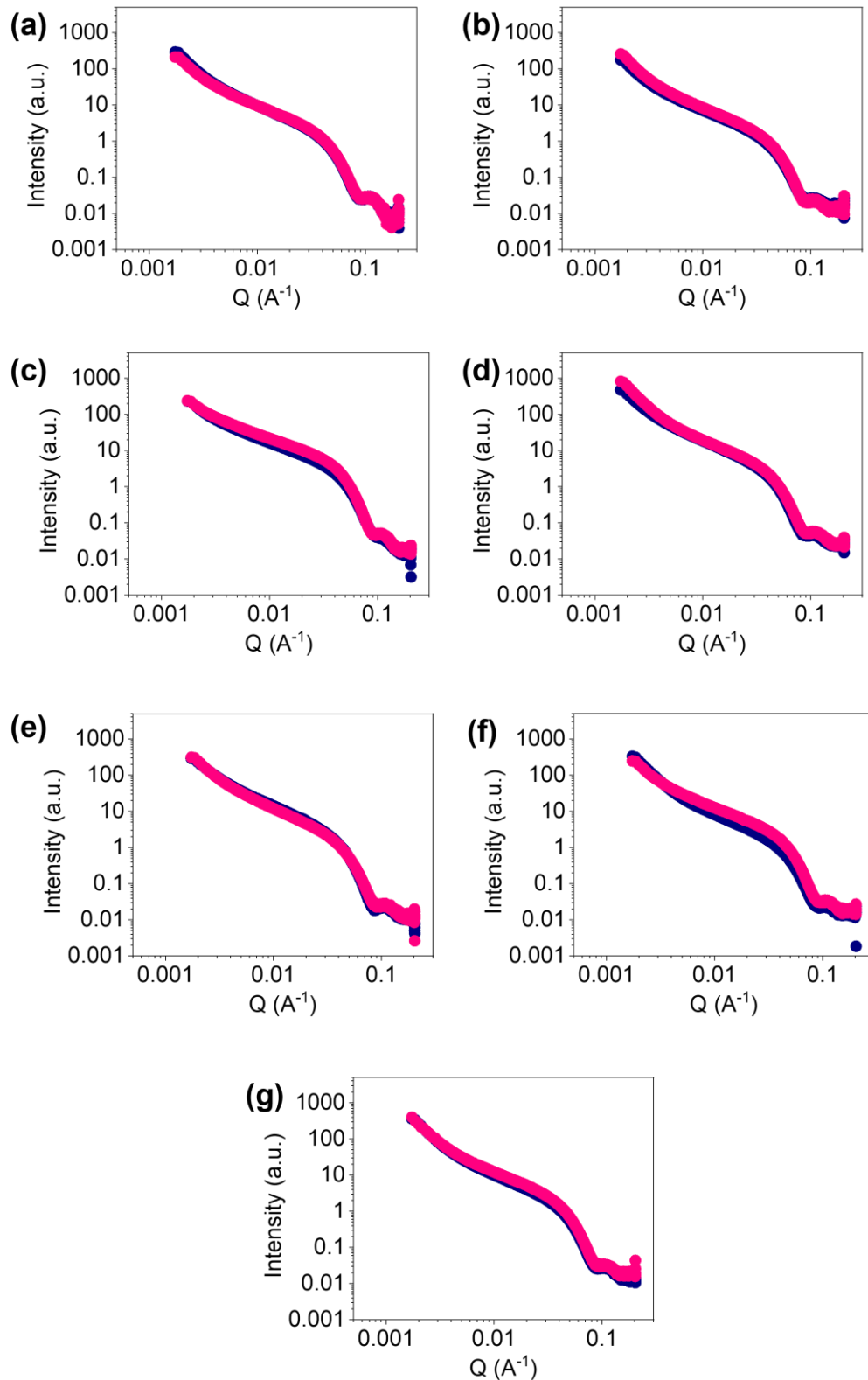


**Figure 10.** Plots of SAXS data of 2NapFF/media gels where the non-printed data is (navy) and printed data (pink) is overlaid. In each case the 2NapFF is gelled with (a) DMEM (b) DMEM + Glucose (c) DMEM F12 (d) RPMI (e) IDIM (f) HPLM and (g) Medium 199 respectively.

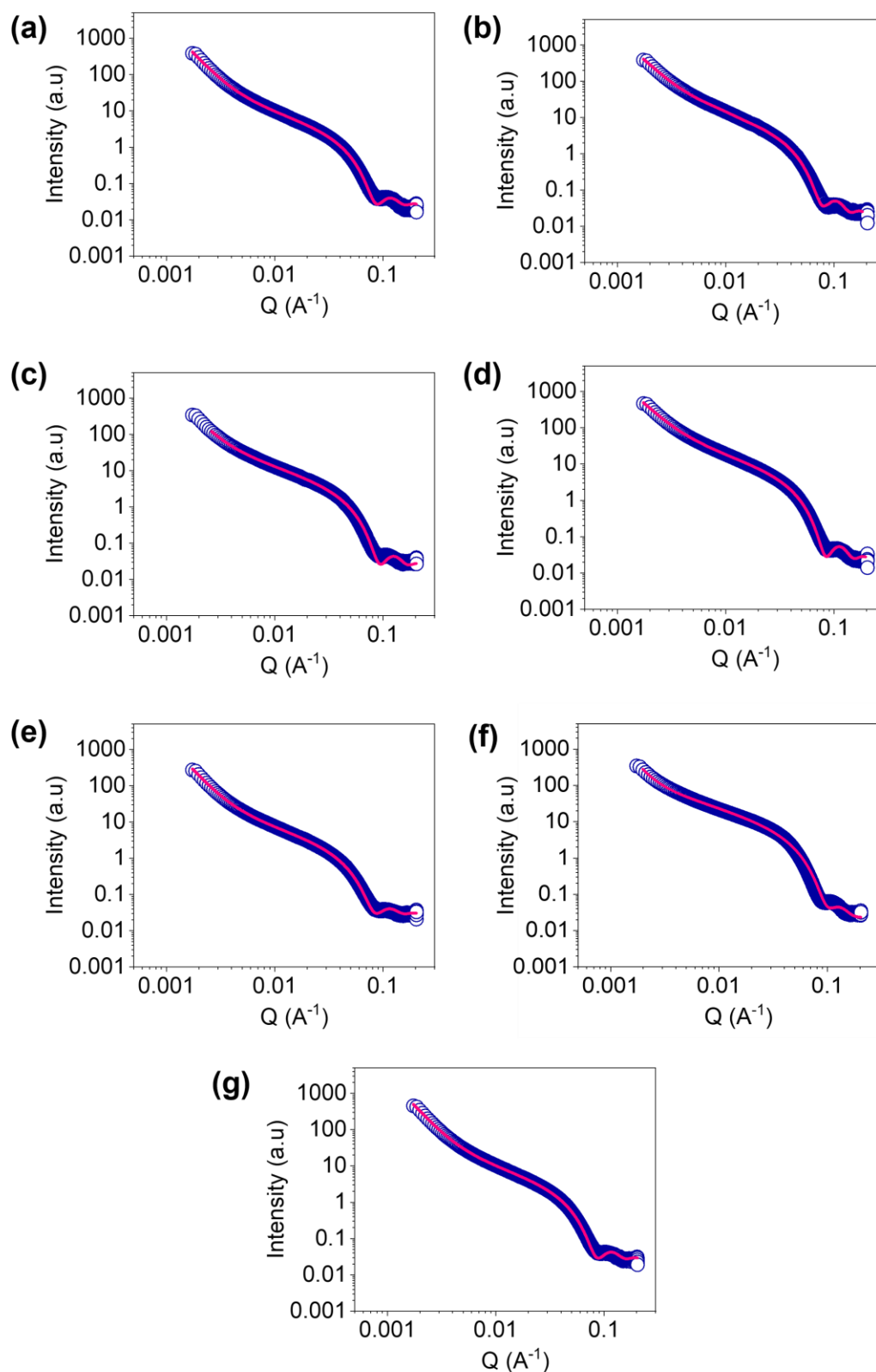


**Figure 11.** Plots of SAXS data of non-printed 2NapFF/media gels (navy) overlaid with fits to the data (pink). In each case the 2NapFF is gelled with **(a)** DMEM **(b)** DMEM + Glucose **(c)** DMEM F12 **(d)** RPMI **(e)** IDIM **(f)** HPLM and **(g)** Medium 199 respectively.

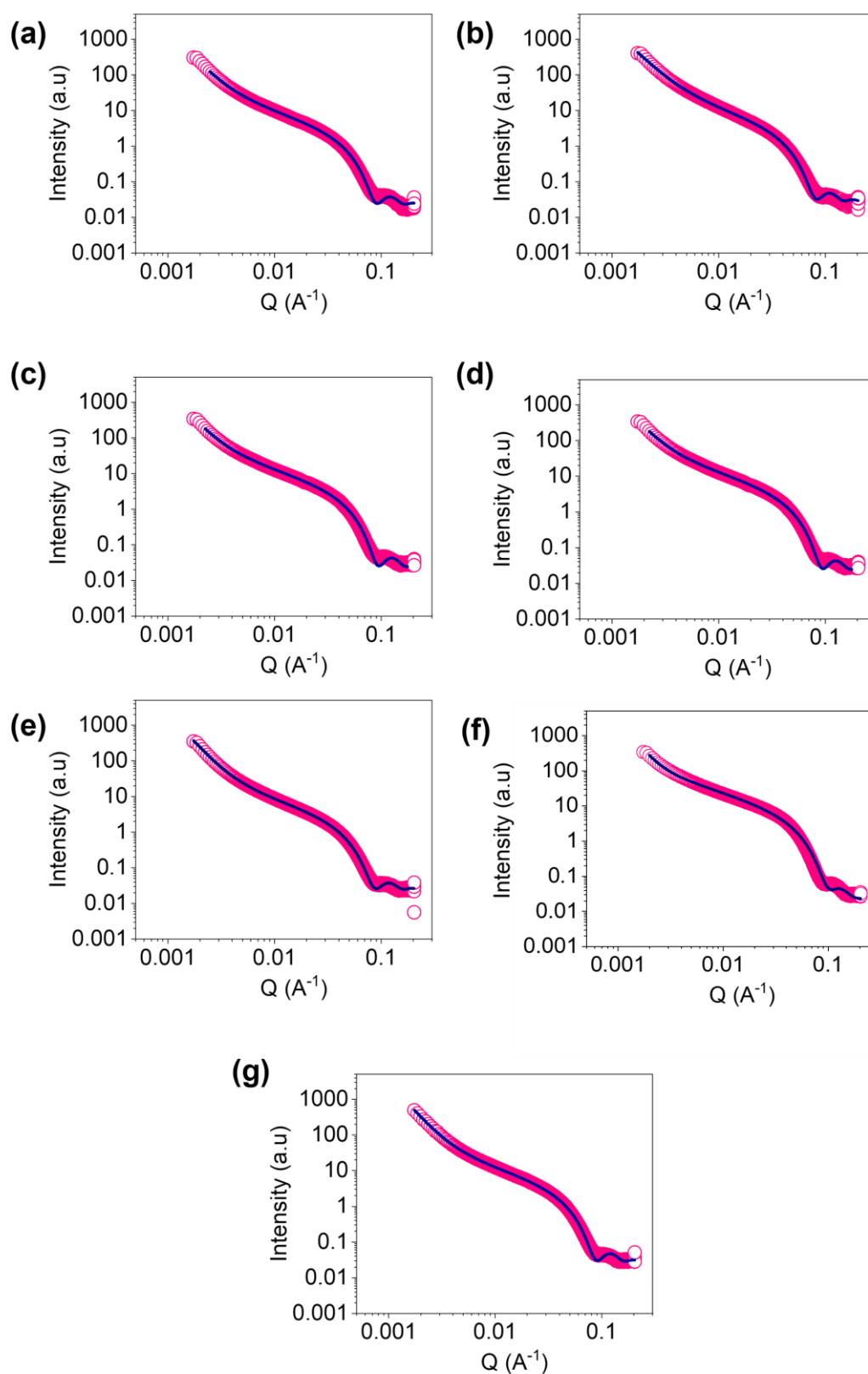


**Figure 12.** Plots of SAXS data of printed 2NapFF/media gels (pink) overlaid with fits to the data (navy). In each case the 2NapFF is gelled with (a) DMEM (b) DMEM + Glucose (c) DMEM F12 (d) RPMI (e) IDIM (f) HPLM and (g) Medium 199 respectively.

## Chapter 5

**Table 2.** Summary of the parameters obtained from fitting SAXS data collected for each non-printed sample. The error of each parameter is shown below each value. Fitting parameters obtained from SasView 5.0.6 model fitting of the SAXS data. In each case the calculated SLD value was 14.196 and 9.469 for the SLD solvent. See section 2.7.3 for full fitting details. See section 2.7.3 for full fitting details.

	DMEM	DMEM + Glucose	DMEM F12	RPMI	IDIM	HPLM	Medium 199
<b>Model</b>	CYLINDER + POWER LAW	CYLINDER + POWER LAW	CYLINDER + POWER LAW	CYLINDER + POWER LAW	CYLINDER + POWER LAW	CYLINDER + POWER LAW	CYLINDER + POWER LAW
<b>A Scale</b>	0.00229 ± 1 x 10 <sup>-6</sup>	0.00256 ± 1 x 10 <sup>-6</sup>	0.00190 ± 1 x 10 <sup>-6</sup>	0.00396 ± 1 x 10 <sup>-6</sup>	0.00172 ± 1 x 10 <sup>-6</sup>	0.00508 ± 1 x 10 <sup>-6</sup>	0.00236 ± 1 x 10 <sup>-6</sup>
<b>Background</b>	0.0255 ± 2 x 10 <sup>-4</sup>	0.0219 ± 2 x 10 <sup>-4</sup>	0.0274 ± 2 x 10 <sup>-4</sup>	0.0256 ± 2 x 10 <sup>-4</sup>	0.0292 ± 2 x 10 <sup>-4</sup>	0.0270 ± 2 x 10 <sup>-4</sup>	0.0270 ± 2 x 10 <sup>-4</sup>
<b>A Length / Å</b>	2000 (fixed)	504 ± 0.8	2000 (fixed)	2000 (fixed)	2000 (fixed)	2000 (fixed)	2000 (fixed)
<b>A Radius / Å</b>	43.2 ± 0.01	48.7 ± 0.01	43.4 ± 0.01	44.7 ± 0.009	43.8 ± 0.02	39.6 ± 0.02	33.3 ± 0.01
<b>B Scale</b>	1.96 x 10 <sup>-7</sup> ± 1 x 10 <sup>-9</sup>	8.57 x 10 <sup>-6</sup> ± 6 x 10 <sup>-8</sup>	1.33 x 10 <sup>-7</sup> ± 8 x 10 <sup>-10</sup>	3.72 x 10 <sup>-6</sup> ± 3 x 10 <sup>-8</sup>	1.29 x 10 <sup>-6</sup> ± 9 x 10 <sup>-10</sup>	4.32 x 10 <sup>-8</sup> ± 2 x 10 <sup>-9</sup>	1.84 x 10 <sup>-7</sup> ± 1 x 10 <sup>-9</sup>
<b>B Power</b>	3.36 ± 0.001	2.77 ± 0.001	3.45 ± 0.001	2.89 ± 0.002	3.42 ± 0.002	3.58 ± 0.007	3.40 ± 0.001
<b>χ<sup>2</sup></b>	16.1	12.3	10.2	8.39	6.94	7.34	13.6

## Chapter 5

**Table 3.** Summary of the parameters obtained from fitting SAXS data collected for each printed sample. The error of each parameter is shown below each value. Fitting parameters obtained from SasView 5.0.6 model fitting of the SAXS data. For the HPLM samples 0.1 polydispersity was applied to the radius. In each case the calculated SLD value was 14.196 and 9.469 for the SLD solvent. See section 2.7.3 for full fitting details. See section 2.7.3 for full fitting details

	DMEM	DMEM + Glucose	DMEM F12	RPMI	IDIM	HPLM	Medium 199
<b>Model</b>	CYLINDER + POWER LAW	CYLINDER + POWER LAW + PD	CYLINDER + POWER LAW				
<b>A Scale</b>	0.00251 ± 1 x 10 <sup>-6</sup>	0.00244 ± 2 x 10 <sup>-6</sup>	0.00367 ± 1 x 10 <sup>-6</sup>	0.00367 ± 1 x 10 <sup>-6</sup>	0.00208 ± 1 x 10 <sup>-6</sup>	0.00745 ± 1 x 10 <sup>-6</sup>	0.00313 ± 1 x 10 <sup>-6</sup>
<b>Background</b>	0.0234 ± 1 x 10 <sup>-4</sup>	0.0286 ± 2 x 10 <sup>-4</sup>	0.0240 ± 2 x 10 <sup>-4</sup>	0.0243 ± 2 x 10 <sup>-4</sup>	0.0250 ± 2 x 10 <sup>-4</sup>	0.0148 ± 2 x 10 <sup>-6</sup>	0.0290 ± 2 x 10 <sup>-4</sup>
<b>A Length / Å</b>	2000 (fixed)	2000 (fixed)	2000 (fixed)				
<b>A Radius / Å</b>	41.9 ± 0.01	46.1 ± 0.02	40.3 ± 0.01	44.7 ± 0.009	42.8 ± 0.02	38.7 ± 0.005	42.3 ± 0.01
<b>B Scale</b>	1.71 x 10 <sup>-7</sup> ± 2 x 10 <sup>-9</sup>	1.44 x 10 <sup>-6</sup> ± 1 x 10 <sup>-8</sup>	1.26 x 10 <sup>-7</sup> ± 1 x 10 <sup>-9</sup>	3.72 x 10 <sup>-6</sup> ± 4 x 10 <sup>-8</sup>	9.44 x 10 <sup>-8</sup> ± 8 x 10 <sup>-10</sup>	1.41 x 10 <sup>-9</sup> ± 2 x 10 <sup>-11</sup>	9.93 x 10 <sup>-8</sup> ± 7 x 10 <sup>-10</sup>
<b>B Power</b>	3.34 ± 0.001	3.05 ± 0.002	3.41 ± 0.003	2.89 ± 0.002	3.46 ± 0.00	4.09 ± 0.005	3.50 ± 0.001
<b>χ<sup>2</sup></b>	7.94	10.5	29.9	27.6	10.9	65.4	9.26

### 5.2.3. Optimisation of parameters for bioprinting

A sterile environment is essential for bioprinting to ensure cell viability. For this reason, we decided to test if the samples could be printed using a Cellink Bio X6 printer, which can be UV sterilised before use and provide HEPA filtered airflow during the experiment (Figure 13a). Previously, the pre-gel solutions had been loaded into a syringe and left overnight before printing, however, this is not suitable if cells are present in the samples. Therefore, we resorted to loading the pre-gelled solution in a 3 mL syringe cartridge and incubating for 20 minutes at 37°C and 5 % CO<sub>2</sub>. After this time, the syringe was equipped with a 25 G, 24 m needle (Cellink NZ6250255001) and printed into a slide. Each hydrogel was printed in a serpentine fashion (Figure 13b) and the printing parameters were optimised by varying the pressure and speed until the most consistent, homogeneous structure was formed. A phone camera equipped with a clip-on macro-lens was used to image the optimised printed gels from a “head-on” angle to gain an insight of the printed sample’s interaction with the glass slide (Figure 14 a-g). Namely, samples that did not print well present a larger, more spread-

## Chapter 5

out morphology (Figure 14a, c, e, g) than those that printed well (Figure 14b, d, f). This is because the 2NapFF hydrogels formed with DMEM + glucose, RPMI and HPLM exhibit structural integrity after the bioprinting process. Variations between results observed from the preliminary printing studies using the 3D printers are likely due to the differences between the preparation methods.

For instance, the bioprinted samples were incubated at 37°C, which we discovered significantly impacted the rheological properties of the 2NapFF/DMEM+glucose in Chapter 2. This may explain why the 2NapFF/DMEM+glucose sample (Figure 14b) printed nicely using the bioprinter despite not having done so previously.

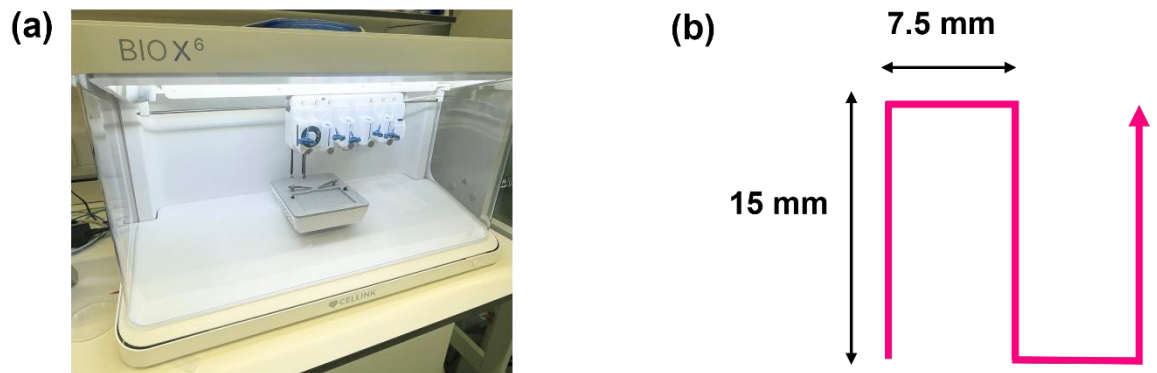


**Figure 13 (a)** Photograph of Cellink Bio X6 printer used to print samples. **(b)** Schematic of serpentine pattern used to print hydrogels onto the glass slides.

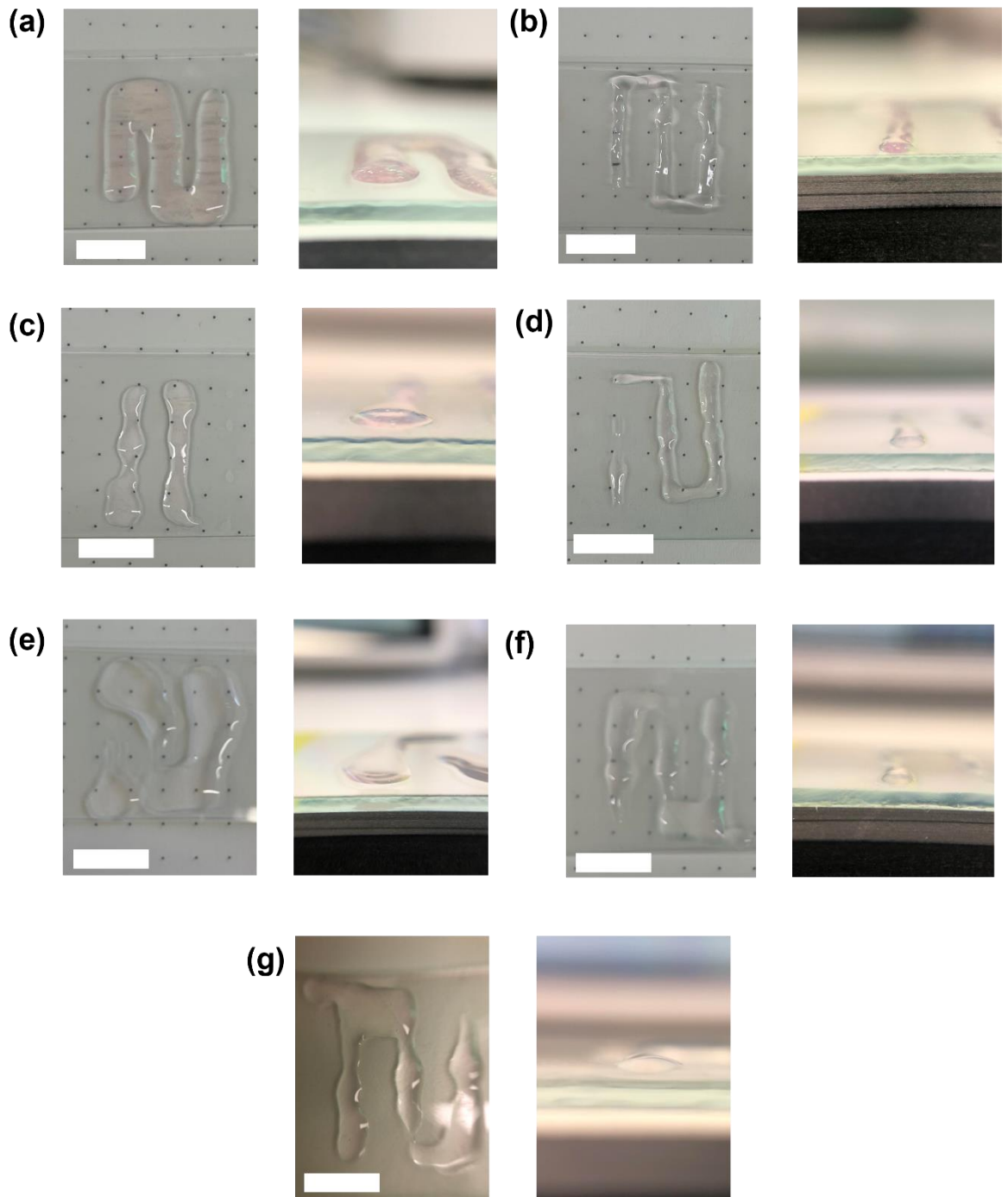


**Figure 14** (a) Optimised printed structures 2NapFF hydrogels gelled with DMEM (b) DMEM + Glucose (c) DMEM F12 (d) RPMI (e) IDIM (f) HPLM and (g) Medium 199 respectively. In each case, the left side photo is taken from above with a phone camera where the scale bar represents 1 cm. Each right-hand photo is taken “head-on” with a macro-lens attached to a phone camera.

## Chapter 5

To allow the shear rate for each sample to be calculated from the parameters available we used Equation 2, which states that the shear rate is equal to the velocity in  $\text{ms}^{-1}$  divided by the distance travelled in meters (m). We decided to use this equation opposed to Equation 1 as the bioprinter used does not provide any information on the volume printed. The shear rates were found to be in the range of  $900\text{-}1000 \text{ s}^{-1}$  which is consistent with the previously discussed results from the 3D printer. However, this calculated shear rate may not be completely accurate as it fails to account for factors including the pressure, size of the needle, and volume printed. Any slight variations may also be a consequence of the change in preparation technique used. It is also revealed that a higher pressure was required to print the HPLM and RPMI, leading to exposure to a higher shear stress than the other samples. We hypothesise that this observation may also be a result of the high storage modulus of gels from RPMI and the divalent cation concentration of HPLM.

$$\text{Shear rate, } \gamma = \frac{v}{D} \quad (\text{Equation 2})$$

**Table 4.** Table showing optimal printing parameters used for bioprinting the 2NapFF hydrogels and the calculated shear rate.

	<b>Pressure (kPa)</b>	<b>Speed (m/s)</b>	<b>Distance (m)</b>	<b>Shear Rate (<math>\text{s}^{-1}</math>)</b>
<b>DMEM</b>	25	50	0.05	1000
<b>DMEM Glu</b>	30	50	0.05	1000
<b>DMEM F12</b>	30	50	0.05	1000
<b>RPMI</b>	100	45	0.05	900
<b>IDIM</b>	35	55	0.05	1100
<b>HPLM</b>	50	50	0.05	1000
<b>Medium 199</b>	35	50	0.05	1000

#### 5.2.4 Bioprinting macrophages with 2NapFF/RPMI

Despite the correlation between high shear stress and cell death, we decided to further examine the potential of the 2NapFF/RPMI hydrogels as bioinks due to their high structural fidelity. Moreover, RPMI can be used as a growth media for macrophages, which are highly adhesive cells and thus more likely to remain in the hydrogels without the addition of adhesive motifs. Furthermore, the ability to bioprint macrophages has the potential to advance research and therapies in the fields of immunity and tissue repair due to their role in immune responses.<sup>42</sup> Samples were prepared as before, but with the media containing enough macrophages to give a final cell density 200,000 cells per mL. After printing into a 6-well plate, media was added to each well and samples were incubated overnight, before staining the following day. The confocal images confirmed that the 2NapFF/RPMI media hydrogels successfully printed the encapsulated macrophages (Figure 15). However, the low cell number observed is related to the low cell density used for this experiment, because of issues removing the highly adhesive differentiated macrophages from the tissue culture plastic. Nevertheless, the z-stack images revealed an even distribution of cells throughout the samples highlighting the potential of these materials as bioinks in the future.

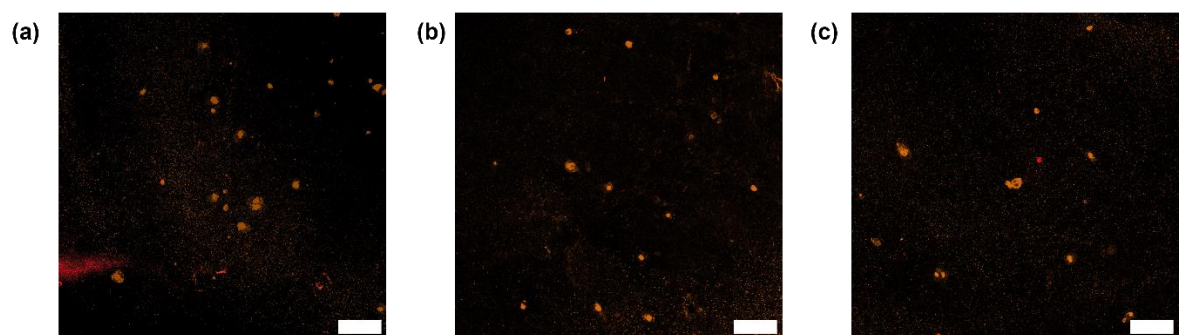


**Figure 15. (a-c)** Confocal images of macrophages 24 hours after seeding in the hydrogels and stained and actin (orange). Imaging was performed using a ZEISS LSM 980 confocal microscope using 10x objective. . Images were processed in ImageJ to create max-projection images of the original z-stacks. Scale bar represents 100  $\mu\text{m}$ .

### 5.3 Conclusions

Through this work, we have demonstrated that the rheological properties and printability of these 2NapFF hydrogels are affected by the media used to trigger gelation. We have also highlighted that a high storage modulus of the unprinted material does not guarantee printability. For example, RPMI and DMEM + glucose produced hydrogels with close to identical rheological properties, yet the initial 3D printing tests found that while RPMI produced materials with structural fidelity, DMEM + glucose failed to. It was also revealed that only the 2NapFF hydrogels containing RPMI and HPLM were capable of printing reproducible, self-supporting structures. We hypothesised that this observation was linked to the divalent ion concentration which differs between media.

SAXS experiments disclosed that the media used to carry out the gelation of 2NapFF and printing through a needle had no significant effect on the nanoscale structures present. We propose that using ultra small-angle x-ray scattering may offer a deeper insight into the microstructure of these materials by allowing analysis on a micrometer scale. This method would complement the SAXS data by allowing comprehensive hierarchical structure assessment.<sup>41</sup>

The optimisation of the samples for bioprinting using the Cellink Bio X6 printer, once again highlighted the importance of pre-gelation processing on the properties of these materials. Particularly, as the printability of the DMEM + glucose samples significantly enhanced when formed in an incubator for 20 minutes, as opposed to overnight at room temperature. This finding also reiterates our point made in Chapter 2 that the temperature at which gelation occurs directly affects the properties of the gels. Finally, our preliminary bioprinting results using 2NapFF/RPMI hydrogels to encapsulate macrophages have showcased the biocompatibility and potential of these materials for use as bioinks. Future work may involve incorporating cell binding motifs such as arginylglycylaspartic acid (RGD) to improve the adhesive properties of the hydrogels so that other cell lines could also be printed.

In conclusion, we have successfully formed 2NapFF hydrogels with a range of media to achieve systems at physiological pH and assessed their printability. We have used oscillatory rheology and small-angle x-ray scattering to characterise the printed and non-printed samples across different length scales. Additionally, we have demonstrated the feasibility of printing the hydrogels using both a conventional 3D gel printer and a bioprinter, confirming their potential use as bioinks.

5.4 References

1. B. C. Gross, J. L. Erkal, S. Y. Lockwood, C. Chen and D. M. Spence, *Anal. Chem.*, 2014, **86**, 3240-3253.
2. S. Huang, P. Liu, A. Mokasdar and H. Liang, *J. Adv. Manuf. Technol.*, 2012, **67**.
3. H. Geckil, F. Xu, X. Zhang, S. Moon and U. Demirci, *Nanomedicine*, 2010, **5**, 469-484.
4. S. Uman, A. Dhand and J. A. Burdick, *J. Appl. Polym. Sci.*, 2020, **137**, 48668.
5. B. Kong and Y. Zhao, *BME Front.*, 2023, **4**, 0010.
6. B. S. Kim, Y. W. Kwon, J.-S. Kong, G. T. Park, G. Gao, W. Han, M.-B. Kim, H. Lee, J. H. Kim and D.-W. Cho, *Biomaterials*, 2018, **168**, 38-53.
7. Z. Yazdanpanah, J. D. Johnston, D. M. L. Cooper and X. Chen, *Front. Bioeng. Biotechnol.*, 2022, **10**.
8. S. Sabetkish, P. Currie and L. Meagher, *Acta. Biomater.*, 2024, **181**, 46-66.
9. M. J. Song, R. Quinn, E. Nguyen, C. Hampton, R. Sharma, T. S. Park, C. Koster, T. Voss, C. Tristan, C. Weber, A. Singh, R. Dejene, D. Bose, Y.-C. Chen, P. Derr, K. Derr, S. Michael, F. Barone, G. Chen, M. Boehm, A. Maminishkis, I. Singec, M. Ferrer and K. Bharti, *Nat. Methods*, 2023, **20**, 149-161.
10. J. M. R. Rego, L. M. Cerezo, A. M. García and A. C. M. Romero, *3D Printing: Fundamentals to Emerging Applications*, Taylor & Francis Group, 2023, 437-449.
11. X. B. Chen, A. Fazel Anvari-Yazdi, X. Duan, A. Zimmerling, R. Gharraei, N. K. Sharma, S. Sweilem and L. Ning, *Bioact. Mater.*, 2023, **28**, 511-536.
12. J. Gong, C. C. L. Schuurmans, A. M. v. Genderen, X. Cao, W. Li, F. Cheng, J. J. He, A. López, V. Huerta, J. Manríquez, R. Li, H. Li, C. Delavaux, S. Sebastian, P. E. Capendale, H. Wang, J. Xie, M. Yu, R. Masereeuw, T. Vermonden and Y. S. Zhang, *Nat. Commun.*, 2020, **11**, 1267.
13. M. J. Uddin, J. Hassan and D. Douroumis, *Technologies*, 2022, **10**, 108.
14. E. S. Bishop, S. Mostafa, M. Pakvasa, H. H. Luu, M. J. Lee, J. M. Wolf, G. A. Ameer, T.-C. He and R. R. Reid, *Genes Dis*, 2017, **4**, 185-195.
15. V. Keriquel, H. Oliveira, M. Rémy, S. Ziane, S. Delmond, B. Rousseau, S. Rey, S. Catros, J. Amédée, F. Guillemot and J. C. Fricain, *Sci. Rep.*, 2017, **7**, 1778.
16. W. Fang, M. Yang, L. Wang, W. Li, M. Liu, Y. Jin, Y. Wang, R. Yang, Y. Wang, K. Zhang and Q. Fu, *Int. J. Bioprint.*, 2023, **9**, 759.

## Chapter 5

17. P. S. Gungor-Ozkerim, I. Inci, Y. S. Zhang, A. Khademhosseini and M. R. Dokmeci, *Biomater. Sci.*, 2018, **6**, 915-946.
18. G. A. Salg, A. Blaeser, J. S. Gerhardus, T. Hackert and H. G. Kenngott, *Int. J. Mol. Sci.*, 2022, **23**, 8589.
19. E. Merotto, P. G. Pavan and M. Piccoli, *Biomedicines*, 2023, **11**, 1742.
20. E. Baur, M. Hirsch and E. Amstad, *Adv. Mater. Technol.*, 2023, **8**, 2201763.
21. S. Kumar, *Mater. Adv.*, 2021, **2**, 6928-6941.
22. S. Hafeez, M. C. Decarli, A. Aldana, M. Ebrahimi, F. A. A. Ruitter, H. Duimel, C. van Blitterswijk, L. M. Pitet, L. Moroni and M. B. Baker, *Adv. Mater.*, 2023, **35**, 2301242.
23. D. J. Adams, *J. Am. Chem. Soc.*, 2022, **144**, 11047-11053.
24. R. G. Weiss, *J. Am. Chem. Soc.*, 2014, **136**, 7519-7530.
25. B. Raphael, T. Khalil, V. Workman, A. Smith, C. Brown, C. Streulli, A. Saiani and M. Domingos, *Mater. Lett.*, 2016, **190**, 102-106.
26. M. M. Harper, M. L. Connolly, L. Goldie, E. J. Irvine, J. E. Shaw, V. Jayawarna, S. M. Richardson, M. J. Dalby, D. Lightbody and R. V. Ulijn, *Methods Mol. Biol.*, 2018, **1777**, 283-303.
27. O. El Hamoui, T. Saydé, I. Svahn, A. Gudin, E. Gontier, P. Le Coustumer, J. Verget, P. Barthélémy, K. Gaudin, S. Battu, G. Lespes and B. Alies, *ACS Biomater. Sci. Eng.*, 2022, **8**, 3387-3398.
28. F. Andriamiseza, D. Bordignon, B. Payré, L. Vaysse and J. Fitremann, *J. Colloid and Interface Sci.*, 2022, **617**, 156-170.
29. A. Chalard, M. Mauduit, S. Souleille, P. Joseph, L. Malaquin and J. Fitremann, *Addit. Manuf.*, 2020, **33**, 101162.
30. S. Rauf, H. H. Susapto, K. Kahin, S. Alshehri, S. Abdelrahman, J. H. Lam, S. Asad, S. Jadhav, D. Sundaramurthi, X. Gao and C. A. E. Hauser, *J. Mater. Chem. B*, 2021, **9**, 1069-1081.
31. M. C. Nolan, A. M. Fuentes Caparrós, B. Dietrich, M. Barrow, E. R. Cross, M. Bleuel, S. M. King and D. J. Adams, *Soft Matter*, 2017, **13**, 8426-8432.
32. A. M. Fuentes-Caparrós, Z. Canales-Galarza, M. Barrow, B. Dietrich, J. Läger, M. Nemeth, E. R. Draper and D. J. Adams, *Biomacromolecules*, 2021, **22**, 1625-1638.
33. A. Ribeiro, M. M. Blokzijl, R. Levato, C. W. Visser, M. Castilho, W. E. Hennink, T. Vermonden and J. Malda, *Biofabrication*, 2017, **10**, 014102.

## Chapter 5

34. A. Fatimi, O. V. Okoro, D. Podstawczyk, J. Siminska-Stanny and A. Shavandi, *Gels*, 2022, **8**, 179.
35. G. C. Papanicolaou and S. P. Zaoutsos, in *Creep and Fatigue in Polymer Matrix Composites*, ed. R. M. Guedes, Woodhead Publishing, 2011, 3-47.
36. A. Schwab, R. Levato, M. D'Este, S. Piluso, D. Eglin and J. Malda, *Chem. Rev.*, 2020, **120**, 11028-11055.
37. J. Karvinen and M. Kellomäki, *Bioprinting*, 2023, **32**, e00274.
38. I. Koumentakou, A. Michopoulou, M. J. Noordam, Z. Terzopoulou and D. N. Bikiaris, *J Mater. Sci.*, 2024, **59**, 9021-9041.
39. H. Herrada-Manchón, M. A. Fernández and E. Aguilar, *Gels*, 2023, **9**, 517.
40. A. Z. Cardoso, L. L. E. Mears, B. N. Cattoz, P. C. Griffiths, R. Schweins and D. J. Adams, *Soft Matter*, 2016, **12**, 3612-3621.
41. H. Okuda and O. Shojiro, *J. Jpn. Inst. Light Met.*, 2010, **60**, 36-40.
42. E. S. Bishop, S. Mostafa, M. Pakvasa, H. H. Luu, M. J. Lee, J. M. Wolf, G. A. Ameer, T. C. He and R. R. Reid, *Genes Dis.*, 2017, **4**, 185-195

## **Chapter 6: Conclusions and Future Work**

## Chapter 6

The aim of this thesis was to develop and characterise a LMWG gelator system at physiological pH which can be used for cell culture applications. Many of the gelation triggers commonly used to induce gelation of LMWG are not ideal for cell culture. For example, a heating and cooling cycle can cause cell death or denature cellular proteins. Similarly, pH triggers often result in networks with an acidic pH and organic solvents used for solvent switch triggers can be detrimental to cells. In this work, we have used a dipeptide-based LMWG (2NapFF) that can be triggered using cell culture media to produce biocompatible hydrogels suitable for cell culture applications. This strategy aligns with the literature advocating for physiologically relevant gelation conditions, such as the use of ionic triggers or enzymatic systems, to improve biocompatibility.<sup>1,2</sup> The work of Liu et al. also describes encapsulating cells within a LMWG matrix with DMEM (Dulbecco's Modified Eagle Medium).<sup>3</sup> However, this method utilises a solvent trigger approach which requires the gelator to be suspended in DMSO. The final solution had a DMSO concentration of between 2.5 and 3.3% which the authors consider acceptable. Despite this, it can be argued that concentrations of DMSO above 0.1% can affect cell viability.<sup>4</sup> In contrast, the 2NapFF/DMEM system investigated throughout this system has displayed the potential to encapsulate cells without the use of organic solvents. Future studies should build on the results presented in this thesis, extending the scope to include *in vivo* studies to validate the translational potential of these hydrogels for tissue engineering and regenerative medicine.

Through our work in Chapter 3, we have shown that heating and cooling a solution before triggering gelation can greatly impact the properties of the network produced, allowing us to access various properties from the same gelator. We went on to demonstrate that the bioactivity of the LMWG systems could be elevated by incorporating PODS® from Cell Guidance Systems, without significantly altering the mechanical properties. PODS® loaded with FGF-2 were used for this experiment as it has been shown to stimulate growth of MSCs as well as promote undifferentiated proliferation.<sup>5,6</sup> Thus, we would expect to see a higher number of live cells present in the samples containing the PODS®.

Future work would involve performing ELISA assays to quantify changes in proteins levels when the PODS® were incorporated and attempting to move towards a 3D cell culture approach. The addition of a bioadhesive motif such as RGD, could also be explored as a method of enhancing cell adhesion. Furthermore, techniques such as ultra-small angle x-ray scattering (USAXS) and Dynamic Light Scattering (DLS) can be used to analyse structures

## Chapter 6

present at a higher range than SAXS, allowing us to probe any interactions occurring between PODS® and the hydrogel network at a scale of up to 10  $\mu\text{M}$ .

Multicomponent supramolecular gelators are attractive candidates for potential biomaterials as they mimic the non-covalent multicomponent nature of the ECM. Additionally, multicomponent supramolecular systems offer novel properties that are not present in the individual species they are composed of. In Chapter 3 we probed the effects of combining 2NapFF hydrogels crosslinked with cell culture media to a Ureido-pyrimidinone (UPy) supramolecular hydrogel system. By combining these systems, we unveiled that self-sorting occurs between the 2NapFF and UPy components when the UPy crosslinking species is present. Furthermore, cell culture studies indicated that the presence of the crosslinker is essential for forming a network that supports cell adhesion. This finding complements prior studies using multicomponent supramolecular systems for cell culturing which also describe the effect mechanical and biochemical cues have on cell behaviour, including adhesion and differentiation.<sup>7,8</sup> Our results also support previous research which has revealed that the addition of different additives to a UPy system can impact cellular response.<sup>9</sup>

Bioprinting is an increasingly popular method for producing materials for biological applications. Due to their unique properties, LMWGs are gaining interest in this field. This inspired us to access the printability of the 2NapFF hydrogels explored in this thesis. By examining the rheological properties and printability of these systems in Chapter 4, we discovered that the media used to trigger gelation strongly influenced the properties of the resulting structures. This observation aligns with studies showing that the viscoelastic properties of bioinks strongly affect printability and the structural stability of printed constructs.<sup>10,11</sup> We went on to successfully print macrophage cells, which remained viable after 24 hours within the material. Regarding future work, USAXS may offer a deeper insight into the microstructure of these materials by allowing analysis on a micrometer scale. We would also like to repeat the bioprinting experiments with a larger volume of cells. Furthermore, while this work has shown that macrophages are present after 24 hours we do not have any indication of their viability. Therefore, further cytotoxicity assays to ensure macrophages remain viable and functional within hydrogels over time is crucial.

Our findings are particularly interesting as previous work in the field has focused on polymers such as methacrylamidated gelatin (GelMA) and hyaluronic acid.<sup>12</sup> In comparison to such materials 2NapFF would be considered cheaper and easier to scale up due to its small

## Chapter 6

size and straightforward synthesis. Therefore, our systems may be more suitable for large scale production which would be essential for clinical applications. Additionally, we could attempt to alter the mechanical properties of the hydrogels in order influence the polarization of macrophages into their various intermediate states (e.g., M1, M2, intermediate states) as gaining access to these phenotypes remains a challenge in the field.<sup>12,13</sup>

To conclude, we have presented a novel biomaterial which has been thoroughly characterised across multiple length scales. By probing the structure at the nanoscale and bulk level we have developed an understanding of how these systems self-assemble. We believe that by focusing on the comprehensive characterisation of such materials and integrating these with emerging trends in the literature we can replicate the ECM more precisely.

## References

1. S. Kralj, O. Bellotto, E. Parisi, A. M. Garcia, D. Iglesias, S. Semeraro, C. Deganutti, P. D'Andrea, A. V. Vargiu, S. Geremia, R. De Zorzi and S. Marchesan, *ACS Nano*, 2020, **14**, 16951-16961.
2. S. Toledano, R. J. Williams, V. Jayawarna and R. V. Ulijn, *J. Am. Chem. Soc.*, 2006, **128**, 1070-1071.
3. G. F. Liu, D. Zhang and C. L. Feng, *Angew Chem. Int. Ed. Engl.*, 2014, **53**, 7789-7793.
4. X. Chen and S. Thibault, *Annu Int. Conf. IEEE Eng. Med. Biol. Soc.*, 2013, 6228-6231.
5. L. Chen, M. Carlton and X Chen, N. Kaur, H. Ryan, T. J. Parker, Z. Lin, Y. Xiao and Y. Zhou, *Stem Cell Res. Ther.*, 2021, **12**, 165.
6. D. L. Coutu, M. François and J. Galipeau, *Blood*, 2011, **25**, 6801-6812.
7. Y. L. Wang, S. P. Lin, S. R. Nelli, F. K. Zhan, H. Cheng, T. S. Lai, M. Y. Yeh, H. C. Lin and S. C. Hung, *Macromol. Biosci.*, 2017, **17**, 1600192.
8. E.V. Alakpa, V. Jayawarna, A. Lampel, K. V. Burgess, C. C. West, S. C. J. Bakker, S. Roy, N. Javid, S. Fleming, D. A. Lamprou, J. Yang, A. Miller, A. J. Urquhart, P. W. J. M. Frederix, N. T. Hunt, B. Péault, R. V. Ulijn and M. J. Dalby, *Chem*, 2016, **1**, 298-319.
9. A. F. Vrethen, J. F. van Sprang, M. J. G. Schotman and P. Y. W. Dankers, *Mater. Today Bio*, 2024, **26**, 101021.

## Chapter 6

10. A. Ribeiro, M. M. Blokzijl, R. Levato, C. W. Visser, M. Castilho, W. E. Hennink, T. Vermonden and J. Malda, *Biofabrication*, 2017, **10**, 014102.
11. A. Fatimi, O. V. Okoro, D. Podstawczyk, J. Siminska-Stanny and A. Shavandi, *Gels*, 2022, **8**, 179.
12. D. Wu, T. Gong, Z. Sun, X. Yao, D. Wang, Q. Chen, Q. Guo, X. Li, Y. Guo, Y. Lu, *Int. J. Biol. Macromol.*, 2024, **269**, 131826
13. S. Chen, A. F. Saeed, Q. Liu, J. Jiang, H. Xu, G. Xiao<sup>5</sup>, L. Rao<sup>6</sup> and Y. Duo, *Sig. Transduct. Target Ther.* 2023, **207**